Analysis of electromagnetic emission measurement as a means of studying fracture processes in carbon fibre reinforced polymers

Dissertation

zur Erlangung des akademischen Grades

Dr. rer. nat.

eingereicht an der

Mathematisch-Naturwissenschaftlich-Technischen Fakultät

der Universtität Augsburg

von

Sebastian Gade

Augsburg, April 2023

Universität
Augsburg
University

Erstgutachter: Prof. Dr. Markus Sause

Zweitgutachter: Prof. Dr. Siegfried Horn

Tag der mündlichen Prüfung: 09.10.2023

Contents

1 Introduction

1.1 Motivation

Carbon fibre reinforced plastics (CFRP) are advanced composite materials that are engineered to exhibit extremely advantageous properties, such as high specific strength and stiffness. Because of these properties, CFRPs are preferably used in applications where high structural strength combined with low weight is required. For engineering applications and further advances in the understanding of the material, precise knowledge of the failure mechanisms is of utmost interest.

A variety of testing methods are available to investigate the complex failure mechanisms in CFRP, from microscopic damage to ultimate structural failure. Of particular interest are methods that provide live information on the damage evolution of a material under external loading. Since direct observation of the evolution of material damage is not possible in most cases, the measurement and analysis of signals generated by the formation and propagation of internal damage has proven to be a suitable means of investigating these processes. However, these methods require a detailed understanding of the correlation between the recorded signals and the emission processes.

Acoustic emission (AE) analysis is a well-established and successfully applied tool for investigating the damage evolution in CFRP. Areas of application for AE analysis on CFRP range from the standard mechanical testing methods to health monitoring of complex components or structures. However, due to the inevitable influence of the propagation path on the acoustic waves, measured as transient displacements at the materials surface, the complex mechanisms and correlations are still the subject of research. In addition, AE sensors usually have a non-linear transfer function, which can have a significant effect on the measured signals.

A different kind of signals, emitted during the fracture of solids, are electromagnetic signals. This phenomenon is commonly referred to as electromagnetic emission (EME). Although EME has been reported for the fracture of almost any type of material, the focus of research and a large part of the published literature is in the field of geophysics. Here, the main advantage of EME is the speed of signal propagation, which makes EME an ideal candidate for effective early warning systems. However, published research on EME from composite materials, particularly CFRP, is very limited.

The prospect of a more direct signal propagation in the material, with less interfering effects of geometry and internal structure, makes a comprehensive study of EME generated by CFRP fracture worthwhile.

1.2 Scope and structure of this study

This work presents the results obtained in a research project on the measurement and investigation of electromagnetic emission during the fracture of CFRP and its components. In the course of this project, the basics for successful measurement of EME signals were developed first. This included the development of a suitable measurement system consisting of sensors, amplifiers and sufficient shielding measures. The measurement equipment was continuously improved and adjusted during the course of the project. The first experimental fracture tests were then carried out on the individual components of CFRP. This was followed by tests on various CFRP specimens.
A large part of the work was carried out between 2012 and 2016 as part of the project "Relation of electromagnetic and acoustic emission to temporal and spatial crack motion on a microscopic scale in polymers and carbon fibres" funded by Deutsche Forschungsgemeinschaft (research projects HO 955/8-1 and HO 955/8-2). Therefore, some of the results presented in this text were published before [1, 2, 3], between 2014 and 2017. In this text, all of these results are summarised and complemented with the results of additional measurements from 2016 and 2017.

Chapter 2 provides an overview of the theoretical foundations of this study. In particular, an introduction to the generation and measurement of electromagnetic emission is given. Chapters 3 and 4 present and discuss the results of EME measurements on the different components of CFRP. Finally, chapters 5 and 6 present results of experiments performed on CFRP specimens in various configurations. A summarising discussion of all results is given in chapter 7.

2 Theoretical considerations and characterisation of measurement setup

2.1 Fracture of materials

2.1.1 Fundamentals

Although the fracture of materials has been examined qualitatively for centuries, *e.g.* in Leonardo da Vinci experiments "Testing the strength of iron wires of various lengths" [4], the origins of modern fracture mechanics are attributed to the work of Griffith, published in 1921 [5]. Griffith's model quantitatively describes the conditions under which defects in the material lead to the formation and propagation of cracks. The model correctly predicted the failure of ideally brittle solids. Griffith's concept of the strain energy release rate was later extended by Irwin [6] to include plastic deformation at the crack tip, though the inclusion of plasticity in the theory is somehow restricted, since the size of the plastic zone is assumed to be small compared to the crack length.

Irwin also introduced another concept to describe conditions for crack growth, the stress intensity, and shows that for linear elastic materials the two concepts are equivalent.

The strain energy release rate is defined as the decrease in total potential energy Π per increase in fracture surface area A:

$$G = -\frac{d\Pi}{dA} \tag{2.1}$$

and can be interpreted as the energy that is available for an incremental increase of the crack surface. Here, the total potential energy is composed of the strain energy stored in the material and the potential energy of external forces. The value of G depends on the external loading conditions (*i.e.* the applied load as well as the specific boundary conditions and specimen geometry), the size and geometry of the initial crack (or flaw) and the material's mechanical properties. When G reaches a critical value G_c, *i.e.* enough energy for crack growth is available, fracture occurs. This critical energy release rate G_c is assumed to be a material property.

For ideally brittle materials, the energy needed for crack growth is the energy necessary to break the atomic bonds within the material, schematically depicted in figure

3

2.1 (a). Since two new surfaces are created, the energy amounts to two times the surface energy. This minimum energy requirement is extended by further contributions for most materials that are not ideally linear elastic. This includes energy for plastic deformation, heat generation or other dissipative processes.
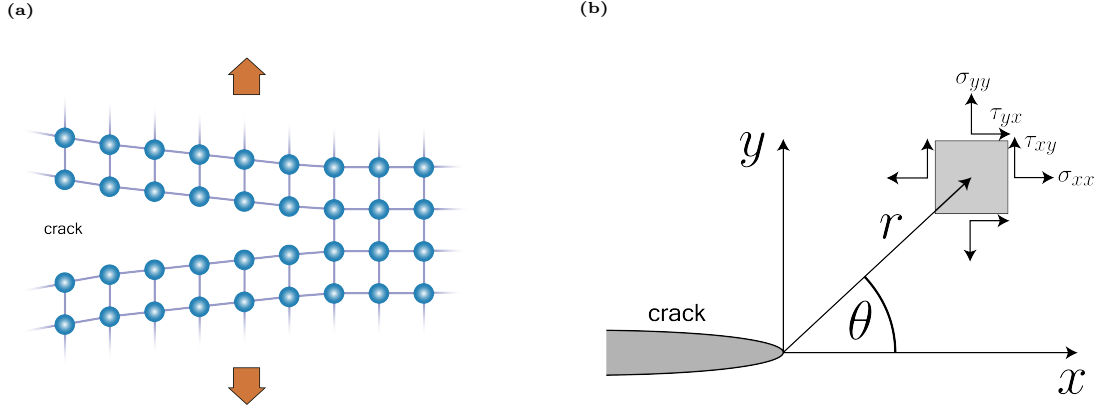

Figure 2.1: (a): Fracture of ideally brittle material. The minimum energy required to generate two new surfaces is the energy needed to break the atomic bonds. (b): Coordinate system for the stress components near the crack tip as used for the description of stress intensity (for plane stress or plane strain).

The stress intensity is a more local criteria for the crack resistance of a material. The stress intensity factor K is a measure of the stresses in the vicinity of a crack tip in a linear-elastic material. For 2D polar coordinates (assuming plane stress or plane strain) as depicted in figure 2.1 (b), the stress field near an ideally sharp crack tip can be written as

$$\sigma_{ij} = \frac{K}{\sqrt{2\pi r}} f_{ij}(\theta) \tag{2.2}$$

Here, $f_{ij}(\theta)$ is a dimensionless function of θ. The stress intensity factor K is a function of the external load as well as the crack dimensions and the specimen geometry. For regions further away from the crack tip, additional, higher-order terms have to be added to equation 2.1.1 to adequately describe the acting stresses. Any loading condition at a crack tip can be thought of as being composed of three basic loading modes (schematically shown in figure 2.2). For mode I loading, there is a tensile stress normal to the local plane of the crack surface. Shear stress parallel to the crack surface and orthogonal to the crack front is called mode II loading, and shear stress parallel to the crack surface and parallel to the crack front is called mode III loading. For any of these fracture modes, a formulation as in equation 2.1.1 can be found. Usually σ, K and f are given a subscript to denote the loading mode. For mixed mode problems, the stresses for each mode can be calculated separately and added together.
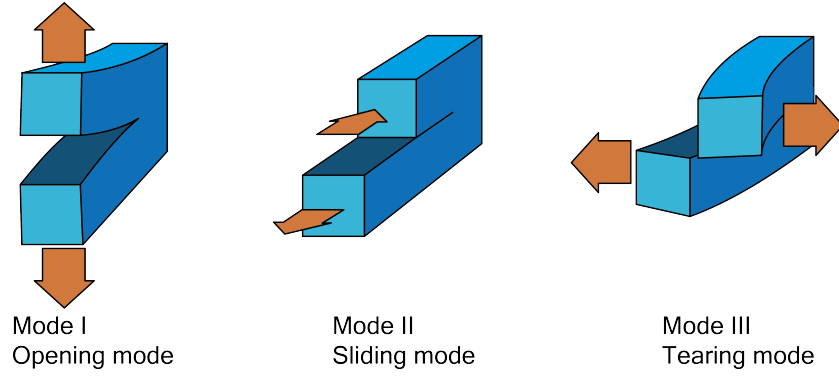
4

Figure 2.2: Decomposition of crack tip loading into three basic modes.

The material's resistance to fracture then can also be described by a critical value K_c, and crack growth is initiated when the stress intensity reaches this value. K_c, like G_c, is assumed to be a material constant.

Calculations for G and K for specific loading conditions, crack geometries and common test specimens can be found in textbook literature [7, 8, 9] or in relevant test standards. Numerical methods are particularly helpful when a 2D approximation of plane stress or plane strain is no longer sufficient to describe the real stress conditions.

For non-linear elastic and elastic-plastic materials, more comprehensive methods for the determination of fracture toughness exist, *e.g.* crack tip opening displacement (CTOD), crack growth resistance curve (R-curve) or the J-integral [7, 8, 9].

2.1.2 Fracture of CFRP

Composites are engineered materials that combine specific properties of its constituent materials, while the composite structure compensates for some of their less desired properties. In the case of CFRP, carbon fibres are embedded in a polymer matrix to obtain a lightweight material with exceptional mechanical properties provided by the high tensile strength of the carbon fibres. This high tensile strength of the fibres is a result of their molecular structure and their small diameter. The latter results in less flaws per length, when compared to a bulk material, and flaws that are limited in size. Furthermore, these flaws tend to be oriented in fibre direction due to the drawing process during manufacturing [10].

At critical loads, carbon fibres exhibit brittle fracture behaviour, *i.e.* there is no load redistribution due to ductile deformation. The high energies released during failure often lead to further fibre fragmentation [11]. If a fibre can move freely, the fragmentation during tensile failure is also partly due to the fact that fibres are much more sensitive to compressive and bending stresses.

For the polymer matrix, different types of polymers can be used, depending on the

desired properties for a respective application. Polymers are subdivided by their microstructure and the resulting properties into thermoplastics, elastomers and thermosets. The polymer matrix in a composite generally determines many mechanical, thermal or chemical properties of the composite, while the fibres determine tensile strength in fibre direction or most electrical properties. Furthermore, the matrix holds the fibres in place, redirects forces between fibres, carries the load in transverse and shear direction, can act as a crack stopper and protects the fibres from environmental influences [10].

Polymers are a family of materials with a considerable range in failure behaviour [12]. The failure behaviour of polymers is affected by the applied stresses, material flaws, temperature, load history and the environment [12, 13]. Due to their wide range, the various possible fracture mechanisms of polymers are not discussed here. Within the scope of this work, one partially cross-linked thermosetting polymer and three different semi-crystalline thermoplastic polymers were investigated. While fracture of the former is mostly brittle and linear fracture mechanics can be applied in most cases, fracture of the latter can be brittle, accompanied with large plastic deformations or show other modes of fracture like crazing. The failure modes of semi-crystalline thermoplastics depend on the micro structure of the material and the loading conditions [14]. Further details are discussed in chapter 3, where the results of the polymer tests are presented.

The specific mechanical properties of CFRP strongly depend of the layout of the material. Typically, the fibres are arranged in a layered setup. In each layer, the fibres are arranged in parallel, with a typical fibre volume fraction of 60-70%. The fibre orientation in neighbouring layers can differ, depending on the layer setup chosen for a specific application. Due to the highly anisotropic mechanical properties of CFRP structures and various possible loading conditions, the accumulation of damage and the evolution of failure in these structures can be quite complex.

The most basic setup is a small volume of unidirectional (UD) composite. Here, the failure mechanisms that can occur are strongly dependent on the stresses acting on the volume. These failure modes can be classified as fibre fracture and inter-fibre fracture. For the latter, the failure occurs in the matrix material or in the interface between fibres and matrix. Fibre fracture is a result of tensile and compressive stresses acting in parallel to the fibre direction, though both cases are accompanied by severe matrix damage. For compressive stresses, shear buckling can be observed, while failure under tensile stresses can be preceded by inter-fibre failure and fibre pull-out. Tensile and compressive stresses acting perpendicular to the fibre direction as well as all possible shear stress configurations will result in inter-fibre fracture when the respective values in fracture strengths are reached.

Another failure mode comes into play when at least two UD layers are combined, that is failure of the interface between these layers. This type is generally called delamination and can occur for different loading configurations.

Even though the failure behaviour in composites can be rather complex, accurate theoretical descriptions have been developed to predict it. Here, usually two independent fracture criteria for fibre and inter-fibre fracture are applied [15, 16].

6

However, composite failure investigated in the context of this text is limited to inter-ply delamination under mode I and mode II loading conditions as well as failure of CFRP laminates with different layer arrangements under bending loads.

Depending on the mode of the applied load, delamination failures in composite laminates initiate and propagate under the influence of normal or shear stresses, or respectively under a combination of both for various mode mixities. Here, the interlaminar shear toughness of CFRP is often greater than its normal out-of-plane toughness [17].

As for any material, flexure induces both tensile and compressive stress areas in a CFRP laminate. If the material is bend downwards, the top layers are under compressive stresses, while the bottom layers experience tensile stresses. Depending on the fibre directions in a certain layer, one or more of the failure modes mentioned above can occur when the respective ultimate strengths are reached. Usually, flexural failure originates in areas of compressive stress due to a much lower failure resistance. Here, effects like fibre microbuckling and subsequent plastic kinking may occur [18]. Increasing inter-laminar shear stresses between the layers may then result in delamination. Finally, fibre pull-out and fibre fracture may be observed in the zones of tensile stresses [19].

2.2 Acoustic emission

2.2.1 Fundamentals

Acoustic emission (AE) analysis deals with transient mechanical waves generated by the sudden release of stored elastic energy within a body. These waves can be described using elastic wave theory [20, 21]. With simplifying assumptions (infinite, isotropic medium) there are two basic solutions, *i.e.* longitudinal waves and transversal waves that travel independently. For finite media, the solutions depend on the boundary conditions, and one type of wave can be converted to the other, *e.g.* when wave reflection or refraction occurs.

Usually, source mechanisms of interest are dislocations, crack growth and propagation or even plastic deformation. The elastic waves manifest themselves as surface motions of the body, which can then be converted to a voltage signal by acoustic sensors and transducers attached to the surface.

The AE signals can contain valuable information about the location and the characteristics of the source. However, the information from the source can be considerably altered before it is recorded [22, 23, 24]. The chain of signal altering mechanisms can be expressed mathematically by a series of convolutions, starting with a source function S which represents the local dynamics of an AE source, *e.g.* a dislocation motion or a crack. According to the convolution theorem, this series can be rewritten as a series of multiplications in the frequency domain, which then can be interpreted as a sequence of linear filters. Figure 2.3 shows the change in signal form along the propagation chain.
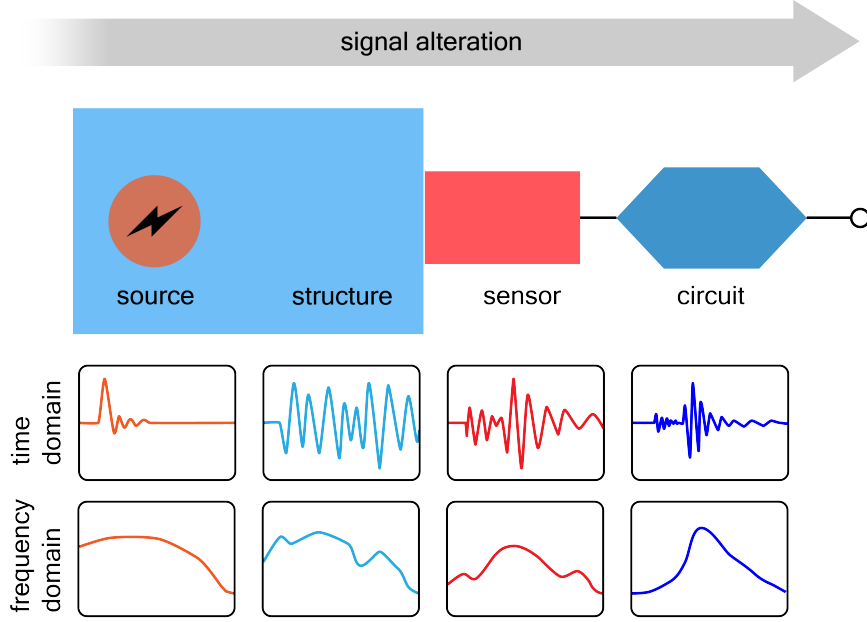
Figure 2.3: Alteration chain of acoustic emission signal from source dynamics to recorded voltage signal.

Therefore, the main goal of acoustic emission analysis is to understand the complex mechanisms and to draw accurate conclusions about the source characteristics from the recorded AE signals. For each step in this chain, detailed theoretical models have been developed over the past decades.

The first successful attempts of linking the surface displacement generated by an acoustic wave to the source dynamics were made in the 1970s and 1980s. The generalised theory of acoustic emission [25, 26] presents a method to calculate the displacement at any point in a medium (*e.g.* at its surface) depending on the source function and the influence of the medium [23]:

$$\mathbf{u}(\mathbf{r}, t) = \mathbf{G}(\mathbf{r}, \mathbf{r}_S, t) \circledast S(t)\mathbf{M} \qquad (2.3)$$

The AE source is represented by a source time function $S(t)$ which describes the temporal behaviour of the source and the moment tensor $\mathbf{M}_{ij} = C_{ijkl}d_k n_l \Delta V$ which describes the source kinematics. Here, C_{ijkl} is the elasticity tensor, d is the unit vector for the crack movement direction, n is the unit vector normal to the crack surfaces and ΔV is the crack volume. The influence of the (isotropic) medium is described by the Green's function $\mathbf{G}(\mathbf{r}, \mathbf{r}_S, t)$. This function represents the response of the displacement at $\mathbf{r}$ to a source pulse at $\mathbf{r}_S$. Typically, these function have to be calculated numerically, and they depend on the material properties of the medium, its geometry and boundary conditions.

8

However, since the desired information is the source time function, the equation is usually solved for $S(t)$ by deconvolution. Here, the Green's function has to be calculated precisely, and the moment tensor has to be modelled to accurately represent the crack. Getting additional information about the source, *e.g.* the source intensity or orientation, becomes increasingly more difficult the more complex the propagation path gets, *i.e.* when anisotropy, inhomogeneities, limited material extension in one or more dimensions, scattering, reflection, attenuation or dispersion have to be considered. Although analytical solutions have been proposed for special geometries such as composite laminates [27, 28], they are usually accompanied by certain simplifying assumptions.

The signal measured by an AE sensor can be described mathematically as the convolution of the sensor input (mechanical motion) with the impulse response of the sensor [23]. Any additional circuit elements, such as filters and amplifiers, can also be described by their respective transfer functions. The most commonly used types of AE sensors are piezoelectric sensors, which convert surface motion, mostly motion perpendicular to the surface, to a voltage signal. Depending on the size of the sensor aperture, the sensor excitation is an average of the surface displacement[29]. Analytical approaches to acquire a sensor's response function may require solving the piezoelectric equations, but finding analytical solutions for finite 3d bodies (typical geometries for the piezo elements used in AE sensors are discs, cones or ring structures) can be quiet challenging. Alternatively, the response function can be determined experimentally by calibration tests [30].

More recent methods to correlate AE signals with certain source types rely on numerical methods, *e.g.* finite element method (FEM) simulations of the medium and the AE source. FEM is a powerful numerical method used to obtain approximate solutions of partial differential equations with specific boundary conditions for any given geometry. These numerical methods have helped to broaden the understanding in many areas of acoustic emissions research, *e.g.* source type studies [31], AE propagation in wave guides [32] and AE sensor development [33]. Furthermore, multi-scale approaches can be applied to simulate the complete AE signal evolution from a growing crack to the voltage signal acquired by the measurement equipment [34].

2.2.2 Acoustic emission of CFRP

AE analysis is an excellent tool for the structural health monitoring of CFRP structures or for the investigation of the evolution of failure in CFRP components in general. As outlined in section 2.1.2, various different failure modes can occur in CFRP. The goal of AE analysis is to extract information on the type of damage from the measured AE signals. Due to the differences in crack durations, energies released or crack volumes between for example fibre fracture and matrix failure, one might expect AE signals with clearly distinguishable AE signal characteristics. However, additional influences like location, depth and orientation of the AE sources as well as considerable AE signal alteration along the propagation path can complicate

the analysis. This is particularly the case for CFRP, since the material is highly anisotropic and the investigated composite structures often act as wave guides. Furthermore, multiple signals emitted by different source types during fracture might overlap in time.

A comprehensive compilation of AE analysis procedures including state of the art methods is given in [35]. According to [35], classical methods for AE source identification, like moment tensor inversion which is briefly discussed in the previous section, which are well established for volumetric, isotropic materials, are not applicable for CFRP, which is often manufactured in structures whose spatial extent is strongly restricted in one dimension. This spatial restriction leads to the formation of specific wave modes, *e.g.* symmetric and anti-symmetric Lamb waves in plate-like structures. These guided wave modes can contain useful information about the source mechanism. Analysis of guided acoustic wave modes and their propagation behaviour, often referred to as modal AE methods, allows for the identification and distinction of particular source mechanisms [36, 37].

Another, more recent approach for AE signal identification in CFRP is the use of pattern recognition techniques. Here, for each recorded transient AE signal, a set of appropriate features are calculated. Classification algorithms are used to find similarities and group the AE signals into natural clusters [38]. These clusters then may be assigned to certain sources, *e.g.* different failure modes, background noise or electrical interference signals. Attributing a specific failure type to a group of signals can be done by conducting experiments where the failure mode Is known or by signals obtained from simulations of specific failure modes [39].

However, AE analysis for failure of composite structures can be quite intricate and still faces major obstacles. For example, failure and the respective AE signals in CFRP are highly dependent on the material configuration and the loading conditions. The measured AE signals strongly depend on the propagation path from source to sensor as well as the frequency characteristics of the applied AE sensor. Furthermore, friction of existing crack surfaces also generates AE signals that have to be filtered from the desired data. For the latter cases, measuring the simultaneously generated EME signals may be useful to overcome these difficulties.

2.3 Electromagnetic emission

2.3.1 Overview

Electromagnetic emission is a term that comprises a wide range of emission effects that occur when materials undergo mechanical processes such as fracture [40, 41], plastic deformation [42, 43] or friction [44, 45]. The frequencies of the emitted electromagnetic radiation range from a few Hertz up to the terahertz regime, while the EME of induced or secondary effects like gas discharges between charged crack sides may have even higher frequencies. In a broader sense, the term EME can also include the emission of charged particles during material failure (sometimes referred to as fracto-emission [46, 47]).

EME effects over a wide range of frequencies were observed for a large variety of materials, *e.g.* rocks, minerals and concrete [40, 48, 49, 50, 51], glass [41, 52, 53], ceramics [54, 55], metals and alloys [42, 56, 57, 58], polymers [59], ice [60, 61] or polymer-matrix composites [62, 63, 64] and concrete composites [65]. EME generated during failure of the interfaces between two different materials was also observed [66, 67]

Although there has been some research concerning EME generated by fracture of fibre-reinforced polymers and its components in the past [68, 69, 70], the full potential of the EME analysis has yet to be explored.

The analysis of EME can be a useful tool to study crack formation and propagation. It can provide real-time information of microscopic failure, such as the duration of crack propagation or the frequencies of the crack wall vibrations [41, 71, 72]. Furthermore, EME with a distinct directionality has already been reported for some materials [45, 73, 74]. This characteristic field distribution of the fracture-generated EME signals can offer additional insight into different failure mechanisms.

Beyond the study of the source mechanism, possible applications range from potential early warning methods to condition monitoring, as EME has been measured as precursors to earthquakes [75, 76] and avalanches [77] or is used to monitor rock bursts in coal mines [78].

2.3.2 Source model

The mechanisms of EME generation have been the subject of research for many years, and multiple theories for the sources of EME in different materials and for different failure modes have been proposed. However, a consistent model for the description of all experimental results concerning EME has yet to be proposed.

In general, the temporal characteristics of EME signals generated by fracture are correlated to a change in charge distribution and its dynamics, both dictated by the fracture processes. Most theories presume these dynamics of charges to be the source of EME [68, 71, 73]. Some authors have pointed to the charge separation or electrification of the crack surfaces to be an important source process [45, 79, 80] . Some authors consider vibrations of the charged crack surfaces in the form of charge surface vibrational waves [41, 50, 81] as sources. Other effects are discussed too, *e.g.* polarisation effects [82, 83] , piezoelectric effects [84] and secondary emission effects such as light emitted by gas discharges in crack openings [53].

Considering the wide range of materials investigated with widely varying mechanical and electrical properties, the different types of loading conditions and also the different methods of measuring the EME signals, the resulting variety of theories is not surprising. Thus, it can be assumed that EME, depending on the circumstances, is generated (and also influenced) by different processes. In any case, fracture-induced EME signals contain valuable information about their sources. A detailed understanding of the source mechanisms is therefore of vital importance for the analysis of the signals.

The source model proposed here, is a basic model based on the results presented in the next chapters. It comprises and combines some elements of the models listed above. Figure 2.4 schematically shows the main components of this model for a mode I crack. For other fracture modes, the source mechanisms may differ in some aspects, but the basic principle is assumed to also apply. Furthermore, plastic deformation of the material is neglected here, because most of the materials under investigation in this text show little or no plastic deformation before fracturing. Nevertheless, plastic deformation has been shown to generate EME, and there are different models to describe this phenomenon.
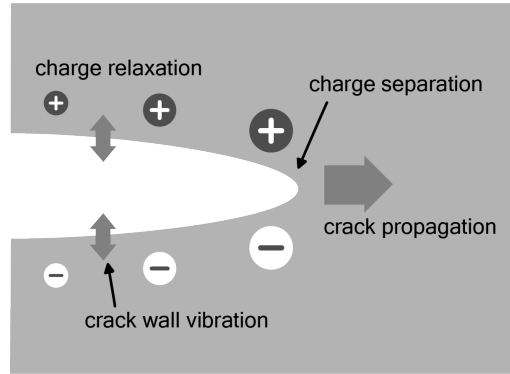

Figure 2.4: Schematic of proposed source mechanism: Build-up of asymmetric net surface charges at the crack tip due to charge separation, vibrations of charged crack surfaces and charge relaxation processes.

The model proposed here attributes the characteristics of the generated EME to three main processes:

The first process is the charge separation due to the formation of new crack surfaces. When a crack is formed and then propagates, molecular bonds break, and a charge distribution arises at the crack surfaces. For EME signals of significant strength to be generated, the charge separation is required to be asymmetrical in some way. The reasons for this asymmetry are unclear. Different theories for possible mechanisms exist, though some authors argue against a break of symmetry.

The second contribution to EME signal shapes is the decay of the newly generated charge distribution. This process starts as soon as charges are generated. The specific processes may differ, depending on the material properties and the crack geometry. Suitable candidates for these processes are charge relaxation and charge recombination. The time constants for these processes are determined by the electrical properties of the material. Due to these first two contributions, the EME signal strength increases as long as new crack surfaces are formed and then decreases with a material-specific time constant.

As long as the charges are present, their spatial distribution can also change over time. These charge dynamics are the third contribution to the EME signal characteristics. An example of such dynamics are the vibrations of the charged crack surfaces. Vibrations of charged surfaces lead to oscillating surface dipoles which

generate EME signals of certain frequencies. The specific frequencies of the oscillations may depend on the crack mode, the crack geometry and dimensions or the material properties. Dampening of these oscillations can be mechanical, with a close relation to the simultaneously generated AE signals, or depend on the relaxation of the charges themselves.

An extensive calculation for EME signals generated by these first two effects is presented in [72] for the assumption of a propagating crack as an electric dipole. For the material parameters used in this publication, the derived electric field at the sensor has a fast rise governed by the time-dependent crack geometry and length and a slower exponential decay determined by the charge relaxation time. Considerations regarding EME signals generated by charge vibrations comprise oscillations of actual dipoles consisting of opposite charges on opposite crack sides [85] or surface vibrational waves where positive charges move together in a diametrically opposite phase to the negative ones [81].

2.3.3 Description of dominant fields

The basic set of equations when dealing with electromagnetic fields in matter above the microscopic scale are Maxwell's equations:

$$
\begin{aligned}
\nabla \cdot \mathbf{D} &= \varrho & (2.4) \\
\nabla \times \mathbf{E} &= -\partial_t \mathbf{B} & (2.5) \\
\nabla \cdot \mathbf{B} &= 0 & (2.6) \\
\nabla \times \mathbf{H} &= \mathbf{j} + \partial_t \mathbf{D} & (2.7)
\end{aligned}
$$

with the electric field $\mathbf{E}$, the magnetic field $\mathbf{B}$, the charge density ρ and the current density $\mathbf{j}$. The displacement field $\mathbf{D}$ and the magnetic field $\mathbf{H}$ include the material response to electric and magnetic fields, *i.e.* the magnetisation $\mathbf{M}$ and the polarisation $\mathbf{P}$:

$$
\begin{aligned}
\mathbf{D} &= \varepsilon_0 \mathbf{E} + \mathbf{P} & (2.8) \\
\mathbf{H} &= \frac{1}{\mu_0} \mathbf{B} - \mathbf{M} & (2.9)
\end{aligned}
$$

ε_0 and μ_0 are the permittivity and the permeability of free space.

It is not always necessary to use the full set of coupled differential equations. For all cases considered in this text, the fields and their sources are related to the dynamics of the fracture processes. Given the typical time scales of crack propagation and

crack wall oscillation, the frequencies ω of the arising electric field are limited to a few megahertz. The dimensions of sources and sensors, respectively the distances between them, are of the order of the characteristic length d which is much smaller than the wavelengths λ of the occurring field, $i.e.\ d \ll \lambda$. In terms of time scales, the propagation time $\tau_{em} = d/c$ an electromagnetic wave needs to travel the distance d at the speed of light c is small compared to the time scales of the source mechanisms $\omega^{-1} = \tau \gg \tau_{em}$.

According to Helmholtz's theorem, the electric field $\mathbf{E}$ can be decomposed into a solenoidal (divergence-free) and an irrotational (curl-free) component, $i.e.\ \mathbf{E} = \mathbf{E}_{sol} + \mathbf{E}_{irr}$. Furthermore, the electric and magnetic fields can be written in their potential representation: $\mathbf{B} = \nabla \times \mathbf{A}$ and $\mathbf{E} = -\nabla\Phi - \partial_t \mathbf{A}$ with the vector potential $\mathbf{A}$ and the scalar potential Φ. Hence, $\mathbf{E}_{irr} = -\nabla\Phi$ and $\mathbf{E}_{sol} = -\partial_t \mathbf{A}$. Equations 2.4-2.7 in the Coulomb gauge ($\nabla \times \mathbf{A} = 0$) give:

$$\Phi(\mathbf{r},t) = \frac{1}{4\pi\varepsilon_0} \quad \int d^3r' \frac{\varrho(\mathbf{r},t)}{|\mathbf{r}-\mathbf{r}'|} \tag{2.10}$$

$$\mathbf{A}(\mathbf{r},t) = \frac{\mu_0}{4\pi} \quad \int d^3r' \frac{\mathbf{j}(\mathbf{r},t-|\mathbf{r}-\mathbf{r}'|/c) - \varepsilon_0 \partial_t \nabla\Phi(\mathbf{r},t-|\mathbf{r}-\mathbf{r}'|/c)}{|\mathbf{r}-\mathbf{r}'|} \tag{2.11}$$

with $\Phi(\mathbf{r},t)$ being the static potential (electric near field). The case $d \ll \lambda$, which is equivalent to $\tau_{em} = d/c \ll 1/\nu = \tau$, leads to $t_{ret} = t - |\mathbf{r} - \mathbf{r}'| /c \cong t$. This leads to the following approximation for the vector potential:

$$\mathbf{A}(\mathbf{r},t) \cong \frac{\mu_0}{4\pi} \quad \int d^3r' \frac{\mathbf{j}(\mathbf{r},t) - \varepsilon_0 \partial_t \nabla\Phi(\mathbf{r},t)}{|\mathbf{r}-\mathbf{r}'|} \tag{2.12}$$

As shown in [86], the following approximation of Maxwell's equations is solved by these potentials:

$$\nabla \cdot \mathbf{D}_{irr} = \varrho \tag{2.13}$$

$$\nabla \times \mathbf{E}_{sol} = -\partial_t \mathbf{B} \tag{2.14}$$

$$\nabla \cdot \mathbf{B} = 0 \tag{2.15}$$

$$\nabla \times \mathbf{H} = \mathbf{j} + \partial_t \mathbf{D}_{irr} \tag{2.16}$$

with:

$$\mathbf{D}_{irr} = \varepsilon_0 \mathbf{E}_{irr} + \mathbf{P} \tag{2.17}$$

$$\mathbf{H} = \frac{1}{\mu_0} \mathbf{B} - \mathbf{M} \tag{2.18}$$

This set is called the quasi-stationary approximation, since propagation effects of the fields can be neglected, *i.e.* the fields can be considered to propagate instantaneously, and retardation effects are negligible.

With linear, time-independent, isotropic material properties σ, ε and μ, further approximation can be made. This results in $\mathbf{D} = \varepsilon \mathbf{E} = \varepsilon_0 \varepsilon_r \mathbf{E}$, $\mathbf{H} = (1/\mu)\mathbf{B} = (1/\mu_0\mu_r)\mathbf{B}$ and $\mathbf{j} = \sigma\mathbf{E}$. Furthermore, as shown in [86], the condition $d \ll \lambda$ leads to

$$\nabla \cdot \mathbf{E}_{irr} = \frac{\varrho}{\varepsilon} \tag{2.19}$$

$$\nabla \times \mathbf{E}_{sol} = -\partial_t \mathbf{B} \tag{2.20}$$

$$\nabla \cdot \mathbf{B} = 0 \tag{2.21}$$

$$\nabla \times \mathbf{B} = \sigma \mathbf{E}_{irr} + \sigma \mathbf{E}_{sol} + \varepsilon \partial_t \mathbf{E}_{irr} \tag{2.22}$$

Here, the part of the polarisation $\mathbf{P}_{sol} = \varepsilon_0 \chi_{el} \mathbf{E}_{sol}$ connected to the solenoidal component of the electric field is also neglected. This additional restriction is reflected in a smaller range of validity of these equations, *i.e.* $\tau \gg d/c$ where $c = 1/\sqrt{\varepsilon\mu} = 1/\sqrt{\varepsilon_0 \varepsilon_r \mu_0 \mu_r}$ now is the propagation velocity of the electromagnetic fields in the materials present.

Since all experiments presented in this text were carried out in a shielding enclosure, the volume under consideration is limited, and $d \ll \lambda$ is, for the frequency ranges under consideration, valid for all cases. Thus, the quasi-stationary approximation describes the occurring fields with sufficient accuracy.

Based on frequency ranges, relaxation times and geometric properties considered, further approximations to the equations describing the fields can be made [86, 87, 88].

For the source model proposed in section 2.3.2, the EME is generated by net charges on the opposite crack surfaces and their temporal behaviour. If the time variation of the charge distributions are slow compared to the time the fields need to travel through the volume under consideration, inductive effects can be neglected and the electric field can be approximated by its quasi-static field $\mathbf{E}_{irr} = -\nabla\Phi$. In this case, the dominating coupling between conductors and the electric field is capacitive [89]. This is the basic assumption for the considerations in the following chapter.

2.4 Measurement of EME

2.4.1 Capacitive coupling and equivalent circuit

As mentioned at the end of the previous chapter, certain assumptions for the material properties and especially for the geometry of the conductors allow for the quasi-static approximation of the electric field. For these cases, the dominant electrical characteristic of the conductors used as sensors is their capacitance [89], and the coupling between electric field and sensor is mainly capacitive. In this section, a suitable equivalent circuit for the capacitive sensor is derived, which will then then be used for the analysis of the measurement circuit in the next section.

The self-capacitance of an isolated conductor, *i.e.* the ratio of the electric charge it carries and the resulting electric potential, depends solely on its geometry. If multiple conductors are present, the electric potential Φ_i of the i-th conductor is a linear function of the charges Q_j on all conductors, which is usually expressed as:

$$Q_i = \sum_{i,j} c_{ij} \Phi_j \tag{2.23}$$

The capacitance matrix is symmetric, and its coefficients c_{ij} represent the influences of the given shapes, positions and relative distances of the conductors.
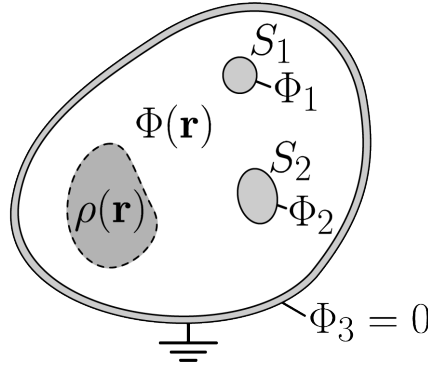

Figure 2.5: Schematic of exemplary configuration of conductors near a charge distribution. Both conductors are at equipotential. The setup is enclosed with a grounded conducting shell.

The following derivation is a slight modification of a derivation given by Partridge in [89]. The starting point is the situation as shown in figure 2.5. Two isolated (*i.e.* not connected to ground or any load) conductors (in the following called "sensors") are placed near a charge distribution (in the following called "source") which is spatially restricted to a small volume (*e.g.* a test specimen). Both conductors and the charge distribution are placed in a conducting, grounded enclosure. The surface of each

sensor is at equipotential due to surface charges induced by the source as well as the surface charge distributions on the enclosure and the other sensor. Since the sensors are not connected to ground, the net charge of each sensor is zero. Therefore:

$$Q_1 = 0 = \quad c_{11}\Phi_1 + c_{12}\Phi_2 + c_{13}\Phi_3 + Q_{1,\varrho} \tag{2.24}$$

$$Q_2 = 0 = \quad c_{21}\Phi_1 + c_{22}\Phi_2 + c_{23}\Phi_3 + Q_{2,\varrho} \tag{2.25}$$

where $Q_{i,\varrho}$ is the surface charge of sensor i induced by the source. Furthermore, the conducting shell is grounded, $i.e.$ $\Phi_3 = 0$. If the two sensors are now electrically connected ($i.e.$ by a wire, which itself is assumed to have a negligible effect on the field and charge distribution) and $\Phi_1 \neq \Phi_2$, charges will flow from one sensor to the other until both sensors are at the same potential, $i.e.$ $\Phi_1' = \Phi_2' = \Phi_{total}$ (quantities after the connection of the sensors are appended with the prime symbol). Here, the geometry is not changed, therefore the capacitance coefficients do not change either.

$$Q_1' \quad = c_{11}\Phi_{total} + c_{12}\Phi_{total} + c_{13}\Phi_3' + Q_{1,\varrho}' \tag{2.26}$$

$$Q_2' \quad = c_{21}\Phi_{total} + c_{22}\Phi_{total} + c_{23}\Phi_3' + Q_{2,\varrho}'. \tag{2.27}$$

With $\Phi_3' = \Phi_3 = 0$ and $Q_{i,\varrho}' = Q_{i,\varrho}$ (here, changes of the source charge distribution due to changes of the sensor charges are neglected), it follows that:

$$Q_1' - Q_1 \quad = \quad \Delta Q = c_{11}(\Phi_{total} - \Phi_1) + c_{12}(\Phi_{total} - \Phi_2) \tag{2.28}$$

$$Q_2' - Q_2 \quad = - \quad \Delta Q = c_{21}(\Phi_{total} - \Phi_1) + c_{22}(\Phi_{total} - \Phi_2). \tag{2.29}$$

Rearranging for Φ_{total} leads to:

$$\Phi_{total} = \frac{c_{11} + c_{12}}{c_{total}}\Phi_1 + \frac{c_{21} + c_{22}}{c_{total}}\Phi_2 \tag{2.30}$$

where $c_{total} = c_{11} + c_{12} + c_{21} + c_{22}$ is the capacitance of the resulting sensor composed of the two connected conductors.
This result implies equivalent circuits for the sensors as shown in figure 2.6, with $C_1 = c_{11} + c_{12}$ and $C_2 = c_{21} + c_{22}$.
The above derivation was done for two conductors that initially had a certain spatial extent and surface charge distribution. These conductors can be considered as a
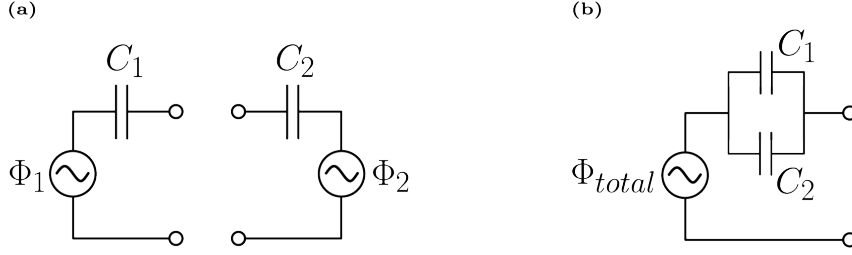
Figure 2.6: Schematic of an equivalent circuit of two capacitive sensors with capacitances C_i being at the potential Φ_i. When the sensors are connected, their capacitances are added (connected in parallel), and their common potential changes to Φ_{total}

.

composition of n smaller conductors that were successively connected the same way as the two sensors in the above example. In this case, the surface charge distribution can be considered the result of n charge exchanges. Furthermore, any kind of sensor geometry can be considered to be a composition of n smaller sensors, each too small to noticeably alter the original electric potential at its position. The electric potential at the sensor then is the sum of all original (before the sensor is placed) values Φ_n of the potential at the positions of the n-th fraction of the conductor, weighted with its capacitances.

$$\Phi_{total} = \frac{\sum_{i,j=1}^{n} c_{ij}\Phi_i}{\sum_{i,j=1}^{n} c_{ij}} \tag{2.31}$$

This result is derived considering potentials with respect to a common reference (ground). The same result is obtained when potential differences between conductors are considered and the respective capacitance matrix elements, *i.e.* $C_i = C_{ii} = \sum_{j=1}^{n} c_{ij}$ and $C_{ij} = -c_{ij}$ are used:

$$\Phi_{total} = \frac{\sum_{i=1}^{n} C_i\Phi_i}{\sum_{i=1}^{n} C_i} \tag{2.32}$$

For the transition to a continuous conductor, the sum becomes an integral over the volume of the sensor.

$$\Phi_{total} = \frac{\int\limits_{V_c} c(\mathbf{r})\Phi(\mathbf{r})d^3r}{\int\limits_{V_c} c(\mathbf{r})d^3r} \tag{2.33}$$

Here, V_c is the volume of the conductor. $c(\mathbf{r})$ is the capacitance of the infinitesimal volume element at the position $\mathbf{r}$, which is the total charge of the volume element when its potential is 1 V and all other elements are grounded. $\Phi(\mathbf{r})$ is the electric potential at position $\mathbf{r}$ in the absence of the conductor. In an external electric field, there is no difference in the surface potential of a solid conductor and a hollow conductor of the same geometry. Thus, equation 2.33 can be rewritten to a surface integral:

$$\Phi_{total} = \frac{\int\limits_{\partial V_c} c(\mathbf{r})\Phi(\mathbf{r})d^2r}{\int\limits_{\partial V_c} c(\mathbf{r})d^2r} \tag{2.34}$$

where ∂V_c is the surface of the conductor, $c(\mathbf{r})$ is the capacitance of the infinitesimal surface element at the position $\mathbf{r}$ and $\Phi(\mathbf{r})$ is the electric potential at position $\mathbf{r}$ in the absence of the conductor, as shown in figure 2.7 (a). Figure 2.7 (b) shows the respective equivalent circuit.
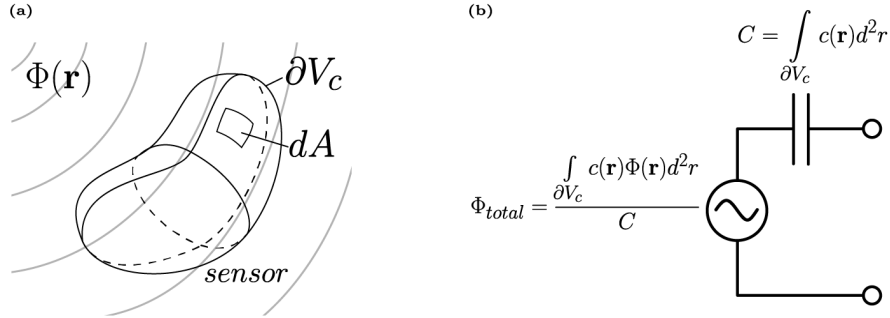

Figure 2.7: (a) Schematic of the undisturbed, location-dependent electric potential and the surface of a conductor placed at a certain position to measure the potential via capacitive coupling. (b) The resulting potential is the weighted (according to the sensors capacitances) average of the previous undisturbed potential.

Since the electric potential generated by the source charges is averaged over the volume of the detecting capacitive sensor, the specific geometry of the sensor can have a significant influence on the measured potential. If a precise measurement of the location-dependent magnitude of the electric potential is required, the dimension of the chosen sensor should be smaller than the distance of considerable change in potential.

Figure 2.8 (a) schematically shows the principle that is the basis of all EME measurements presented in this work. A fracturing specimen is the source for a time and
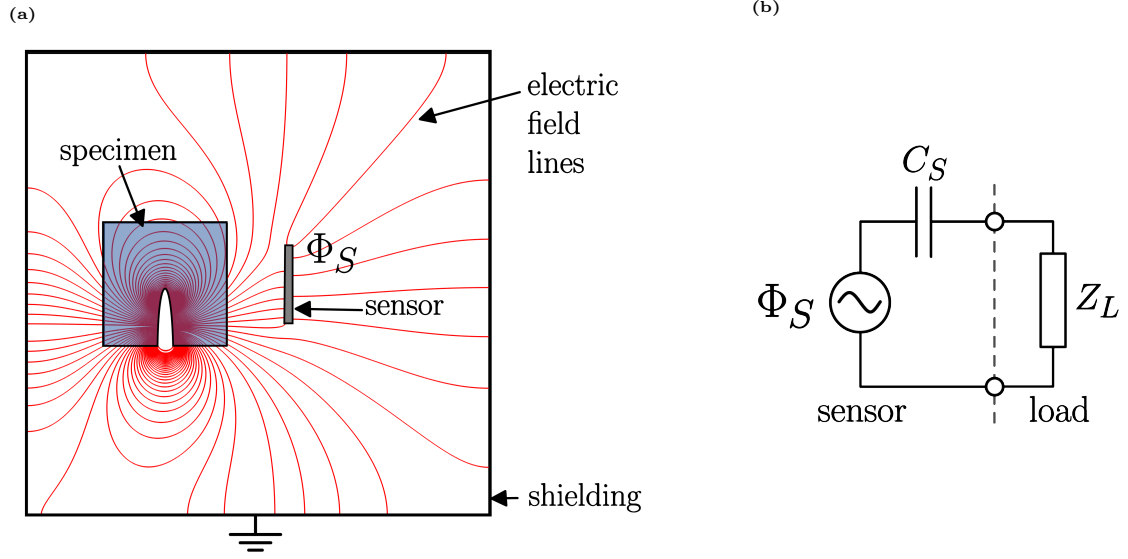
Figure 2.8: (a): Principle of a capacitive sensor picking up an electric field generated by charges on the crack surfaces of a specimen. (b): Equivalent circuit of capacitive sensor with attached load impedance.

location-dependent charge distribution which gives rise to an time and location-dependent electric field. As a sensor, a conductor is placed near the source and capacitively couples with the electric field. Connecting the sensor with a load, see figure 2.8 (b), then allows for the measurement of a voltage signal. The grounded shielding enclosure also serves as reference for the voltage measurement. The measured quantity here is the electric potential. For the measurement of the actual electric field strength, a slightly different approach is needed.

A basic principle of electric field measurement using capacitive coupling requires an electric dipole, *i.e.* a configuration of two conductors (*e.g.* a dipole antenna). For this kind of configuration, the sensitivity of the sensor can be given by its effective length:

$$V_{oc} = -\mathbf{l}_{eff} \cdot \mathbf{E}_{inc} \tag{2.35}$$

with V_{oc} being the open circuit voltage between the terminals of the sensor. The effective length vector $\mathbf{l}_{eff}$ solely depends on the sensor's geometry and usually is defined by equation 2.35. $\mathbf{l}_{eff}$ can be calculated (analytically for special cases [89] or numerically) or be determined by calibration, using known calibration fields [90]. To satisfy the open circuit condition, the sensor is connected to a high load impedance (with respect to the sensor impedance: $Z_L \gg 1/i\omega C$). Since equation 2.35 contains the vector product $\mathbf{l}_{eff} \cdot \mathbf{E}_{inc}$ and $\mathbf{l}_{eff}$ is constant for a fixed sensor configuration, the measured sensor voltage depends on the magnitude of the electric field at the sensor

position as well as the angle between the incident field and the sensor orientation (given by $\mathbf{l}_{eff}$).

For the experiments presented in this text, the direct measurement of the electric field strength using passive capacitive sensors was not implemented, mainly for two reasons: The signal to noise ratio of the sensor limits the measurable voltage differences. Therefore it is much more convenient to measure the voltage between one conductor near the source and the grounded shielding enclosure than to measure the voltage difference between two conductors near the source. Furthermore, the correlation between the electric field and the sensor potential (*e.g.* as expressed by the effective length) changes with any change in the setup. Since most of the experiments require at least some parts to be moving (*e.g.* the specimen and the attached AE and EME sensors), this correlation is time-dependent. The determination of this time-dependent correlation, either by calculation or by calibration, was not attempted here.

Nevertheless, the measurement of the potential at the sensor may also result in valuable information. For certain frequency ranges, as will be discussed in the next section, the sensor potential is a direct function of the charge dynamics in its vicinity, while the charge dynamics are assumed to closely correlate with the fracture process. A useful concept for determining the electric signals at conductors induced by moving charges was presented by [91] and [92]. Here, the authors showed that, for the electrostatic case, the current in a grounded conductor (sensor) induced by a moving point charge is given by:

$$I_S(t) = \frac{q}{1V} \mathbf{E}' \cdot \mathbf{v}_q(t) \qquad (2.36)$$

where q is the charge and $\mathbf{v}_q$ is its velocity (see figure 2.9 (a)). $\mathbf{E}'$ is the electric field that would arise when the charge q is removed, the sensor is set to a constant voltage of 1 V, and all other conductors are grounded (schematically shown in figure 2.9 (b)). If the direction of the charge movement is known, *e.g.* for known crack orientations, equation 2.36 can be used to optimise the sensor positioning for maximum signal strength. On the other hand, this concept can be applied to determine the movement direction of charges. A simple and commonly used sensor setup, in this work as well as in other publications, is the parallel plate capacitor setup. For this setup, the specimen is located between two parallel plates, where either one plate serves as ground while the other serves as the sensor or both are used as sensors (figure 2.9 (b)). Depending on plate sizes and distances, the electric field $\mathbf{E}'$ between the plates is mostly directed perpendicular to the plates and is constant. This proves particularly useful, since the induced electric signal then only depends on the charges velocity but is independent of its position.
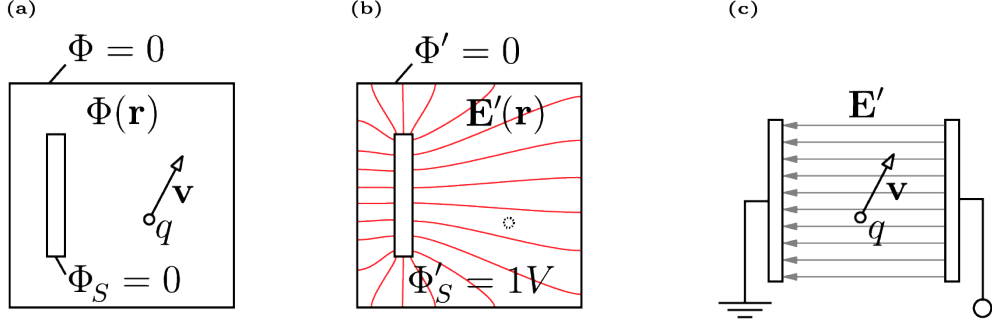
Figure 2.9: (a) Basic setup to illustrate the underlying concept of equation 2.36 . (b) $\mathbf{E}'$ is the imagined electric field resulting from removing all charges and setting the sensor plate voltage to 1 V. (c) Plate capacitor setup as exemplary application for equation 2.36.

2.4.2 Measurement setup and measurement circuit

As discussed in the previous section, a capacitive sensor in a quasi-stationary electric field is at an equipotential with a value corresponding to an averaged value of the potential at its position. Connecting the sensor to a load impedance allows for the measurement of this value as a voltage signal. The simplest circuit is a load impedance that consists of only a resistor, with $Z_L = R$. The circuit then equals a first order high-pass filter. The complex transfer function is the ratio of the complex output and input voltages (or in this case the voltage the resistor $\underline{V}_R$ and the sensor voltage $\underline{V}_S$) and reads:

$$\underline{G}(i\omega) = \frac{\underline{V}_R}{\underline{V}_S} = \frac{i\omega RC}{1 + i\omega RC} \tag{2.37}$$

With the cutoff frequency $\omega_c = 1/RC$ the division of $\underline{G}(i\omega)$ into its amplitude and phase parts leads to the common expressions:

$$G(\omega) = |\underline{G}(i\omega)| = \frac{\omega/\omega_c}{\sqrt{1 + (\omega/\omega_c)^2}} \tag{2.38}$$

$$\varphi(\omega) = \arctan\left(\frac{1}{\omega/\omega_c}\right) \tag{2.39}$$

Figure 2.10 (a) shows the RC circuit with values for R and C that are typical for the setups used in this work, while figure 2.10 (b) shows the respective transfer function. For frequencies $\omega \gg \omega_c$, the measured voltage signal perfectly represents the electric potential at the sensor, *i.e.* the amplitudes of V_S and V_R are the same and no phase
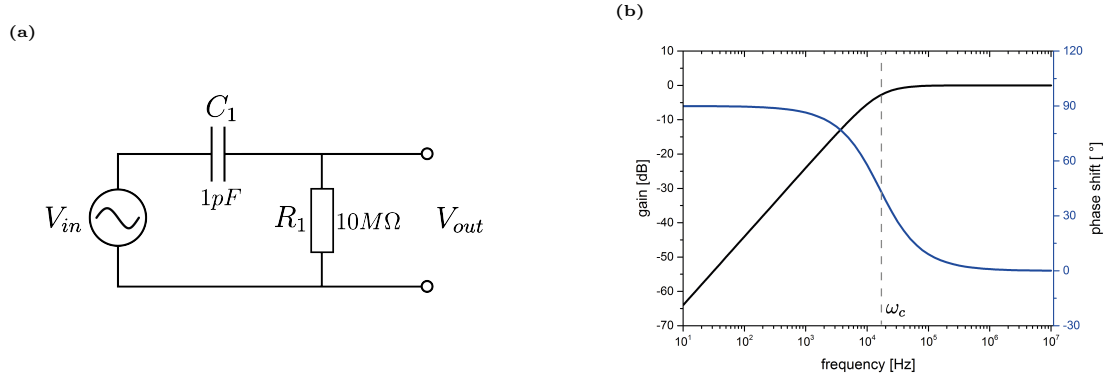
Figure 2.10: (a): A resistor attached to the sensor results in a first order high pass. (b): Amplitude gain and phase shift over frequency for RC circuit.

shift occurs. For frequencies $\omega \ll \omega_c$, the transmitted signal amplitude is attenuated and a phase shift of 90 degrees occurs, *i.e.* $|\partial_t \mathbf{E}|$ is measured instead of $|\mathbf{E}|$. Therefore, for the measured signal to be as true to the sensor voltage as possible for a wide range of frequencies, a load with a high enough resistance value has to be chosen. However, for practical applications, the attached load consists of more than a single resistor, as the sensor signal is usually fed into a preamplifier system attached with a shielded cable. Depending on input impedance and capacitance of the preamplifier circuit, the cutoff frequency may differ distinctly from $1/RC$. In most cases, especially for weak sources, amplification of the sensor voltage signal is necessary. For this purpose, numerous configurations exist [93]. Preferred modes of operation for such acquisition circuits are impedance matching and amplification of the voltage signal.
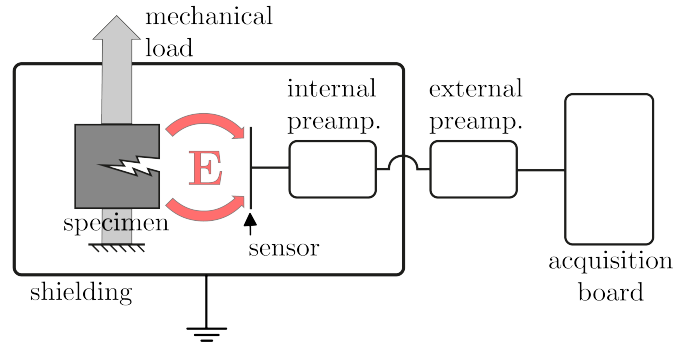

Figure 2.11: Schematic of measurement setup, consisting of source (fracturing specimen), sensor, internal and external preamplifier and acquisition board.

A schematic of the basic setup for the measurement of weak, fracture-induced electric fields (as used for most of the experiments presented in this work) is shown schematically in figure 2.11. A first "internal" preamplifier is directly connected to the sensor, *i.e.* is also located inside the shielding enclosure. This concept was

previously presented for an integrated acoustic emission sensor by Shiwa *et al.* [94], and is now adopted for the purpose of EME measurements. Amplifying the electric signal directly at the sensor reduces the influence of a long cable connection, *e.g.* the noise corruption between sensor and amplifier and the signal loss due to capacitive loading. The signal is then further amplified by a second, "external" preamplifier before being recorded by an acquisition board.
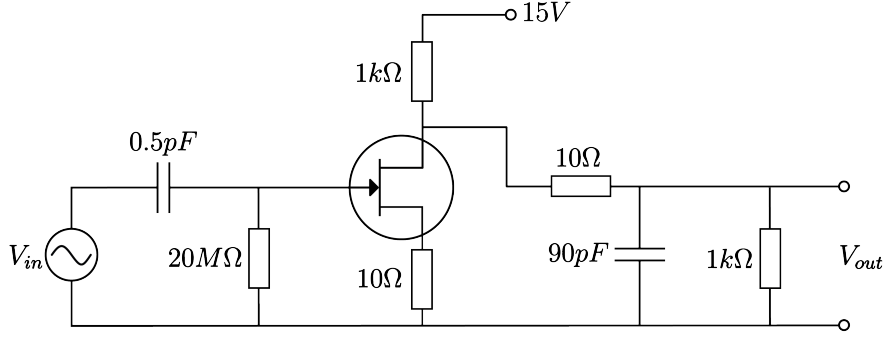

Figure 2.12: Circuit of first amplifier stage used for SPICE simulations.

Figure 2.12 shows the circuit diagram of the sensor and the first preamplifier stage. This stage consists of a junction field effect transistor (JFET) in a common source setup. For the calculation (using LTspice) of the transfer function, a BNC cable and the $1\,\mathrm{k\Omega}$ input resistance of the acquisition board are also included. Figure 2.13 (a) shows the calculated amplitude response and phase shift depending on the frequency of the sensor voltage. For frequencies between 200 Hz and 2 MHz, the amplitude response is almost flat and the signals are inverted (phase shifted by 180 degrees).

A direct result of this bandpass character is shown in figure 2.13 (b). The bandpass corresponds to specific time constants in the time domain. The step response, *i.e.* the response of a system to an instantaneous rise in input voltage is characterised by two time constants $\tau_{1,2}$. These time constants define the upper and lower limits of measurable changes in input voltage. Figure 2.13 (b) shows the calculated (LTspice) response of a system consisting of a capacitive sensor and a JFET amplifier (first, "internal" amplification stage) with an attached BNC cable to a step function as input voltage.
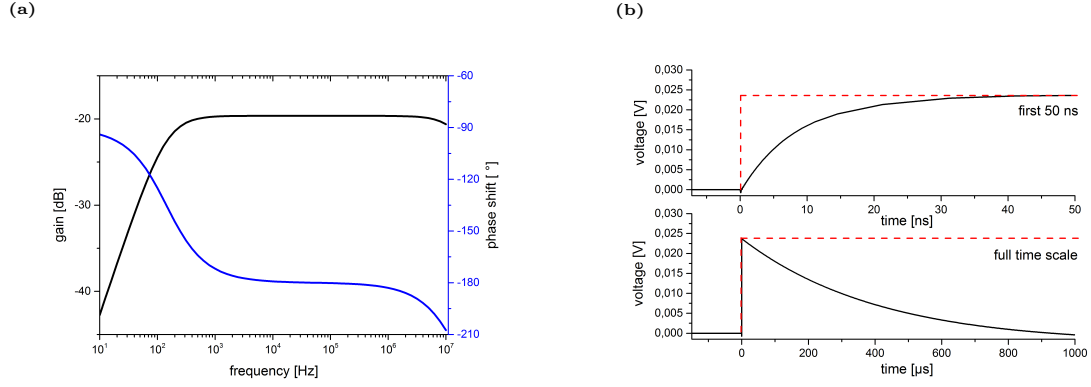
Figure 2.13: (a): Numerical result for the transfer function of the first amplifier stage. (b): Response of circuit to step function as input voltage, plotted for two different time scales. Dotted line: Input voltage, normalised to output amplitude.

These numerical results show the theoretical limits in frequency range and time scales for which a sensor signal will be recorded without being significantly altered.
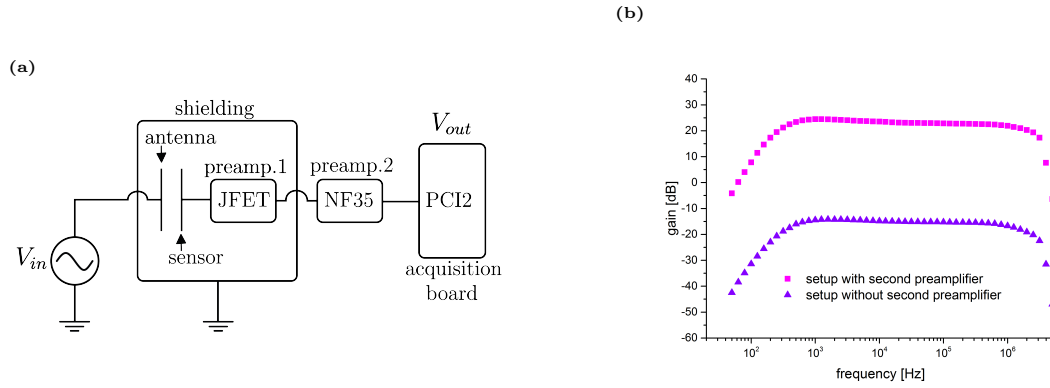

Figure 2.14: (a) Schematic of setup for measuring transfer functions. (b) Measured transfer functions for different variations of applied measurement chain.

The actual setups used to measure and record EME signals may include additional components. Figure 2.14 (a) shows a setup to experimentally determine the amplitude of the transfer function of the measurement chain used for most of the experiments presented in this text. An antenna (a 30 mm long wire with a diameter of 0.6 mm) fed by an arbitrary waveform generator serves as tunable voltage source. The sensor (a wire with the same geometry as the antenna) is directly connected to a JFET amplifier (n-channel JFET 2SK932-22, common source circuit, with a 20 MΩ input resistor). The signal then is further amplified by a commercially available low-frequency amplifier (UBBV-NF35, Aaronia AG) and recorded by a PCI-2 acquisition card (Mistras corporation, software: AEwin). The measured amplitude of the voltage signals as a function of frequency is shown in figure 2.14 (b) for the whole measurement chain and for a setup without the second preamplifier. For both

25

cases, the bandpass characteristic mainly reflects the 1 kHz high-pass filter respectively the 3 MHz low-pass filter of the acquisition card. Between 1 kHz and 3 MHz the transfer function of the sensor circuit system is almost constant.

In addition to the upper frequency limit of the setup, the capability of measuring fast changes in voltage is further limited by the maximum sample rate of 40 MHz of the used acquisition card.

Considering electric fields generated by crack propagation and crack wall vibrations (as discussed in section 2.1), the proposed setup is well suited to detect the electric field component linked to the oscillations of charged crack walls as well as the electric field component attributed to charge separation during macroscopic crack propagation.

2.4.3 Shielding

In a real experiment, the electric fields generated during fracture can be exceeded by the electric noise floor. Therefore, measures to reduce this electric noise have to be considered. A conducting enclosure can reduce electric fields by several orders of magnitude. This ability is characterised by its electric shielding effectiveness. The shielding effectiveness of an enclosure depends on the frequency of the electric field as well as on the enclosure's characteristics and design. The latter comprise the enclosure's material parameters, such as conductivity and permeability, as well as its form and dimension and the existence of apertures and seams. The shielding effectiveness of metallic cavities with apertures is well studied [95, 96, 97]. For shielding low frequency electric fields, a grounded metallic enclosure, *i.e.* a Faraday cage, proves sufficient. However, in order to perform EME measurements of material fracture inside the chamber, several modifications to a perfect Faraday cage are required. Figure 2.15 (a) shows a schematic of a shielding enclosure for a typical setup. Here, apertures are almost always necessary as feedthroughs for fixtures, cables and mechanical connections to the testing machine. Figure 2.15 (b) shows the spectrum of the background noise in our laboratory measured with our sensor and acquisition circuit (red line). After enclosing the sensor and preamplifier in a grounded metallic box, the noise floor is reduced by up to 60 dB to the level of the electric noise of the measurement (blue line). Most of the remaining noise floor is attributed to our measurement equipment. To quantify the equipment's influence on the measured noise, its equivalent input noise density for the whole bandwidth of the equipment (1 kHz-3 MHz) was calculated to be n = 3.84 nV$\sqrt{\text{Hz}}$.

The enclosure is made from aluminium with a height $a = 320$ mm, a width $b = 320$ mm and a depth $d = 120$ mm. The wall thickness is 5 mm. The relatively thick walls are a result of practical considerations regarding mechanical stability, since for shielding purposes a much thinner wall would be sufficient. The dimensions are small enough to not have to consider resonance effects. Resonance frequencies for any TE$_{mnp}$ modes in a rectangular cavity filled with a medium are

$$f_{mnp} = \frac{c}{2\pi\sqrt{\mu_r \varepsilon_r}} \sqrt{\left(\frac{m\pi}{a}\right)^2 + \left(\frac{n\pi}{b}\right)^2 + \left(\frac{p\pi}{d}\right)^2} \tag{2.40}$$

with the relative permeability μ_r and relative permittivity ε_r of the medium. For the enclosure dimensions, air as the cavity filling medium and the first cavity mode TE_{101}, the first resonance frequency f_{101} is expected at 663 MHz, which is far beyond the frequency range considered in this context.
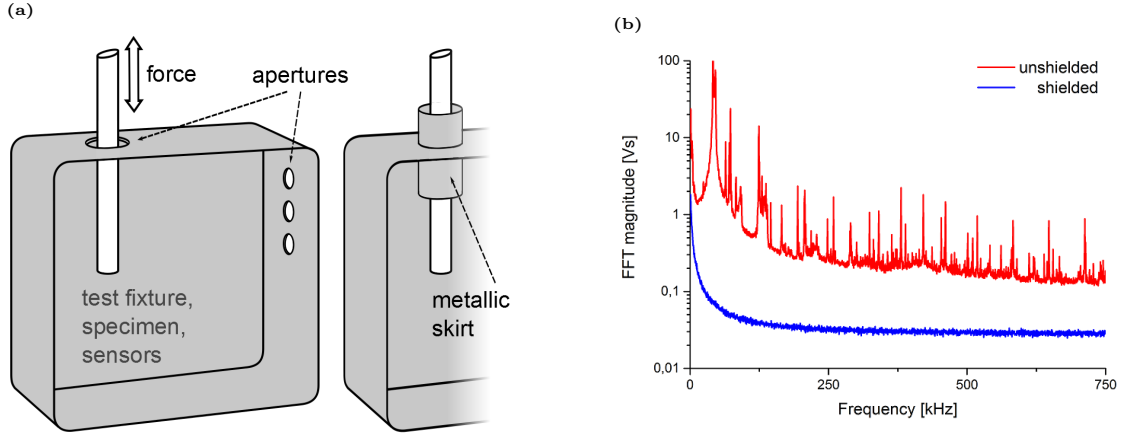

Figure 2.15: (a): Left: Schematic of shielding enclosure with apertures and mechanical connection to the testing machine. The front is closed during measurements. Right: Proposed addition of skirt to increase waveguide length. (b): Noise floors measured with and without shielding.

Figure 2.16 (a) shows the influence of apertures in the shielding box. The noise floor was measured before the addition of the apertures. Then one aperture as required for the force transmission (25 mm diameter) and three apertures for cable connectors/feedthroughs (15 mm diameter each) were added to the enclosure. As seen in figure 2.16 (a), these apertures do not compromise the shielding effectiveness. This is due to the fact that these apertures may be considered as waveguides operating below their cutoff frequency for the considered range of the EM field. The principles of electromagnetic waveguides are well-established and can be found in standard literature, *e.g.* [98]. The cutoff frequency $f_{cutoff,mn}$ for an electromagnetic wave in a circular waveguide depends on its mode and the radius a of the waveguide. For the transversal-electromagnetic modes TE_{mn}, the cutoff frequencies are

$$f_{cutoff,mn} = \frac{p_{mn}c}{2\pi a} \tag{2.41}$$

with c being the wave velocity and p_{mn} being the nth zeros of the derivative $J'_m(x)$ of the Bessel functions. For frequencies below f_{cut}, the electromagnetic field cannot propagate through the waveguide and is attenuated instead. In this case, the dominant mode would be the TE_{11} mode. So for the largest aperture used for the experiments presented in this text, with a diameter of 25 mm, the cutoff frequency is approximately 15 GHz. Reversely, the maximum frequency that is considered here is 3 MHz. So apertures with diameters below 120 m operate as waveguides below their cutoff frequency and will therefore not compromise the shielding efficiency of the shielding enclosure. The specific attenuation then depends on the frequency of the waves, the electric and magnetic properties of the waveguide and the medium within as well as the length l of the waveguide. In our case, l represents the wall thickness of the shielding enclosure, which is perfectly sufficient. On the other hand, the length of the waveguide can easily be increased by adding a metallic skirt to the aperture, as indicated in figure 2.15.
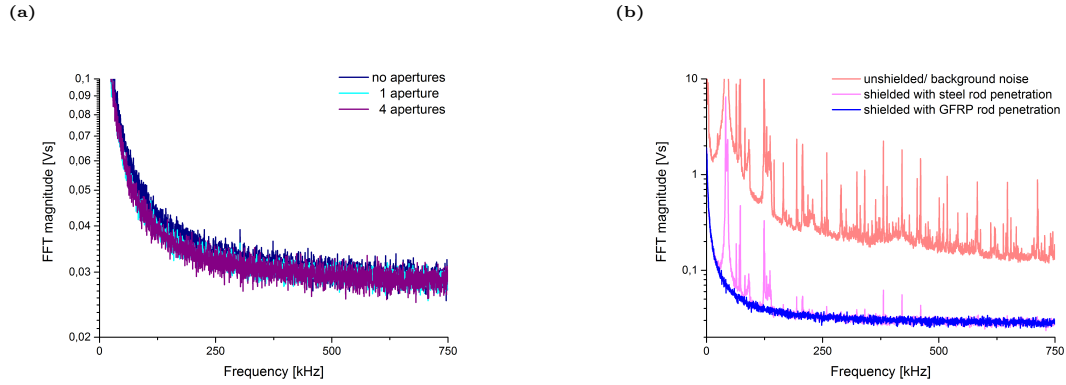

Figure 2.16: (a): Influence of apertures on noise floor. (b): Influence of shielding penetrations.

Electrically conductive connections of the test fixture with the testing machine can completely compromise the shielding effect, since they may guide external fields into the enclosure. A simple way to prevent this effect is to use connections made of non-conductive material. Figure 2.16 (b) shows the noise spectrum inside the enclosure for two rods of different material connecting the testing machine with the interior of the enclosure. Whilst a connection made of steel raises the noise floor significantly, a connection made of glass fibre reinforced plastic does not compromise the shielding effectiveness of this setup.

2.4.4 Influence of charged surfaces on measured signals

While the electric field generated by fracture processes may not be altered along its propagation path like the simultaneously generated acoustic waves, the EME signals measured at the sensor may very well be affected by the material properties and the dynamics of the surrounding materials. As analysed in section 2.4.1, conductors

in the vicinity of the EME source and EME sensor will influence the electric field distribution and therefore may also have a negative effect on the sensor's sensitivity. For this reason, the setups for most of the presented experiments in this work were manufactured from non-conductive materials (mostly PMMA and PVC). However, the use of this kind of dielectric materials is accompanied by other effects that have to be taken into consideration. Polymeric materials, amongst many others, tend to accumulate electric surface charges when brought into contact with other materials. This triboelectric effect is known since the times of ancient Greece, but the fundamental mechanism is still not fully understood, though it is assumed to be a combination of several different processes [99, 100].

Charges near the sensor are of no concern to the EME measurement as long as they change with time constants that are small compared to the lower cutoff frequency of the applied sensing circuit. Therefore, the relative movement of the specimens, the test fixtures and the sensor during mechanical loading or the slow charge relaxation in dielectric materials will not generate measurable voltage signals. Nevertheless, faster relative movement between statically charged surfaces and the sensor, which will occur during the fracture of a specimen, may very well generate measurable EME signals that might superimpose with the signals generated by the fracture process.

Figure 2.17 shows a simple experimental setup. This experiment was initially designed for a different purpose, as will be discussed at the end of this section, but is well suited to investigate the influence of fast movement of a charged surface relative to an EME sensor. The movement of the surface is induced by an acoustic wave that propagates within the material. A standard source for an acoustic signal similar to that of a natural AE source is a pencil lead break (Hsu-Nielson source [101]). This method of generating an acoustic wave was not applicable here, because the whole setup was encased with a shielding enclosure. Therefore, a ball impact was chosen as the AE source. The force-time characteristic of a ball impact is a short impulse of a few microseconds [30], which translates to a very broad frequency range. The frequencies of the surface displacement near the sensor then depend on the dominant wave modes within the specimen.

As schematically shown in figure 2.17, a PVC plate with dimensions of 140 mm × 25 mm × 5 mm is mounted on two PMMA supports at the centre of an aluminium shielding enclosure (as described in section 2.4.3). A steel ball of 3 mm diameter is dropped from a height of 150 mm above the PVC plate, with the point of impact at the centre of the plate. On one side of the plate, an acoustic sensor (KRNBB-PC point contact sensors) is mounted at the surface of the plate at a distance of 50 mm from the point of impact. The EME sensor, a silver-plated copper wire of 0.8 mm diameter and 14 mm length, is placed on the opposite side of the plate with the same distance to the point of impact. The EME sensor is mounted 3 mm above the surface of the PVC plate and is attached to a JFET preamplifier. A small PMMA plate with dimensions of 30 mm × 7 mm × 2 mm is placed directly beneath the EME sensor, leaving a gap of 1 mm between plate and sensor. The PMMA plate can be tribo-charged by rubbing the plate with a paper towel, leaving, according to
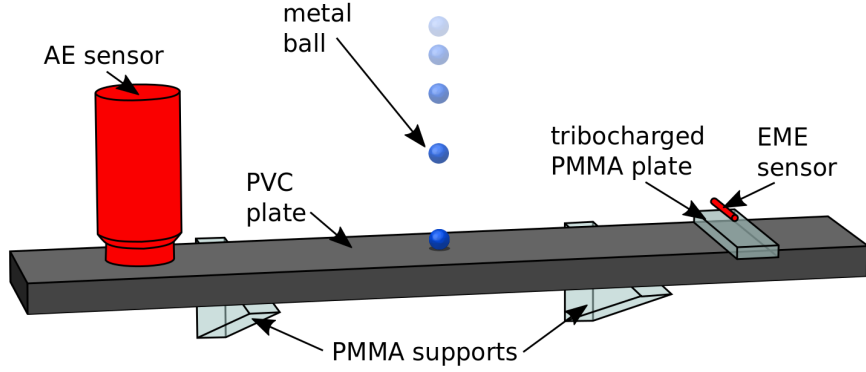
Figure 2.17: Schematic of test setup for ball drop tests.

the triboelectric table, a negative net charge on the surface of the plate. The impact of the steel ball generates an acoustic wave at the centre of the PVC plate. The wave than arrives approximately at the same time at both sensors. On one side of the plate, the surface displacement is measured by the piezoelectric AE sensor. The AE signal is amplified by 20 dB. On the other side of the plate, the acoustic wave leads to small variations in the distance between charged PMMA plated and EME sensor. The resulting EME signal is amplified by 27 dB.
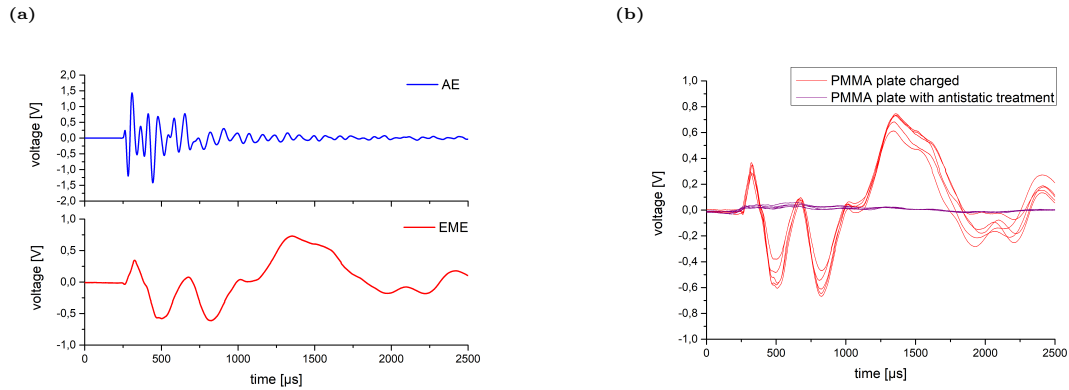

Figure 2.18: (a): Exemplary acoustic and electric signal recorded during a ball drop test. (b): Influence of electrostatic charge on EME signal strength.

Figure 2.18 (a) shows an exemplary pair of AE and EME signals for a ball drop test using a tribo-charged PMMA plate. The signal characteristics, especially the frequency contents, differ significantly, which is mainly a result of the different transfer functions of the AE and EME sensors.

Figure 2.18 (b) shows multiple EME signals measured for charged and for discharged PMMA plates. As one might expect, a clear increase in signal strength in the

presence of surface charges can be observed. However, even after antistatic treatment of the PMMA plates, the signal strength does not decrease to zero (or below the noise floor). This implies the presence of residual charges near the EME sensor.
These results illustrate the importance of taking (fast moving) surface charges into consideration during EME tests.

As mentioned at the beginning of this section, this test was originally designed for another reason. In section 2.3.2, a variety of source models for EME, proposed by different authors, were listed. These models result from EME measurements during fracture tests of many different kinds of materials, while also using different kinds of EME measurement equipment as well as multiple theoretical approaches. Some authors also attempted to test their models by trying to build test sources that replicate certain aspects of their model [102].
A similar approach is presented here. This simple experiment was conducted to investigate if an electrically charged surface generates a measurable EME signal when its surface displacement (*i.e.* relative distance to the sensor) resembles that of a fracture surface during and shortly after the fracture process or ,as in this case, the charge movement is induced by an acoustic wave that resembles one generated by fracture. The results as shown in figure 2.18 (a) clearly support this hypothesis. Therefore, if charges are generated during the fracture of a material and these charges move relative to the EME sensor, a measurable EME signal can be expected. Or, the other way around, if EME signals are measured that resemble the ones presented here, the assumption that they are generated by moving surface charges may be reasonable.

3 EME of polymers

In this chapter, experiments that have been performed to measure the electromagnetic emission occurring during the fracture of polymers are presented. Polymers are one of the two main components of CFRP. The investigation of EME on pure polymers is therefore the first step in the investigation of EME in CFRP.

Section 3.1 presents flexure tests that have been performed to study the EME signals generated by the fracture of epoxy resin samples. These experiments were the first to be performed in the context of the presented work. The aim of the experiments was not only to measure and study the EME generated by the fracture of epoxy resin, but also to study EME and its measurement in general. The experimental setup is based on a three-point flexure test and was designed to generate small and plane crack surfaces with a fixed orientation. This allowed the measurement of EME signals at different distances from the source and in different orientations between source and sensor. One result of these experiments was the development of the EME measurement setup presented in section 2.4.2, which was then used for all subsequent experiments. This means that the results presented in section 3.1 are the only results in this text that were obtained with a different EME test setup.

Section 3.2 contains tensile tests with different types of polymers that were performed to investigate the characteristics of EME depending on the fracturing material. A Tapered Double Cantilever Beam (TDCB) setup was chosen, with some modifications to the specimen geometry. EME generated by the fracture of four different polymers were measured with this setup, and their characteristics are compared.

The results presented here have already been published [1, 2]. The content of this chapter is consistent with these publications and places the findings in the overall context of the project.

3.1 Fracture of epoxy resin specimens

3.1.1 Specimen preparation

Identical specimens, with a geometry as shown in figure 3.1 (a), were manufactured using the mono-component epoxy resin system HexFlow RTM6. Partially cured RTM6 epoxy resin plates of 5 mm thickness were prepared. For this purpose, casting moulds made from two-component silicon rubber (Elastosil M 4601 A/B) were filled with the viscous resin and then heated for the curing process. For 80% cross-linked

resin plates, the process consisted of curing for 30 min at 120 °C followed by a post-cure for 140 min at 135 °C, with heating and cooling rates of 2 K/min [103]. The degree of cross-linking was determined by using differential scanning calorimetry (DSC) [103]. Then, the plates were cut to beams with lengths of 25 mm and widths of 5 mm. Notches of 3 mm length and 1 mm width were added, leaving a thickness of 2 mm at the centre of the specimens.

This specimen geometry resulted in fracture surfaces that are almost completely vertical and straight, with a variance of the angle between the fracture surface normal and the x-axis of less than 5°. This distinct orientation of the EME source is vital for the investigation of the relation between measured EME signal strengths and the relative position of the EME sensor.
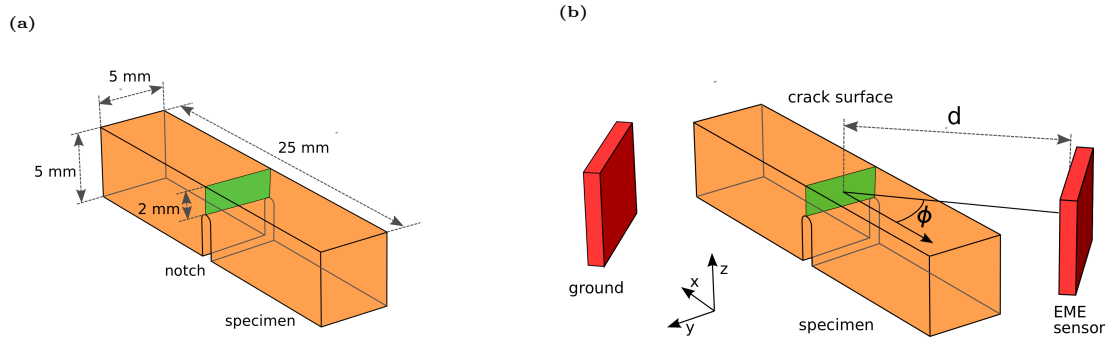

Figure 3.1: (a): Resin flexure test specimen geometry and dimensions, (b): Schematic of EME sensor orientation and distance. The area shown in green represents the crack surface.

3.1.2 Experimental setup

An experimental setup was designed to perform three-point flexure tests on single-edge notched flexure specimens. Figure 3.2 schematically shows the setup. The bend fixture has a support span of 20 mm and a pin radius of 1.5 mm. While the EME sensors have a fixed orientation, the test fixture, along with the specimen, is rotatable around the z axis. This allows different angles Φ between source and EME sensors, as is schematically shown in figure 3.1 (b).

The whole fixture was created from non-conductive materials. The load pins were made of polyvinyl chloride (PVC), and the rest of the fixture was made of poly-methyl methacrylate (PMMA). Therefore, the fixture exhibits a high compliance with regard to the specimens. This compliance of the fixture alone was measured to be 1.03 μm/N, which is 17.5% of the total compliance during the flexure tests.

A universal testing machine (Zwick ZT 5.0) was used to apply a mechanical load with a constant velocity of 5 mm/min. The load was measured with a 5 kN Xforce HP load cell.
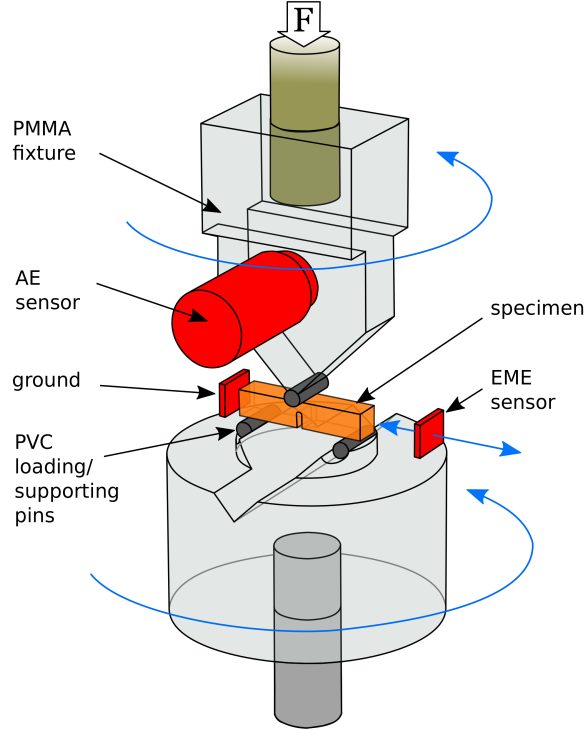
Figure 3.2: Schematic of three-point flexure test setup used for inducing fracture in epoxy resin specimens. Blue arrows indicate moveable parts designed to change the orientation and distance between EME source and EME sensor.

For the detection of the acoustic signals, a KRNBB-PC point contact sensor with a mostly flat frequency response was attached to the fixture above the loading pin (see figure 3.2). The AE signal was preamplified using a type 2/4/6 preamplifier (Physical Acoustics) without internal bandpass filter. A trigger-based acquisition was used. The signals were recorded using a PCI-2 system (Physical Acoustics) with a 1 kHz-3 MHz bandpass filter (1 kHz 4th order Butterworth high-pass and 3 MHz 6th order Butterworth low pass, with rectangular window function). The AE acquisition parameters are listed in table 3.1. (For the thresholds, the term dB_{AE} denotes an amplification with respect to 1 μV and will also be used for the EME detection throughout this text.)

The electromagnetic signals were detected with an EME sensor setup consisting of two small copper plates of 6 mm height and 8 mm width, forming a capacitor. While one of the plates was grounded, the other one was connected to a 2/4/6 preamplifier without internal bandpass filter. The signals were also acquired with the PCI-2 system. The EME acquisition parameters are listed in table 3.1. As mentioned in section 2.4.2, the EME acquisition setup used for the flexure tests differs from the ones used for all other experiments presented in this text. The flexure tests were the first experiments conducted in the context of this work, and no special EME measurement equipment was available at this point. For this reason, the same

Table 3.1: Acquisition parameters used for AE and EME signal recording during flexure tests.

Channel	Threshold [dB$_{AE}$]	Preampl. [dB]	Sample rate [MS/s]	PDT [µs]	HDT [µs]	HLT [µs]
AE	35	20	10	10	80	300
EME	35	40	10	50	1000	1000

preamplifier as was used for the AE measurement was used for the EME measurement. These 2/4/6 preamplifiers were specifically designed for the acquisition of acoustic signals. The measured transfer function of the measurement chain consisting of sensor, preamplifier and acquisition card is shown in figure 3.3. Even with the internal bandpass filter of the preamplifier removed, the transfer function only has a flat characteristic above 40 kHz with a steep gain drop below 5 kHz. The insights gained from these first experiments then led, amongst other things, to the development of the measurement setup presented in section 2.4.2.
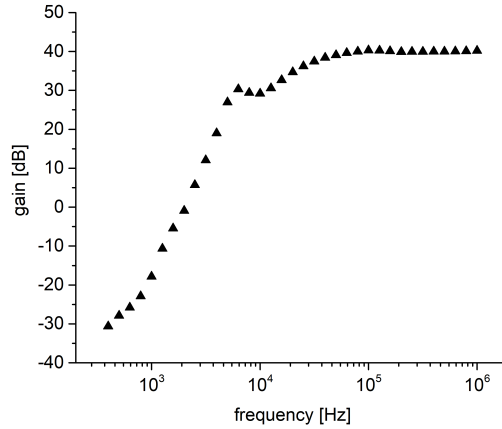

Figure 3.3: Measured transfer function of EME measurement chain used for the resin flexure tests.

The whole setup was shielded against electromagnetic noise and electrically insulated from the universal test machine using a grounded aluminium box of 3 mm wall thickness.

3.1.3 Results and discussion

When the applied load exceeds ultimate strength, complete fracture of the specimen occurs. The failure of each specimen results in one EME and one AE signal to interpret. These signals are composed of many separate, temporally and spatially

35

close signals that are emitted during crack propagation, merging into one EME and AE signal each. The crack dynamics are influenced by the stresses in different zones of the specimen. In flexure tests, there are generally two major zones, the tension zone and the compression zone. Therefore, the crack process consists of many separate steps with different characteristics. An image of the fracture surface after failure of one specimen is shown in figure 3.4.
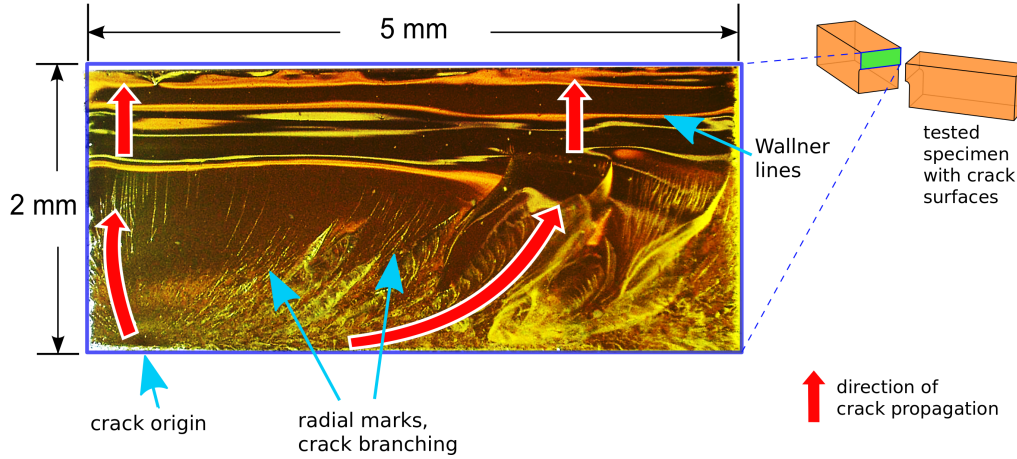

Figure 3.4: Microscopy image of the crack area of a RTM6 specimen with parameters of the crack dimension. The red arrows indicate the crack propagation starting at a point on the notch. Two different areas of crack propagation are visible, a rough area with almost radial marks starting at the point of crack origin and a smooth area with rib marks at the upper half of the crack surface.

In this example, the crack propagation starts at a point of high tension on the edge of the applied notch. Radial marks are visible which are parallel to the direction of crack propagation. Sliver-like patterns indicate the region where crack branching took place and indicate an accelerating, unstable crack propagation. The upper half (compression zone) is smooth with straight, horizontal rib marks (Wallner lines). This indicates smaller velocities and a propagation direction perpendicular to these lines. Since the crack surfaces are mostly smooth, the crack area can be approximated by its height and width. The resulting crack surfaces are mostly parallel to the y-z-plane, with a maximum deviation of 5°.

Analysis of EME signal characteristics

Figure 3.5 (a) shows signals measured by the electromagnetic and the acoustic emission sensor for one representative specimen.
The AE signal is influenced by the applied sensor as well as by the experimental setup. The acoustic emission sensor is attached to the fixture above the loading pin, since the specimens are too small to directly attach the sensor to the specimen surface. Along the propagation path from crack to sensor, the acoustic wave is influenced by damping and dispersion in the materials it propagates in and by

reflection at the boundaries of the geometry. Furthermore, the acoustic signals partially exceed the linear working range of the applied AE sensor, which leads to saturation effects in the recorded AE signals. This could only have been avoided by increasing the distance between AE sensor and source, which would have resulted in even more influences of the propagation path, or by a weaker source, *i.e.* a smaller crack area. The latter would also have resulted in a much weaker EME signal strength.

Figure 3.5 (b) shows the difference in arrival time for the exemplary EME and AE signals. The measured time difference is 3.5 µs. Assuming the EME signal to be detected instantaneously (within the measurable time resolution), a distance between source and AE sensor of about 25 mm and transversal wave velocities in PVC and PMMA in the order of 1000 m/s, the difference in arrival time is expected to be in the range of 25 µs. Since there is no indication of the travel times of the AE and EME signals being significantly different from the typical values, the reason for the discrepancy between expected and measured arrival time difference may either be an offset in the source mechanisms for both signals or a result of an inadequate measurement setup. The latter case seems more likely, considering the results presented in the next section (see figure 3.18 of section 3.2) which are recorded with the improved EME measurement setup and where a more reasonable time difference can be observed. Therefore, the EME signal might start earlier with lower frequencies that cannot be detected by the setup used for this experiment.
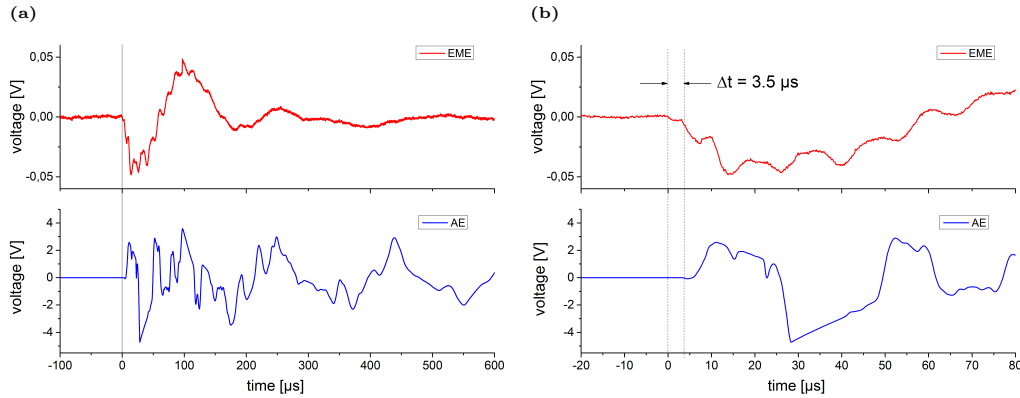

Figure 3.5: (a): Typical pair of electromagnetic and acoustic signals obtained from the crack of one specimen. (b): Same signals with different time scale to identify the arrival time difference Δt. (Also, the AE sensor saturation effects can be seen.)

Figure 3.6 (a) shows five exemplary EME waveforms recorded with the same settings, figure 3.6 (b) shows the respective FFT spectra, and 3.6 (c) shows the same spectra with a different magnitude scale and the averaged FFT spectrum of all five signals. (Here, five signals with comparable amplitude were chosen for better comparison. In general, as is presented and discussed in sections 3.1.3 and 3.1.3, the signals were measured with a much greater variance in amplitude.) The EME waveforms and their frequency spectra suggest that the signals consist of several components that
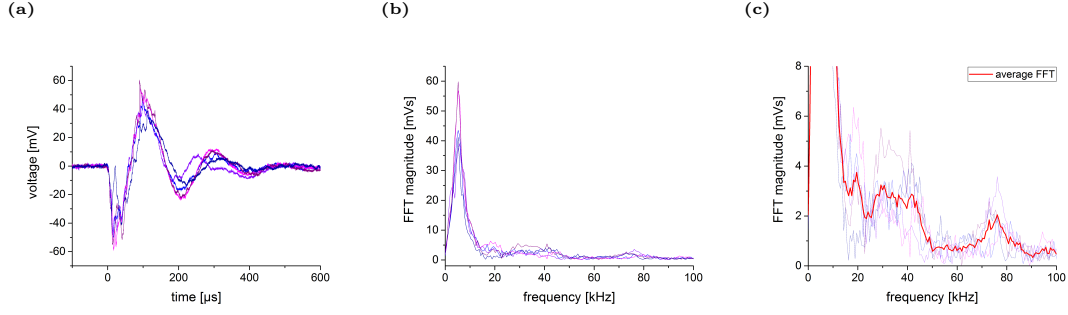
Figure 3.6: (a): Five representative EME signals recorded with the same settings. (b): FFTs of the EME signals. (c): FFTs of the five exemplary EME signals with different magnitude scale and averaged FFT.

superimpose. The dominant part is a low frequency oscillation in the frequency range from 1 kHz to 20 kHz. Oscillations with higher frequencies and smaller amplitudes are superimposed. The averaged spectrum indicates that the high frequency part of the signals mainly consist of two distinct frequency ranges, one from 20 kHz to 50 kHz and a smaller peak with a centre frequency of 76 kHz.

As is briefly discussed in the theory section (see section 2.3.2), the different EME signal components may be the result of different source mechanisms. Theoretical considerations as well as results presented in literature suggest three main mechanisms: charge separation during crack formation, charge relaxation and vibrations of charged crack surfaces.

For further understanding and to improve the understanding of the EME acquisition system, tests using an artificial test sourc powered by an arbitrary waveform generator were conducted. The basic hypothesis to follow within the first series of tests was that one part of the signal stems from the separation of charges during crack growth and the second part is due to the subsequent charge relaxation. The combination of these two contributions will be referred to as base signal in the following. As a third part of the signal, a small oscillation is superimposed. This oscillation is assumed to originate from the vibrations of the charged crack surfaces.

For the charge separation following the crack tip, the generated electric field emitted would rise during crack growth due to cumulative charge separation and then decline with a certain time constant. A corresponding theoretical model for the temporal characteristic of the electric field caused by cracking rocks was reported by Ivanov *et al.* in [72].

A given charge distribution decays over time due to conduction currents. The charge relaxation time τ for a surface charge at the crack surface of a RTM6 specimen depends on the dielectric properties of RTM6 and the adjacent air. For RTM6, $\sigma = 6.67 \cdot 10^{-10}$ Ω^{-1}cm^{-1} and $\varepsilon_r = 4.13$ were measured. The charge relaxation time τ also depends on the geometry of the charged surface and the surrounding matter. Furthermore, the dielectric properties are a function of the temperature, which is much higher at the crack tip than in the surrounding bulk. Therefore, τ

is time and location-dependent during the crack propagation process, but constant afterwards. For an infinite, uniformly charged plane separating two half spaces of different materials, the surface charge relaxation time is calculated by $1/\tau = 1/2\left(1/\tau_1 + 1/\tau_2\right)$ with $\tau_i = \varepsilon_i/\sigma_i$. In this case, the relaxation time for a surface charge between RTM6 and air is calculated to be $\tau \approx 110$ ms. This estimation only gives the order of magnitude for the actual time constant, because the real crack surfaces are not infinite planes. Since the fracture process is much faster than the relaxation of charges, the influence of the surface temperature is not considered in this estimation.

To evaluate the system response to source signals with different relaxation times, different signals, as seen in figure 3.7 top, were generated with the waveform generator. These test signals resemble a smoothed step function. All test signals exhibit the same rise characteristic, but diminish with different time constants, with a smooth transition between these two parts. The signals were generated with a total length of 2 ms. The first signal does not decay ($\tau = \infty$). The other signals decay with $\tau \approx 600$ µs and $\tau \approx 200$ µs, respectively. Regarding the estimated charge relaxation time of RTM6, the first signal is considered to represent the experimental conditions.
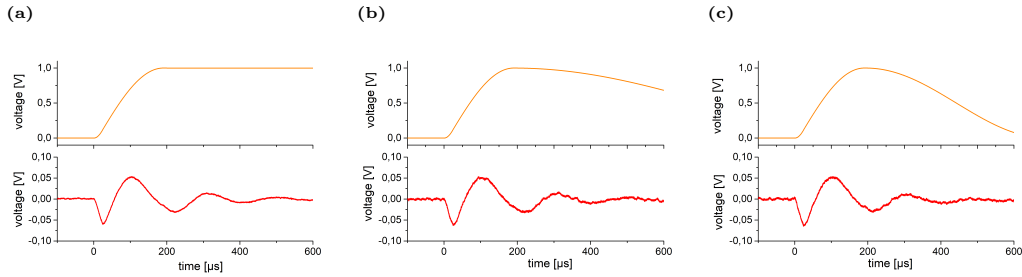

Figure 3.7: (Top): Test signals fed to the test source by the arbitrary waveform generator, each having the same rise characteristic but different decay rates ((a): $\tau = \infty$,(b): $\tau = 600$ µs, (c): $\tau = 200$ µs). (Bottom): The resulting signals measured with the present sensor system. Their shape is dominated by the rise characteristic of the test signals.

The according signals detected with the EME sensor are shown in figure 3.7 (bottom). Only a fraction of such slowly varying fields were able to pass the bandpass filter of the acquisition card (1 kHz high pass, 4th order Butterworth). Furthermore, the present acquisition electronics also have a frequency-dependent transmission characteristic, as shown in figure 3.3. The resulting signals resemble slow oscillations containing frequencies below 20 kHz. This indicates that the dominant part of this oscillation is the response of the sensor system to the first rise in the test signal. This rise is continuous and increases over a time interval of approximately 20 µs. The signal is measured with reversed polarity. The further behaviour of the test signal has no significant impact on the measured signal, as long as the relaxation times are high enough. The measured signals are superimposed with a noticeable noise floor.

To test the response of the measurement chain to higher frequencies, an oscillation with a frequency of 80 kHz was used (figure 3.8, (a), (top)). This oscillation is sup-
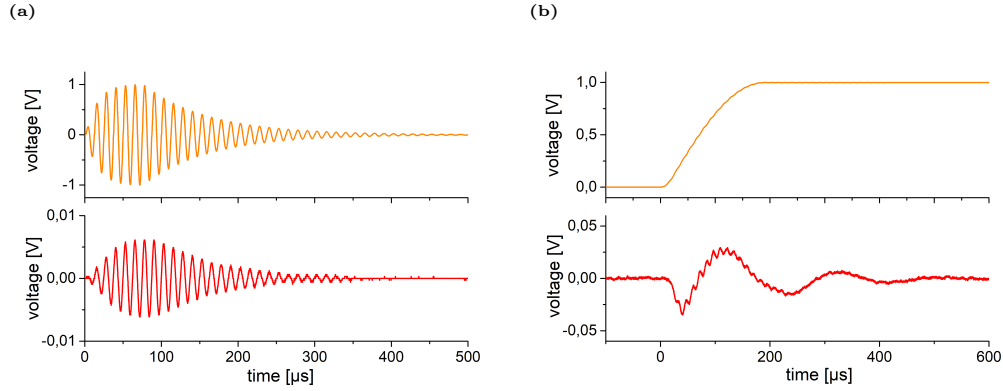
Figure 3.8: (a): Oscillating part of the test function, generated by the arbitrary waveform generator (top) and measured with the EME sensor system (bottom). (b): Complete test function with base part and added oscillation (top) and the corresponding measured signal (bottom).

posed to represent the signal that is generated by the vibration of the charged crack surfaces. Its rise and decay times would depend on the generation and relaxation of the charges and on the damping of the crack surface vibration. The envelope of this oscillation was chosen to increase within 100 µs and to subsequently decay to zero with a time constant of 100 µs. Figure 3.8 (a), (bottom) shows the response of the sensor system to the oscillation part only. For this part, the rise and decay times and the frequency of the oscillation are measured unaltered. The polarities of the generated and the measured signals are reversed.

Combining base signal and oscillation part results in the test signal that is shown in figure 3.8 (b), (top). A ratio of 1/200 for the maximum amplitudes of the two parts was chosen, which makes the oscillating part in the generated signal barely noticeable in the figure. The measured voltage signal of the complete test signal is shown in figure 3.8 (b), (bottom). The measured signal clearly shows the system response due to the rise in the base signal superimposed by the contributions of the 80 kHz oscillations.

The results of the experiments with the test source and the measured transfer function (figure 3.3) clearly indicate that the present measurement chain cannot detect frequencies below 1 kHz and that faster oscillations superimposed with the slower field change are detected almost unchanged. Furthermore, the measured base signal, attributed to the charge separation during crack propagation, is only partially detected and is strongly influenced by the applied acquisition setup. As a result of these first tests, a new EME measurement setup was developed, which is presented in section 2.4.2 and which was then used for all following experiments.

Since it is assumed that the high frequency oscillations are generated by the vibrations of the charged crack surfaces, one might expect some correlation between these parts of the EME signals and the corresponding AE signals.

Figure 3.9 (a) shows the same exemplary EME and AE signals as are shown in figure
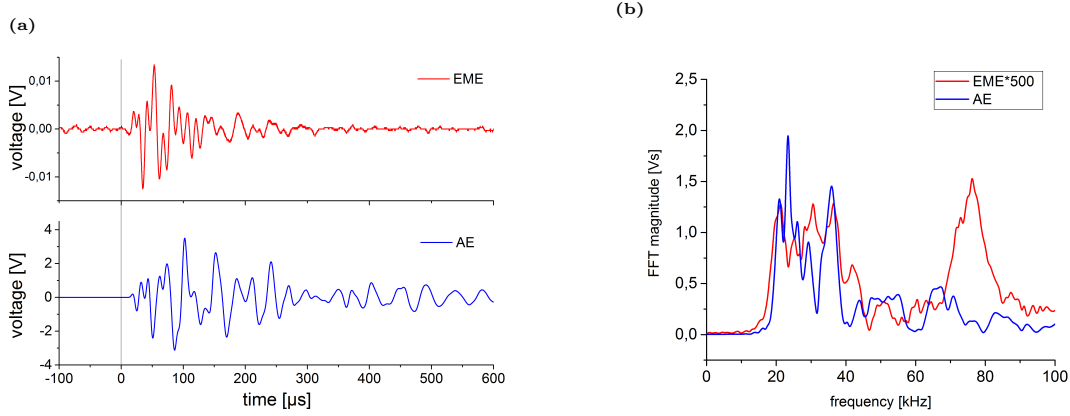
Figure 3.9: (a): Exemplary EME and AE waveforms (as shown in figure 3.5) with additional 20 kHz high-pass filter applied, (b): FFT spectra of filtered exemplary EME and AE signals. EME signal scaled for better comparison.

3.5, but with an additional 20 kHz - 100 kHz bandpass filter applied to remove the base part of the EME signal. The same filter applied to the AE signals partially removes spurious signals and effects from AE sensor saturation.

When comparing the filtered EME signals and the AE signals, one has to take into account that the AE frequencies are influenced by the geometry of the specimen and the propagation path from the source to the acoustic sensor [51, 68]. The frequency response of the AE sensor also has to be considered. The filtered EME and AE signals still differ in terms of frequency content, rise and decay time. Figure 3.9 (b) shows the frequency contents of both (filtered) signals. Although both signals contain frequencies in the range below 50 kHz, the peak at 76 kHz is not present in the AE spectrum. Nevertheless, since the frequency ranges of both signals largely correspond for frequencies below 60 kHz, the assumption that the higher frequency part of the EME signal originates from vibrations of charged crack surfaces is considered reasonable.

Influence of detection angle

To characterise the present sensor system as well as the emitted field during crack initiation and propagation, several flexure tests were performed, with the distance d between the centre of the specimen and the EME sensor and the angle ϕ between the crack surface normal and the sensor plate normal as varied parameters (see figure 3.1). To ensure statistical significance 6 to 8 specimens were tested for every point of measurement. The signals were individually analysed by calculating the absolute energy using equation 3.1. Here, Z_M=10kΩ is the input impedance of the applied measurement equipment.

41

$$W = \frac{1}{Z_M} \int\limits_{t_0}^{t_W} (U(t))^2 \, dt \tag{3.1}$$

The resulting energies for each distance and angle were averaged to yield one data point. Although the specimens were prepared to be identical and were carefully placed and adjusted on the fixture, the EME and AE signals show a wide distribution in signal strength. This results in a high standard deviation of the calculated data, which is of the same order of magnitude for the EME and the AE signals. Thus, the cause for this high deviation is attributed to the complexity of the fracture process and not to the signal detection.

While the sensor orientation was kept constant, the bend fixture was rotated orthonormal to the z direction. That way, it was possible to systematically change the angle between the crack surface normal and the sensor plate normal. To investigate the influence of this angle on the EME signal strength, the angle was varied between 0° (parallel) to 90° (perpendicular) in steps of 10°. The distance d of the sensor (see figure 3.1) was kept constant at 14 mm. For the recorded EME signals, the absolute energies were quantified. Additionally, a bandpass filter of 20 kHz - 100 kHz was applied to the signals. Thus, the base part and most of the underlying noise were removed, leaving only the oscillating part of the waves. For the filtered signals, the energies were quantified as well. The results are shown in figure 3.10.
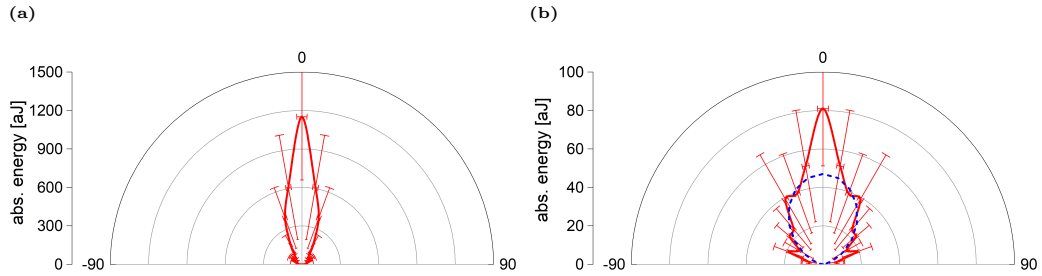

Figure 3.10: Averaged signal properties depending on detection angle. The data is mirrored at the 0° axis for clearness. (a): Angular dependence of the absolute energy of the whole signal. (b): Angular dependence of the absolute energy of the oscillating part of the signals and a scaled $\cos^2(\phi)$ graph (dashed).

A clear correlation between signal energy and detection angle is observable for both parts of the signals. While the strongest signals are detected for a parallel orientation of crack surface and sensor plate, the measured signals decrease significantly in energy with increasing angle. This indicates a directional field distribution.

The angular directivity differs for the different parts of the signals. Figure 3.10 (a) shows the calculated energies for the detected signals consisting of the base part and the oscillating part. The signals' energy is dominated by the energy of the base part. The base signal is attributed to the separation of charges during crack growth.

This part exhibits some kind of dipole characteristic, since two crack surfaces with opposite charges form a dipole moment with a direction parallel to the crack surface normal. The detected energies show a stronger angular dependence than the energies of the oscillating part. Only for angles up to 40°, energies significantly exceeding the level of the noise were detected with a maximum at 0°. At $\phi=10°$, the energy of the signals dropped to 53% when compared to the energy at $\phi=0°$.

The oscillating part of the signals is assumed to be generated by the vibration of the crack surface. When this vibration is assumed to be perpendicular to the crack surface, *i.e.* has a strong directional orientation, an corresponding angular dependence of the detected signals is expected. The observed behaviour seems to be more complex than one would expect for a simple dipole characteristic. For a point dipole, the electric potential scales with $\cos(\phi)$, so one could expect the detected energy to scale with $\cos^2(\phi)$ (as indicated in figure 3.10 (b)). The angle-dependent energy of the detected signals only partially follows this pattern. However, since the sensor is not point-like even for $\phi=90°$, the sensor is likely to detect some field components of other angles. This could account for the detection of higher energies for small angles than one would expect for a dipole characteristic.

Influence of sensor distance

One advantage of the small dimensions of the specimens is the ability to position the EME sensor close to the crack for every orientation under observation. When the distance between the source of the electric field and a detector is increased, a decrease in measured signal strength is expected due to geometric spreading. Additionally, the spatial characteristics of an electric field depend on the type of source and on the surrounding matter. To measure the distance sensitivity of the sensor system or rather the range of the EME signals, measurements of the EME signals for different distances between sensor and source were performed. The signals were detected for three different angles ϕ. For angles of 0°, 45° and 90°, the distance of the sensing plate was varied ranging from the closest distance possible, up to the distance where the signal-to-noise ratio inhibits detection of the signal. The recorded signals and the filtered signals (20 kHz - 100 kHz bandpass filter) were then analysed in terms of the detected energy. In figure 3.11, the results for the calculated energies are displayed for the complete signals (a) and for the oscillating part of the signals (b). As expected, the measured energy decreases with increasing source-sensor distance. This was observed for all three angles. As discussed in the previous section, the different parts of the signals show a different angular dependence. The dependence on the distance appears to be almost the same for the base signal and the oscillating part. Both parts of the signals are only detectable within a distance of a few millimetres. The characteristics of the plotted data show no intuitive dependence of distance d. This may be due to multiple influences, which all depend on the position of the sensor. The main effect is expected to arise from the spatial characteristic of the electric field. The potential generated by a dipole decreases with a $1/d^2$ dependence. This would result in a decrease with $1/d^4$ for the measured energies.
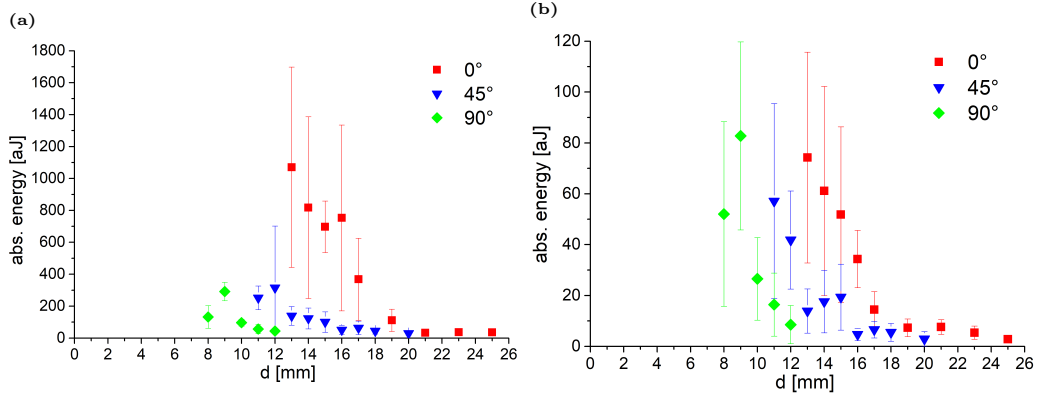
Figure 3.11: (a): Dependence of the absolute energy of the complete signal on the source-sensor distance. (b): Absolute energy of the oscillating part of the signals.

Such dependence on distance was not observed. Since the real charge distribution is unclear, multipole moments of different order may also appear during the fracture process, exhibiting different kinds of distance dependencies. Furthermore, with an increase of d, the distance between the capacitor plates also increases, and thus the capacitance decreases. For a constant field strength, the smaller the capacitance gets the higher the resulting voltage between the plates. Another effect that might be of larger relevance than the increase of capacitance with distance is the influence of other conductive parts of the experimental setup. Although the fixture was built from non-conductive materials, some other elements inevitably consist of conductive materials. The most important one is the acoustic emission sensor, which is positioned 25 mm above the specimen. Since all conductors near the source influence the voltage on the sensor plate [91], this influence becomes more important at larger sensor distances.

3.2 Mode I fracture of polymers

3.2.1 Material properties

Following the results from the previous section, and since polymers are one of the components of CFRP, the electromagnetic emission generated by fracture of different polymer types were measured. For this purpose four different polymer types, exhibiting different mechanical and dielectric properties, were chosen. The selection comprises the thermoplastic polymers polytetrafluorethylene (PTFE), polyether ether ketone (PEEK) and polypropylene (PP) as well as a thermoset polymer of cured RTM6 (which was also used for the experiments presented in section 3.1). In order to find correlations between the polymer properties and the generated EME, the mechanical and dielectric properties of the tested materials were determined first.

The mechanical properties of the thermoplastic polymers were measured according to DIN EN ISO 527-1 [104], using dog bone-shaped specimen in tensile loading (specimen shape and dimensions in accordance to DIN EN ISO 527-2 [105]). For the determination of the properties of the brittle RTM6 slightly modified dog bone-shaped specimens were used. An ARAMIS 12M digital image correlation system was used to measure the specimen deformation. Conditioning and testing was done at standard climate conditions (23°C and 50% relative humidity). The densities were obtained using a helium pycnometer. The acquired results, as summarised in table 3.2, are in accordance with those reported in literature.

Table 3.2: Material properties of tested polymers.

Material	Modulus [GPa]	Poisson's number	Yield str. [MPa]	Density [g/cm^3]
RTM6	2.74 ± 0.03	0.381 ± 0.006	26.2 ± 0.5	1.026 ± 0.001
PEEK	3.45 ± 0.01	0.374 ± 0.009	43.6 ± 0.5	1.301 ± 0.001
PTFE	0.72 ± 0.10	0.460 ± 0.029	4.0 ± 0.1	2.172 ± 0.003
PP	1.51 ± 0.03	0.420 ± 0.007	15.0 ± 0.3	0.919 ± 0.001

The electric properties of the materials were obtained from measurements using a frequency response Novocontrol Alpha analyser (frequency range: 1 Hz to 10 MHz), an Agilent 4980A auto-balance bridge (frequency range from 20 Hz to 2 MHz), and an Agilent E4991A impedance/material analyser (1 MHz to 3 GHz). Figure 3.12 shows the measured values for the relative permittivity and the electric conductivity of RTM6, PP and PEEK. No measurements were performed for PTFE, since the literature values reported already indicate the highly insulating properties of the material [106]. In the context of our work, the conductivity is therefore assumed to be negligible. Due to the intrinsic dependency of the electric properties on frequency, measurements were conducted spanning the frequency range of interest for

the experiments (100 Hz to 1 MHz). While the measured values for the relative permittivity shows no significant variations in this frequency range, the values for the electric conductivity vary over a range of up to four orders in magnitude. Still, these materials can be considered low conductive for all of these frequencies.
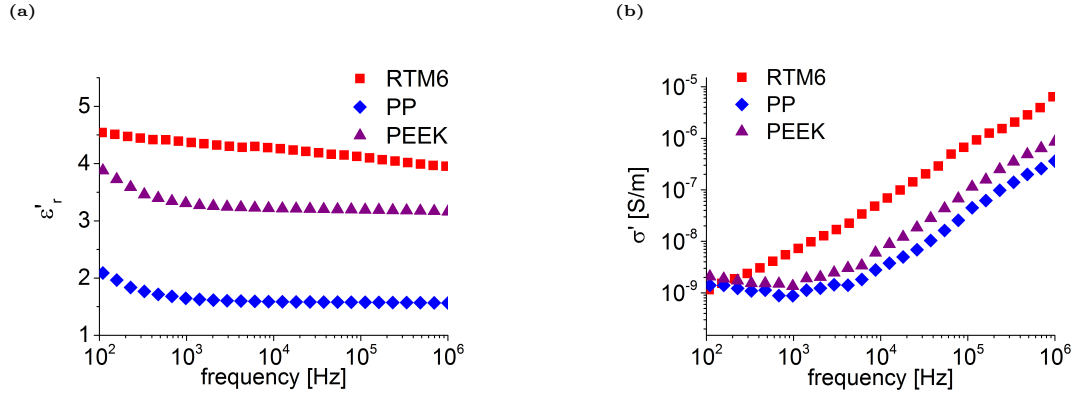
(a)

(b)

Figure 3.12: Dielectric properties of polymers as functions of frequency (a): Relative permittivity, (b): electric conductivity.

3.2.2 Specimen preparation

For the measurement of the electric fields generated by mode I fracture of different materials a tapered double cantilever beam (TDCB) setup was chosen. Figure 3.13 shows the geometry and the dimensions of the modified TDCB specimen. This specimen design allows for self-inhibiting crack growth for the more brittle materials used while preventing excessive plastic deformations at the pinholes for the more ductile materials investigated. This design also offers sufficient space for the attachment of sensors.

The RTM6 specimens were cured in correspondingly shaped casting moulds (a detailed description of the curing process is found in section 3.1.1), while the thermoplastic polymer specimens were cut from plates of 5.0-5.3 mm thickness. Pinholes, notches and side-grooves were added, the latter by using a flat end mill tilted by 45 degrees.
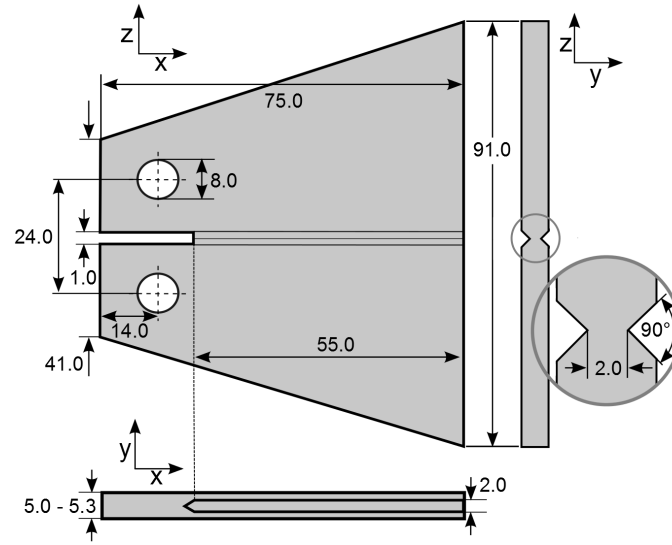
Figure 3.13: Geometry and dimensions of TDCB specimen used for mode I fracture tests of polymers.

3.2.3 Experimental setup

The test setup for the TDCB tests is schematically shown in figure 3.14. For most of the experimental setups presented in this text, the test fixtures are manufactured from non-conductive materials (mainly PMMA). For this experiment, pin grips and pins made from steel were used because of the higher forces that are needed to induce fracture to some of the tougher materials being tested. The mechanical load is introduced by a tube of pultruded glass-fibre-reinforced plastic.

The mechanical load is applied displacement-controlled by a universal testing machine (Zwick ZT 5.0). The load was measured with a 5 kN Xforce HP load cell. Different velocities for the displacement were chosen for different materials. This was necessary due to their different elasto-plastic behaviour. While the brittle RTM6 required a slower testing velocity of 1 mm/min to not initiate unstable crack propagation, the more ductile PP and PTFE required a higher testing velocity of 5 mm/min to initiate fracture in the first place instead of only showing plastic deformation at the notch and ductile failure of the material. For PEEK, fracture behaviour was the same for all of these velocities, so a testing velocity of 5 mm/min was applied.

For the detection of the AE signals, two KRNBB-PC point contact sensors were attached symmetrically to both, upper and lower, halves of the specimens, as is shown in figure 3.14. A trigger-based acquisition was applied for all channels. The acquisition parameters that proved adequate for the acquisition of the AE signals are listed in table 3.3. An additional 20 kHz high-pass filter was used for the measurement of the AE signals emitted during fracture of PP and PEEK. This removes part of the information content of the AE signals of these two polymers, but was necessary in order to avoid overloading the AE amplifier.
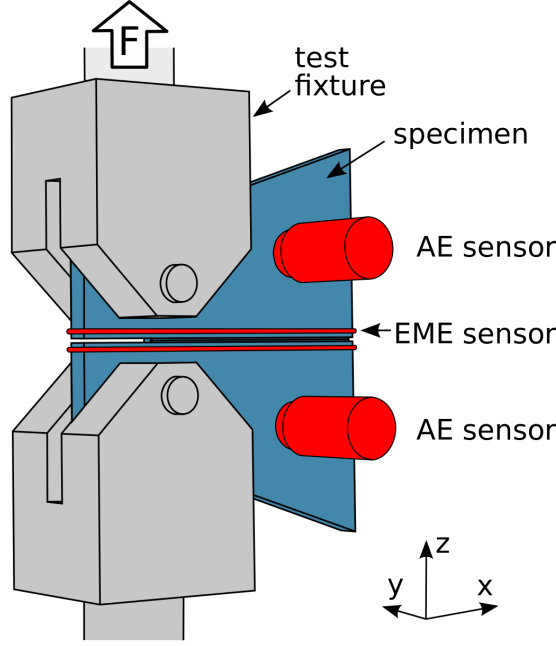
Figure 3.14: Test setup to induce mode I fracture to TDCB specimen made from polymers.

Table 3.3: Acquisition parameters used for AE and EME signal recording during flexure tests.

Channel	Threshold [dB_{AE}]	Preampl. [dB]	Sample rate [MS/s]	PDT [μs]	HDT [μs]	HLT [μs]
AE	40	20	10	100	1000	300
$EME_{(RTM6/PTFE)}$	42-45	20	5	500	1000	300
$EME_{(PEEK/PP)}$	42-45	0	5	500	1000	300

The emitted electric field is expected to show a polar character, oriented normal to the crack surfaces. Thus, the orientation of the EME sensors has to be chosen accordingly. Therefore, for the detection of the emitted directional electric fields, two copper wires of 0.5 mm diameter were placed around the specimens, one wire above and one below the notch, thus effectively forming a type of capacitor with "plate" normals directed along the z-axis.

The electric fields generated by the macroscopic fracture surfaces of the polymer specimen are strong enough to be detected with little or no amplification, but differ enough in strength for the different polymers used that two different setups were used for the acquisition of these signals. For the RTM6 and PTFE specimen, only the first, "internal" preamplifier of the measurement setup presented in section 2.4.2 was

48

used, leaving the total amplification at 20 dB. The fracture of the other materials, PP and PEEK, resulted in signals that exceeded the working range of this "internal" preamplifier. Here, we still used the JFET amplifier, but decreased the input voltage by adding a 220 pF capacitor in parallel to the input resistor, thus increasing the input capacitance. This resulted in a total amplification of 0 dB.
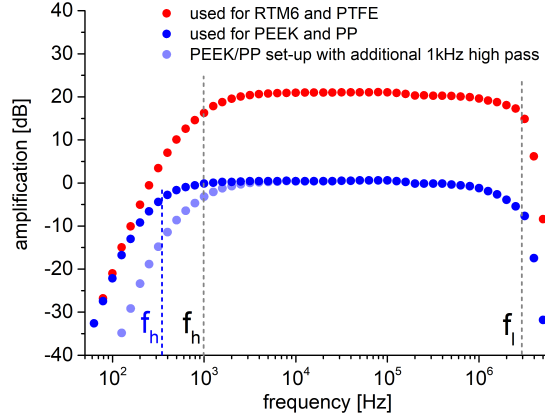

Figure 3.15: Measured transfer functions of acquisition setups used herein, with cutoff frequencies of the low and high-pass filters.

Figure (3.15) shows the amplitudes of the transfer functions of the two different applied amplification setups. While the setups for the "weakly" emitting polymers (RTM6 and PTFE) have the same frequency characteristic as the full setup (as presented in section 2.4.2), the increase of the input capacitance for the PEEK/PP setup also results in a slight shift of the high-pass cutoff frequency towards lower frequencies. Between the cutoff frequencies, which mainly reflect the bandpass characteristics of the acquisition board, the transfer functions of both amplification setups are almost constant.

The EME acquisition parameters are listed in table 3.3. The thresholds were set between 42 dB_{AE} and 45 dB_{AE} (due to minor variations in noise floor amplitudes over the course of the experiments).

To reduce the significant influence of the surrounding electromagnetic noise, the whole setup was encased by a shielding enclosure that also serves as ground potential. Conducting parts of the test fixture (*i.e.* the pin grips and pins) are connected to ground potential.

3.2.4 Results and discussion

Figure 3.16 shows representative load-displacement curves for each polymer type. The graph for RTM6 shows the expected piecewise crack propagation, with the result of multiple emission signals per specimen, i.e one per macroscopic crack propagation event. Although exhibiting strong plastic deformation, each PTFE specimen also
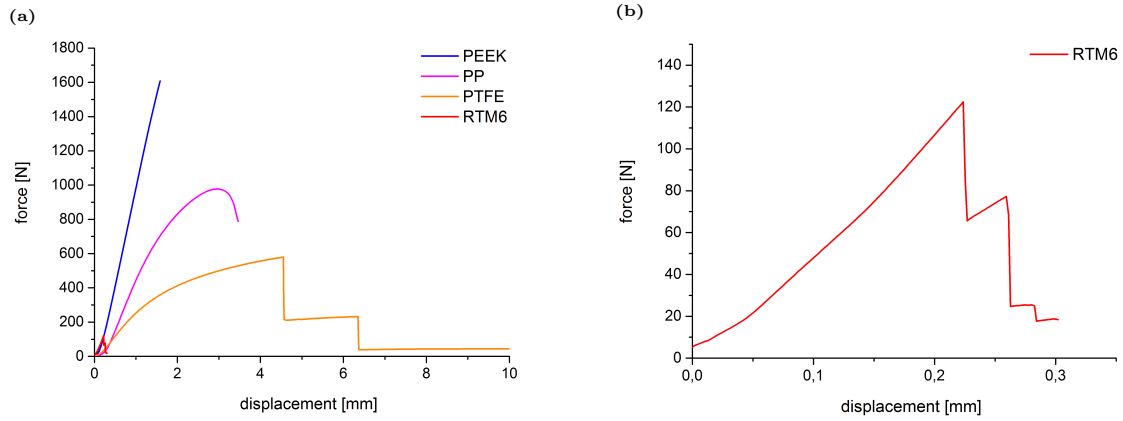
49

Figure 3.16: Typical force-displacement curves for each polymer type. (a): All tested polymers, (b): with different scale for RTM6.

provided at least two measurable AE and EME signal pairs. PP and PEEK always failed in one unstable fracture event, providing only one strong signal per acquisition channel. Here, PP additionally showed large plastic deformation before the final failure occurred.

For the sake of comparability of all EME signals, the recorded voltages signals for the PTFE and RTM6 tests were corrected for their gain to match the 0 dB amplification of the PEEK and PP tests. This reveals a considerable discrepancy in EME signal strength for the different polymers tested. Figure 3.17 shows the first $500\,\mu s$ of the detected, unamplified EME signals for all polymers tested. For PTFE and RTM6, only signals generated by the first fracturing event of each specimen are shown. For each individual polymer, the EME signal strength only varies within the same order of magnitude. A comparison between the different materials shows a variation in EME signal strength of up to two orders of magnitude. The EME signals of PEEK and PP exhibit the highest signal strengths with a few hundred millivolts peak amplitudes, while the RTM6 signals are by far the weakest with peak amplitudes of only a few millivolts.

The results of section 3.1 substantiate the assumptions about the different components of the EME signals, *i.e.* a slowly varying part considered to be generated by charge separation and an oscillating part considered to be generated by vibrations of the charged crack surfaces.

This consideration also applies to the EME signals presented in this section. Figure 3.18 (a) shows exemplary AE and EME signals for one RTM6 specimen, while figure 3.18 b) shows the corresponding FFT spectra. In contrast to the signals presented in section 3.1, with frequencies in the range between 20 kHz and 80 kHz for the oscillating part, the frequencies of the acoustic signals and the oscillating part of the EME signals presented here are much smaller. For the AE signals, this is mainly attributed to the difference in fracture surface dimensions, but also to specimen geometry and sensor placement which determine the detected wave modes.
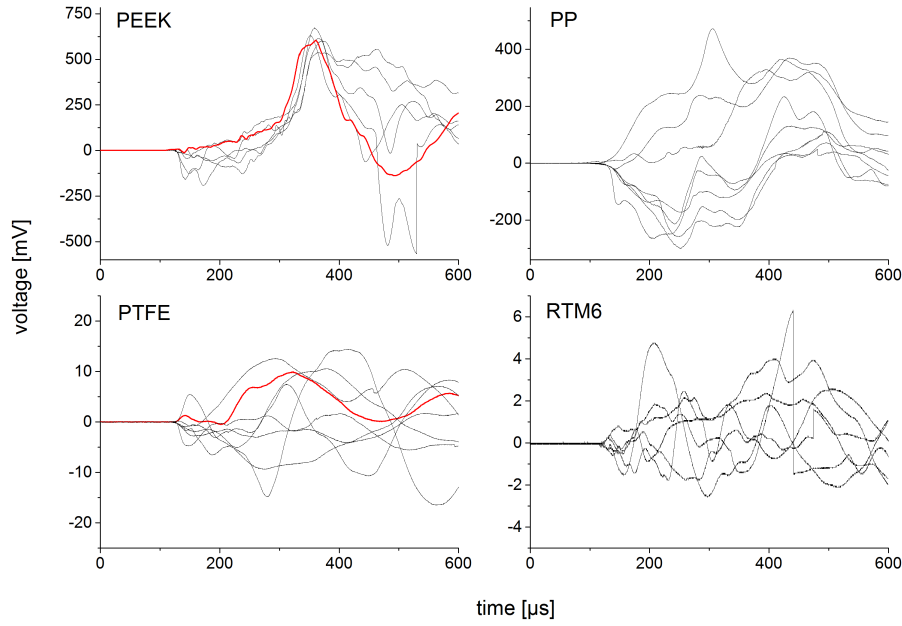
50

Figure 3.17: Unamplified EME signals for the polymers tested. For polymers with more than one fracture event per specimen (RTM6 and PTFE), only the EME signals of the first failure are shown. Signals highlighted in red are used as examples in section 3.2.4 (figures 3.23 and 3.24).

The spectra of the electric and acoustic signals differ slightly, though both are mostly limited to frequencies below 20 kHz. Assuming the same source mechanisms for the acoustic emission and the oscillating part of the EME signals (as has been discussed in section 3.1 or in [35]), this difference may be a result of different transfer functions of AE and EME sensors as well as the influences of the propagation path on the AE signal. Other, superimposing effects should also be considered. The EME sensor consists of two wires that are directly attached to the polymer specimen. Thus, relative movement of the sensor wires to each other, to the grounded test fixture parts or even relative to the charged fracture surface will result in measurable changes of the detected voltage signal. This macroscopic movement of the specimen and the attached sensors begins during crack propagation and continues after the complete failure of the specimen. Therefore, a considerable amount of the detected EME signals is attributed to this relative movement of charged materials. For this reason, it proves difficult to compare the signals frequency contents. This shifts the focus to the initial, rising part of the EME signals for the following analysis. Nevertheless, this rising part's amplitude, rise time and overall characteristic is expected to contain valuable information about the fracture processes.

Figure 3.18 also shows the expected difference of the signal's arrival time, which is the time the acoustic signal needs to travel from the source to the AE sensor. The calculated travel time of an acoustic signal in RTM6, starting at the tip of the notch, to the AE sensor is about 60 µs. For the exemplary signal pair, the measured time difference is in the same order of magnitude, but slightly below the expected

value. As mentioned in section 3.1 (where the difference between theoretical and measured values was much more pronounced), this discrepancy might be attributed to the measurement process, *i.e.* the EME signal might start earlier but with lower frequencies.
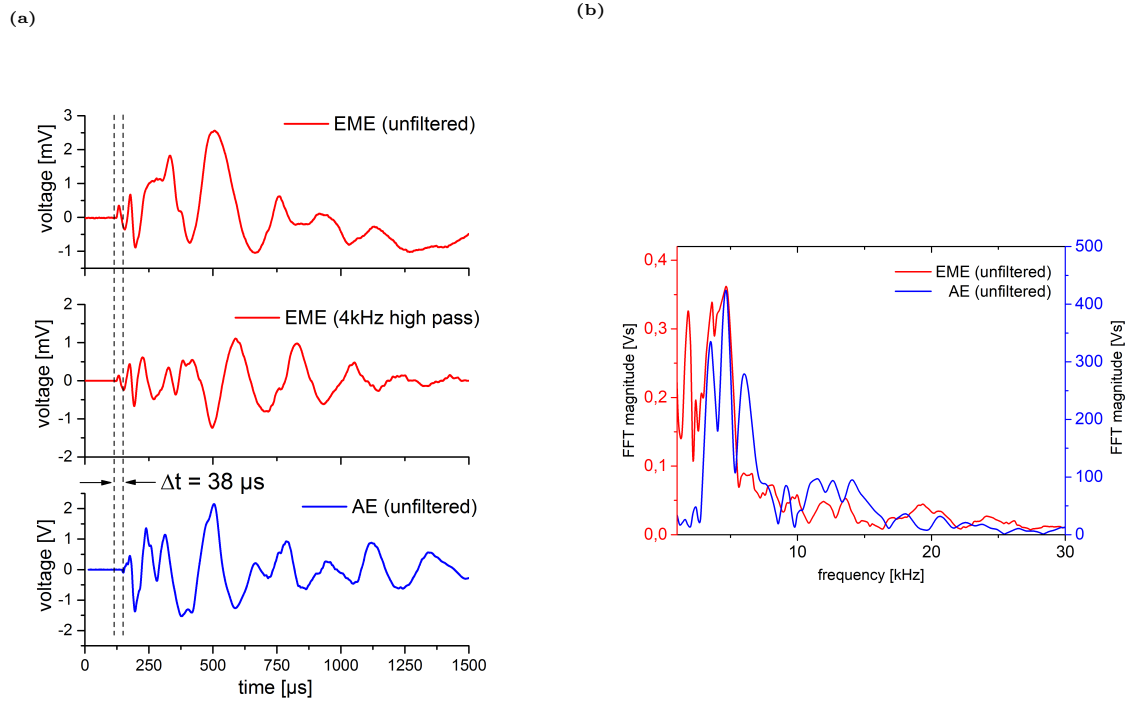

Figure 3.18: (a): Exemplary EME signal (as detected and high pass-filtered) and AE signal recorded during fracture of RTM6 specimen. (b): FFT spectra of exemplary signal pair.

PEEK

The fracture of the PEEK specimens generates the most reproducible and strongest EME signals of the four tested polymers (see figure 3.17). The load-displacement curves for the PEEK tests (figure 3.16) indicate no significant plastic deformation before brittle fracture occurs. The fracture process seems to occur in two stages. The EME signals of the first stage exhibit lower amplitudes and slower rises when compared to the second stage, and the polarities of the signals show a random character. The second stage generates a fast rise to a high EME amplitude. Surprisingly, of all detected EME signals (for all polymers) only the signals generated by this second stage of the PEEK fracture are all generated with the same polarity. No specific reason for this behaviour was found (although, assuming a random polarisation, there is also a small chance to get only one polarisation direction when testing a limited number of specimens). Figure 3.19 shows a microscopy image of the fracture

surface of an exemplary PEEK specimen, taken after the fracture tests. Here, like for the EME signals, the two stages of crack propagation are observable by means of fractographic investigation. The first part of the crack surface is fissured and rugged. Then, the surface becomes less rough and is almost completely smooth for the rest of the crack propagation. Consequently, the two stages observable in the EME signals are attributed to two different fracture processes the fracture surface indicates. The crack lengths of the two stages are approximately the same, while the first stage exhibits a larger crack surface area due to the rough surface. Nevertheless, the first stage generates a weaker EME signal. This could be due to different source-sensor orientations or partial compensation of differently charged surface fragments. Or, if the fracture process differs for both stages, so could the electrification process.
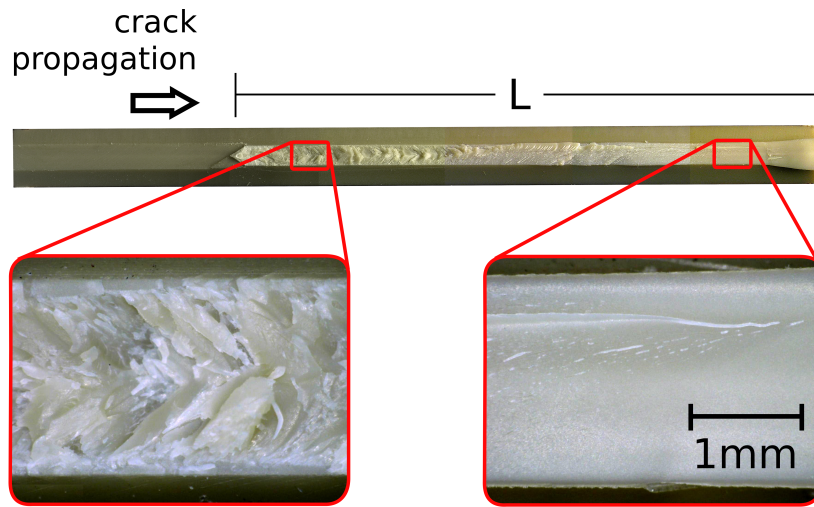

Figure 3.19: Microscopy image of PEEK specimen fracture surface. Left detail: First part of crack surface, rough with complex structures. Right detail: Much smoother surface at the end of the crack.

PP

The fracture of the PP specimens is preceded by large plastic deformation, as can be seen in the load-displacement curves (figure 3.16) and in the microscopy image of the fracture surface (figure 3.20). The crack starts at the notch and slowly propagates through the plastically deformed zone. Crazing processes are expected during this stage of ductile fracture. This results in a rough fracture surface that appears white in figure 3.20. No electric or acoustic emission was recorded during this part of the crack propagation, so all arising AE and EME signals are below our acquisition threshold and therefore within or below the level of the noise floor. At a certain point, brittle fracture starts, and complete failure of the specimen occurs. The fracture surface of this failure becomes smooth after a short and rough transition zone. The total crack length of this event is indicated as length L in figure 3.20. Strong EME and AE signals are recorded for this brittle fracture process. The EME

signals are slightly weaker than the ones recorded for PEEK, but this may be due to the slightly shorter crack lengths or the higher distance between the sensing wires (as a result of the plastic deformation at the beginning of crack propagation). The polarisation of the EME signals appears to be random. Nevertheless, in terms of signal strength and signal characteristic, the EME signals generated by fracture of PP exhibit very good reproducibility.
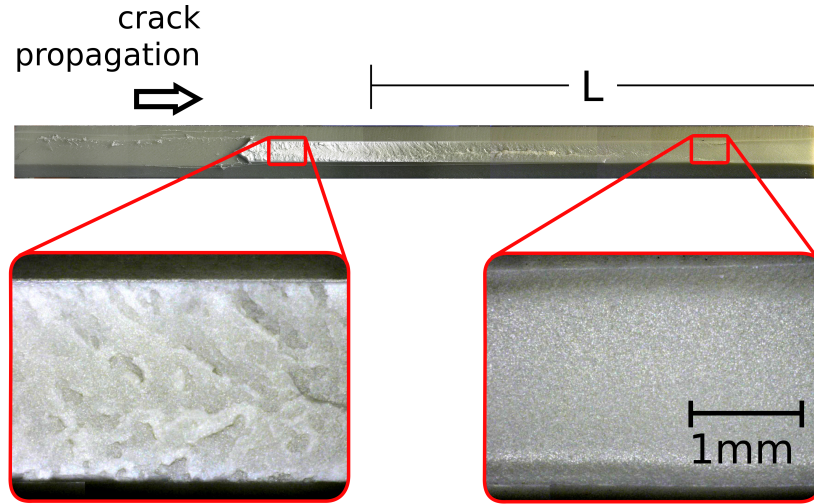

Figure 3.20: Microscopy image of PP specimen fracture surface. Left detail: Surface for slow crack growth after plastic deformation, with no measurable EME. Right detail: Surface for fast crack propagation with measurable EME, macroscopically smooth. L indicates crack length for brittle failure.

PTFE

The fracture of the PTFE specimens was accompanied by large plastic deformation. After the initial plastic deformation, sudden fast crack growth occurs in a more brittle fashion and with measurable AE and EME. As intended by the design of the TDCB specimen geometry, and in contrast to PP and PEEK, the crack stops for the first time after a certain crack length L_1. This length in shown in figure 3.21 and is flanked by two zones of plastic deformation and ductile fracture (white in figure 3.21). After another period of plastic deformation, a second fast and brittle crack propagation phase occurs (L_2 in figure 3.21) with another pair of AE and EME signals. Although the EME signals generated by the second or third macroscopic fracture event tend to have smaller amplitudes, and given some random influences on the amplitudes (like slightly asymmetric fracture and therefore slightly different source-sensor distances), not enough samples were tested to verify a direct crack length to amplitude correlation. No preferred polarisation direction was observable. Compared to PEEK and PP, the amplitudes of the EME signals emitted by the fracture of the PTFE specimens are at least one order of magnitude smaller.
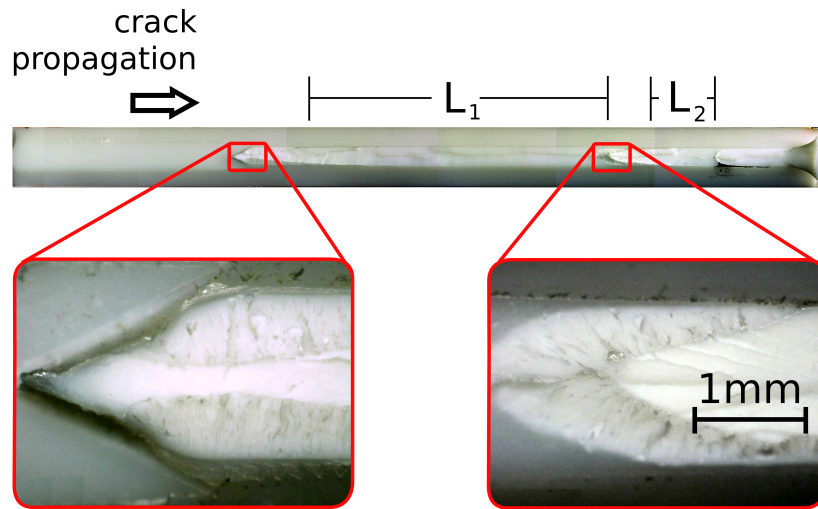
Figure 3.21: Microscopy image of PTFE specimen fracture surface. Left detail: Crack initiation after large plastic deformation. Right detail: End of first and start of second macroscopic fracture event, with plastic deformation in between. With lengths of first two brittle fracture events.

RTM6

For the epoxy resin RTM6, only brittle fracture is observed, starting directly at the notch tip. As for PTFE, the crack stops after a certain crack length L_1 (see figure 3.22). The length L_1 of this first fracture event is almost the full available specimen length. This first fracture emits a pair of well measurable AE and EME signals. Subsequently, one or more additional macroscopic fracture events occur with much smaller crack lengths. The EME signals emitted by these events are very weak, but still measurable with the applied setup. The EME signals of RTM6 are the weakest of all tested polymers. The polarisation of the first rise in EME voltage signal seems to be completely random.

With the results from the fracture tests, an evaluation of the acquired EME signal's characteristics based solely on the mechanical and electrical properties of the polymers does not appear practicable. Since the polymers also exhibit different kinds of fracture mechanisms and dynamics, possible correlations between EME generation and material properties are certainly superimposed with other effects. Additional influences may also be the inter- and intramolecular bonding or the chemical composition in general. In any case, additional investigation is needed.

Crack propagation velocities

For the determination of the crack velocities, it is assumed that the voltage signals at the EME sensors rises as long as the crack surface increases (and bonds are breaking) *i.e.* as long as the crack propagates. Charge relaxation is neglected, since its time
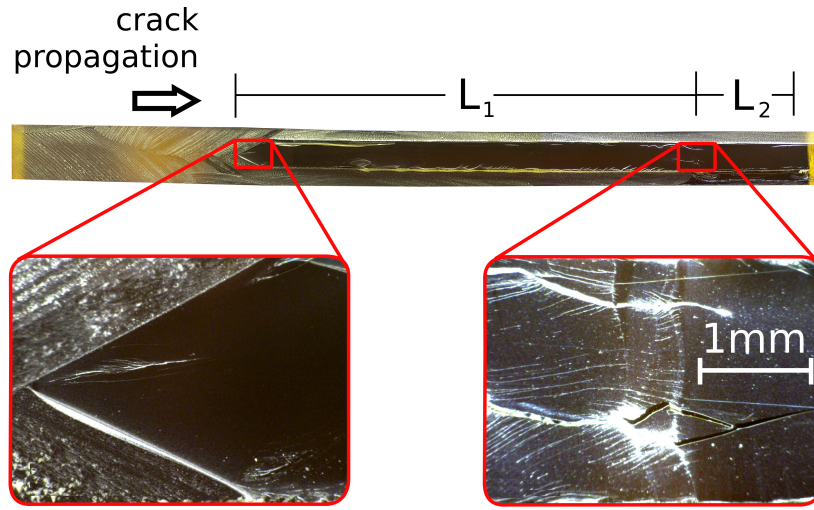
Figure 3.22: Microscopy image of RTM6 specimen fracture surface. Left detail: Start of brittle fracture, with smooth fracture surface at notch tip. Right detail: End of first and start of second macroscopic fracture event.

constants are much larger than the actual fracture times. As mentioned before, the signals are superpositions of electric signals generated by various sources. For the first signal rise, little influence by sensor and specimen movement is assumed. The higher frequencies attributed to crack wall vibration are assumed to be influenced by crack wall movement perpendicular to the crack propagation direction. Therefore, the low frequency part of the signal, considered to be generated by charge separation, seems to be a more reliable source for information about the crack's propagation characteristic. For the determination of the crack velocities, low-pass filtering is applied to all EME signals to remove the higher frequencies generated by vibrations. The filter frequency has to be low enough to filter all frequencies higher than the base signal, but has to be high enough for the filtered signal to still adequately represent the base signal's rise characteristics. For RTM6 and PTFE, a 5 kHz low-pass filter (Butterworth, 6th order) proved adequate (see figure 3.23, top), while for the steeper rises of the PP and PEEK signals, a higher cutoff frequency was needed (12 kHz and 15 kHz, respectively, Butterworth, 6th order). Furthermore, the EME signals emitted during fracture of PEEK and PP were recorded with a different setup. For comparable results, *i.e.* for matching the transfer functions of both setups used, an additional 1 kHz high-pass filter (Butterworth, 1st order) was applied to all PEEK and PP EME signals. Figure 3.15 shows the transfer function of the PEEK/PP setup with the applied high-pass filter (light blue dots), which now matches the bandpass characteristics of the PTFE/RTM6 setup. The additional filter only marginally influences the characteristic of the first rise of the PEEK and PP EME signals.

To determine the actual velocity profiles, a method as is illustrated in figure 3.23 is used. After filtering the component of the EME signals that are attributed to pure
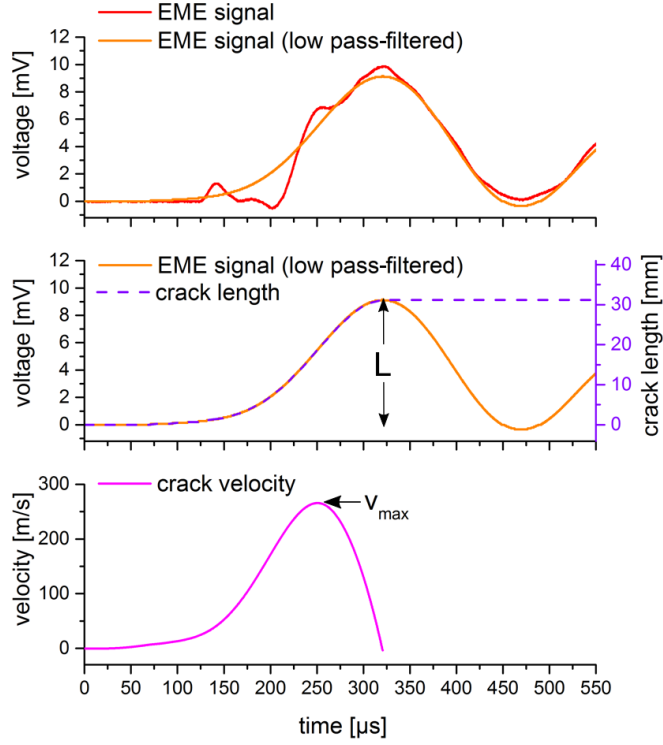
Figure 3.23: Method of crack velocity determination from exemplary PTFE EME signal. Top: Application of low-pass filter. Middle: Normalising signal rise to maximum crack length as derived from post-mortem microscopy. Bottom: Velocity as derivative of crack length.

charge separation (figure 3.23, top) is obtained. Under the assumption that charges are separated as long as the crack propagates, the first signal rise is normalised to the maximum crack lengths as determined from post-mortem microscopy of the fracture surfaces. This results in a function for the time dependence of the crack tip position (figure 3.23, middle). The first derivative of this function then gives the time-dependent crack velocity (figure 3.23, bottom). This method uses additional assumptions. It has to be assumed that the density of separated charges is in fact the same for every incremental crack surface area. Additionally, it has to be assumed that the polarisation of the net charge density does not change during the propagation of the crack. For this reason, it should be noted that this method only works with half of the recorded EME signals, *i.e.* those signals that show a distinct polarity. The presented results therefore only include these signals.

For the PEEK specimens, where the crack propagates in two stages, the normal-isation cannot be done with the maximum amplitude and the total crack length. For the different stages, the ratio of the amplitude rises differs from the ratio of the crack lengths. This indicates a difference in surface charge density for the two stages.
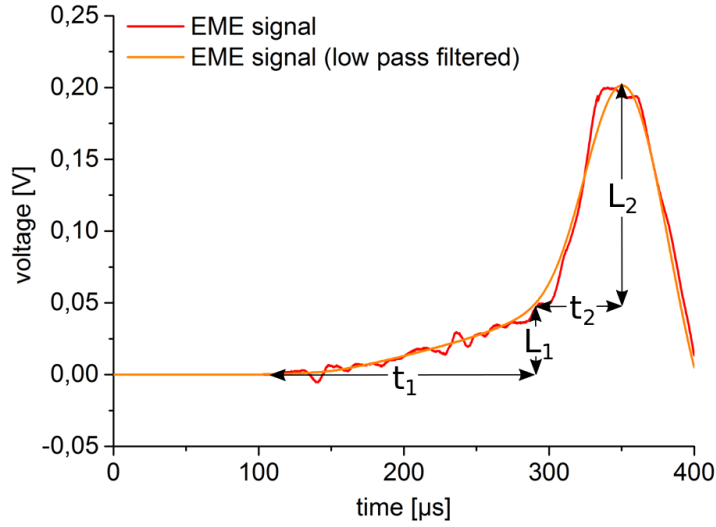
57

Figure 3.24: Two stages of crack propagation of PEEK fracture. Normalisation of crack length is carried out for each stage independently.

Therefore, the velocities were determined separately for each stage, as indicated in figure 3.24.

Table 3.4 summarises the obtained maximum crack velocities v_{max} for unstable crack growth for each polymer. For comparison, the transversal sound velocities v_T and the respective Rayleigh wave velocities v_R are also given. These values were calculated using Bergman's approximate [107], with the material parameters shown in table 3.2. The obtained values for v_{max} vary greatly for the different polymers, while all of the velocities are below the rayleigh wave velocities that define the upper limits for the crack propagation velocities in these solids. For PEEK, the second stage of its fracture has the highest crack propagation velocity, whereas the crack propagates much slower in the first stage. Of all the tested polymers, PTFE features the lowest value for v_R. This is reflected in the obtained crack propagation velocity. The velocity values obtained here are not compared to polymer crack velocities from literature, since the crack propagation velocity depends on the local stress states and therefore on the specific specimen geometry as well as potentially existing residual stresses originating from the material's processing conditions. Nevertheless, the relation between the derived maximum crack velocities and the Rayleigh wave velocities indicate that the proposed approach could lead to meaningful crack velocity profiles. The errors for the velocities given in table 3.4 are the standard deviation derived from the averaging process. Additional error sources are the choice of the low-pass filter frequency as well as the determination of the total crack length. Especially for the materials with partially ductile crack propagation, the determination of the beginning of the EME signal generating brittle crack may prove challenging. These influences differ for the different polymers, but are estimated to be of the same order

58

Table 3.4: Transversal wave velocities, Rayleigh wave velocities and calculated maximum crack propagation velocities for the tested polymers.

Material	v_T [m/s]	v_R [m/s]	v_{max} [m/s]	$\sigma_{v_{max}}$ [m/s]
RTM6	983	926	466	± 121
PTFE	337	321	226	± 48
PP	761	720	673	± 185
$PEEK_{stage1}$	982	924	210	± 40
$PEEK_{stage2}$	982	924	853	± 132

as the standard deviation.

4 EME of carbon fibres

For the investigation of electromagnetic emission generated during fracture of CFRP, the first steps are measurements on the individual components of CFRP. The previous chapter presented measurements with different types of polymers. In this chapter, experiments conducted to measure electromagnetic emission generated by fracture of carbon fibres are presented. Tests on single fibres and thin fibre bundles of less than 50 fibres were conducted. As for the polymers, different types of carbon fibres with different cross sections and material properties were used to study the influences on the EME signals.

As for the previous chapter, the results presented here have already been published [2]. The content of this chapter is consistent with this publication and places the findings in the overall context of the project.

4.1 Tensile tests of single fibres and fibre bundles

4.1.1 Material properties

For the tensile tests, three types of carbon fibres from different classes, a high tenacity (HT) type, a high modulus (HM) type and an intermediate modulus (IM) type, were chosen.
Single fibre tensile tests on 20 single fibres each were carried out to obtain the modulus and the tensile strength of the fibre types. Fibre fixation and load application was done via mechanical clamps with cushioned clamping surfaces. A displacement rate of 10 mm/min was applied, with a free fibre length of 60 mm for the modulus determination and 10 mm for the tensile strength determination. The obtained data is summarised in table 4.1.

Table 4.1: Mechanical properties of carbon fibres used.

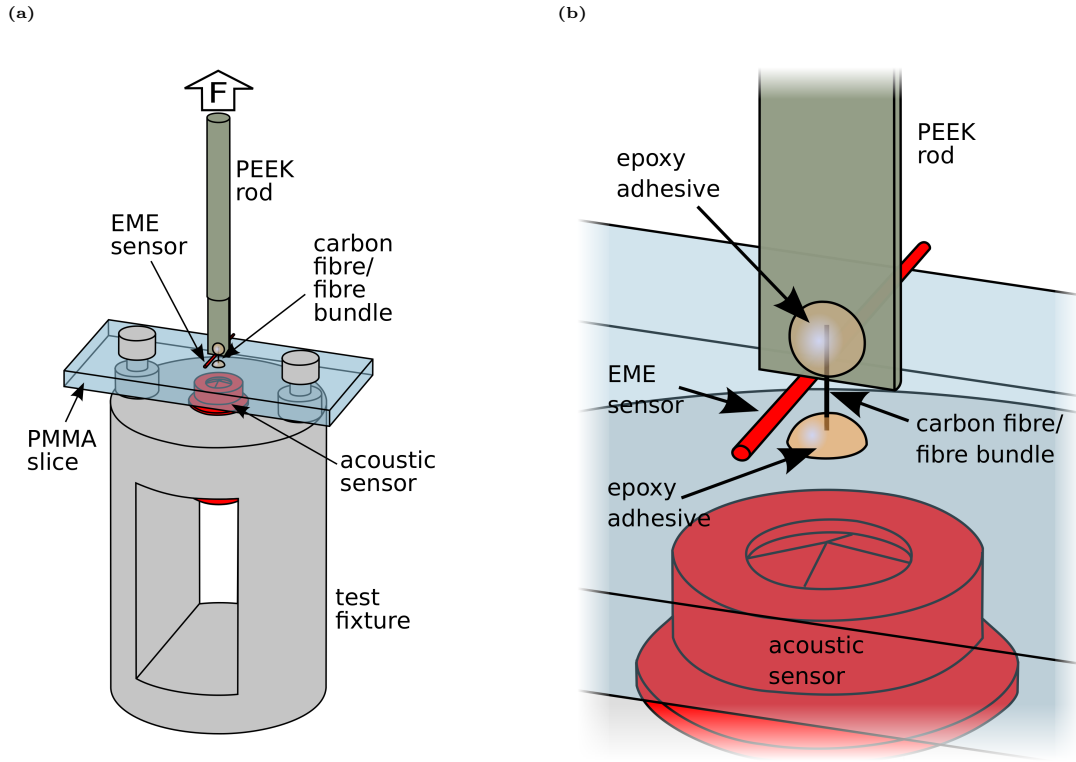| Material	Tens. str. [GPa]	Modulus [GPa]	Class
TohoTenax HTA40	3.0 ± 0.3	191 ± 15	HT
Sigrafil C030	4.2 ± 0.4	249 ± 9	IM
Torayca M40	3.0 ± 0.4	367 ± 5	HM-UHM

4.1.2 Experimental setup

Figure 4.1: Experimental setup for the fibre tensile tests. (a): Schematic of complete fixture. (b): Detail of fibre and EME sensor.

The experimental setup to measure EME generated by tensile fracture of carbon fibres is shown in figure 4.1. One end of a single fibre or a fibre bundle is fixed to the end of a flattened PEEK rod of 5 mm diameter using a two-component epoxy adhesive. This way, the fibre is located directly at the centre of the rod diameter. The other end of the fibre is attached to a PMMA plate, also using a drop of epoxy adhesive. The rod is connected to the testing machine (ZWICK ZT 5.0) and applies the load to the fibres. The load is applied displacement-controlled with a velocity of 0.1 mm/min and measured by a KAP-TC 5N load cell. The acoustic sensor is a KRNBB-PC point contact sensor located directly beneath the fibre at the bottom surface of the PMMA plate. This AE sensor placement provides the least possible influence of the propagation path, since the sensor cannot be connected directly to the fibre and has to be placed somewhere on the test fixture. The EME signals are detected by a thin copper wire near the fibres. The distance between fibres and EME sensor has to be as small as possible and was set to 1 mm.

The acoustic signals were amplified by a 2/4/6 preamplifier without internal band-pass filter, while the voltage signals at the EME sensor are amplified by the two-stage amplification setup discussed in section 2.4.2. The AE and EME acquisition parameters are listed in table 4.2. The signals were recorded in synchronised mode, *i.e.* if

Table 4.2: Acquisition parameters used for AE and EME signal recording during single fibre fracture tests.

Channel	Threshold [dB$_{AE}$]	Preampl. [dB]	Sample rate [MS/s]	PDT [µs]	HDT [µs]	HLT [µs]
AE	40	40	5	10	80	300
EME	40	40	40	50	800	300

a threshold is exceeded on one of the channels, signals on all channels are recorded simultaneously.

4.1.3 Results and discussion

EME measurements with capacitive probes during tensile tests of fibre bundles containing a few thousand carbon fibres have been conducted before and reported in [69, 108]. The EME signals emitted by failure of single fibres before the failure of the whole bundle reported in these texts are dominated by the bandwidth of the applied sensor system, *i.e.* all show a characteristic form of a fast exponential rise and a slow exponential decay, which reflects the characteristic response of the applied sensor system to a step function in input voltage. Furthermore, all detected signals of carbon fibre fracture reported in [69, 108] exhibit the same polarity.

Figures 4.2 (a) and (b) show EME and AE signals detected during the fracture of exemplary HM and IM type carbon fibres. The EME signals exhibits the fast rise that has been reported before. Only a small fracture of all recorded signals exhibit this kind of rise. As for the polymers, the rise times are expected to correlate with the fracture times and velocities. The measured rise times are in the range of 200 ns for all tested fibre types, which is the lower limit of our measurement equipment (3 MHz low-pass filter).

Figure 4.3 (b) shows the response of the acquisition system to a step function (20 ns rise) generated by an arbitrary waveform generator and normalised EME signals for the three fibre types. Since all signal rises are identical to our system's step response, the actual rise times cannot be determined with the current setup and are possibly of the same order of magnitude or smaller. Considering crack propagation velocities of the order of 10^3 m/s and crack lengths in the range of a few µm, the crack propagation times are expected to be in the nanosecond range. In a more detailed approach, Sause *et al.* [34], combining AE measurements and FEM modelling of single fibre fracture, obtained a total crack duration of 1.2 ns for carbon fibres with comparable diameter. Therefore, an acquisition board with an appropriate bandwidth and sample rate is needed to measure these fast processes.

After the fast initial rise, the characteristics of the EME signals vary for every recorded signal, and no distinct characteristic can be assigned to a specific type of carbon fibre. This may be attributed to the nature of the fracture process. All
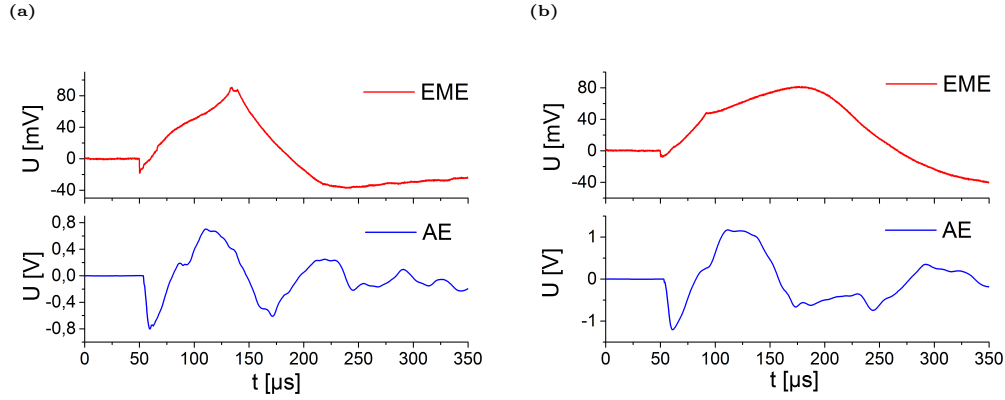
Figure 4.2: Exemplary EME and AE pairs, exhibiting step-like rise time. (a) HM type fibre (b) IM type fibre.
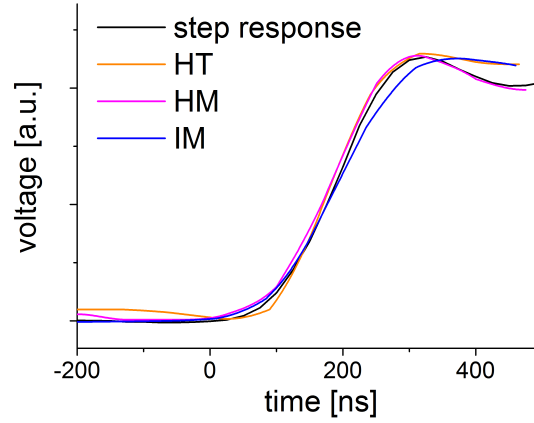

Figure 4.3: Step-type EME signals for three fibre types in comparison to the measurement system's response to 20 ns step function. Normalised.

three fibre types showed similar behaviour for this tensile test and fractured into several fragments that, caused by the released energy, moved in arbitrary directions. The charges and the movement directions, with respect to the sensor, of the fibre fragments then determine the further characteristics of the EME signals.

The majority of the recorded EME signals are of the kind that is shown in figures 4.4 (a) and (b). These signals do not exhibit the first sharp signal rise. Instead, the voltage signal increases much slower. A possible explanation might be that the actual fracture signal is not recorded due to the relative orientation of the fracture surfaces and the sensor, and only the movement of the charged fragments contributes to the detected signal.

No specific polarity of the recorded EME signal was observed either. If there is a preferred polarity, as has been reported, it was not observed due to the additional random influences on the detected EME signals, *i.e.* the position of the cracks relative to the sensor and the movement of the fibre fragments.
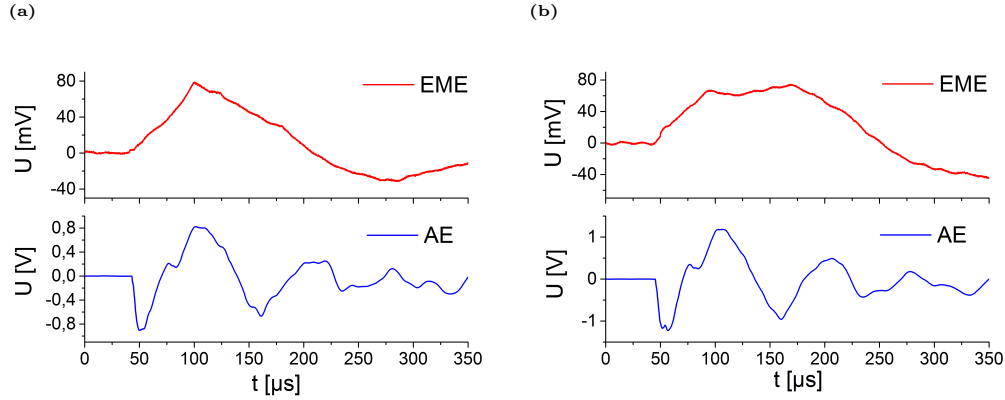
63

Figure 4.4: Exemplary EME and AE pairs, with EME signals showing no step-like characteristics. (a) HM type fibre (b) HT type fibre.

With the intention of reducing free movement of the fibre fragments after fracture, tensile tests with fibre bundles containing less than 50 fibres were conducted for the three fibre types. A clear correlation between the number of fibres per bundle and the number of emission events could not be observed. The first fibre failure occurred at about 80% to 90% of the maximum load. Each fibre fracture is accompanied by a small drop in the load-displacement curves and an AE/EME signal pair (recorded in synchronised mode). The number of such fibre fractures varied between zero and five, with the occasional occurrence of multiple events recorded in one signal. Figure 4.5 (a) shows an EME signal of the first fibre failures of a bundle of HM type fibres. Again, as for the single fibre tests, the two different kinds of signals could be observed. Here, the signals with the rapid rise could be observed more often. Due to the restriction of movement of the fragments within the fibre bundle, these signals now also exhibit the slow exponential decay that is attributed to the 1 kHz high-pass filter of the measurement system.

Final failure of the bundle, accompanied by multiple emission events, generated strong AE and EME signals, often resulting in saturation of both channels. Figure 4.5 (b) shows the AE and EME signal pair of the final fracture of a bundle of IM type fibres. Multiple step-like features in the EME signal can be observed, each attributed to a fracturing fibre.

Due to a limitation of the acquisition board and the significant influence of the dynamics of the fibre fragments, it was not possible to distinguish the fibre types on the basis of the analyses of the EME signals. Nevertheless, relatively strong EME signals could be measured for the single fibre and fibre bundle fracture tests, which clearly differ from the EME signals emitted by fracture of the polymers. This may be caused by the different materials, source mechanisms, post-fracture dynamics, crack surface dimensions and source-sensor orientations.

The acoustic emission signals (as seen in figures 4.2, 4.4 and 4.5) all exhibit near-identical characteristics, regardless of the type or number of fibres breaking. Furthermore, for every type of fibre tested, emission events occurred with additional
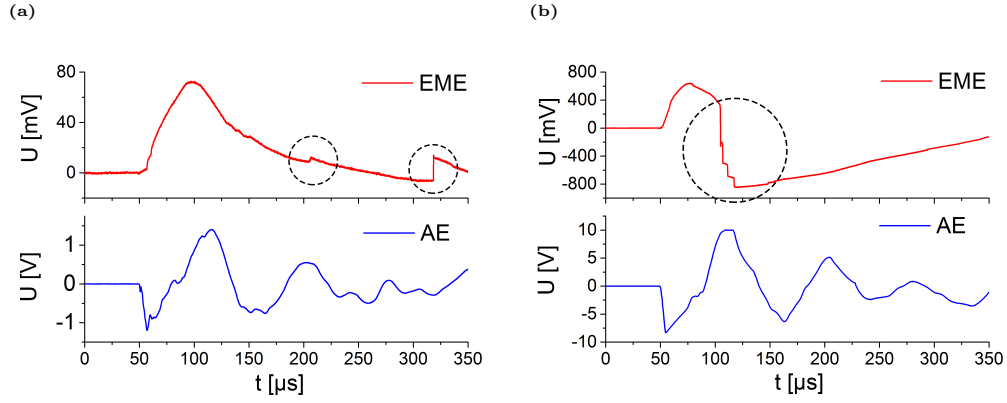
64

Figure 4.5: Exemplary EME and AE pair recorded during fracture of a bundle of HM type carbon fibres. Marked with circles: EME signatures without correlated AE signatures. (a) HM type fibres (b) IM type fibres.

step-like signatures in the EME signals, with no indication of correlated signatures in the AE signals. An example for this observation is shown in figure 4.5 (a), where two additional, differently pronounced EME signatures are recorded (marked in figure) with no visible correlated AE signature. Nevertheless, the combined measurement of acoustic and electric signals has proven to be a practical approach. EME signals that are accompanied by an AE signal can be attributed to fibre fracture with certainty and therefore can be distinguished from occasional spurious signals. Furthermore, the higher amplitudes of the measured AE signals make them excellent trigger signals for EME detection.

5 EME of mode I and mode II fracture of CFRP

In this chapter, experiments conducted to measure electromagnetic emission generated by interlaminar fracture of CFRP specimens are presented. Since there are no standard tests for these kind of measurements, two test setups were chosen that were designed to determine certain mechanical properties of CFRP specimen with a specific layer stacking sequence. In section 5.3, the employed test method is based on a double cantilever beam (DCB) test used to determine the mode I interlaminar fracture toughness of unidirectional CFRP, while the test method presented in section 5.4 is based on an end notch flexure (ENF) test used to measure the mode II interlaminar fracture toughness of unidirectional CFRP. These two setups are specifically designed to induce a single failure mode and are therefore considered to be well suited to study the EME generated by each individual failure mode of CFRP laminates.

In order to make meaningful comparisons between the results of the two experiments, the setups were designed to feature, where possible, equal properties. Mostly, the same materials were used for the test fixtures, the specimens were manufactured from the same batch of laminates, the same AE and EME measurement equipment with similar parameters, and a comparable EME sensor-to-specimen distance and sensor position were installed. The experiments were conducted with the same testing machine and within the same shielding enclosure. Differences in setup design are mainly the result of the different nature of the tests and the associated variations in geometry, such as differences in specimen dimensions and AE sensor positions.

5.1 Conductivity of CFRP

For the investigation of electric fields generated by fracture of CFRP, the electrical properties CFRP, especially its conductivity, can be of interest.

The components of CFRP, namely the matrix material and the carbon fibres, are materials that usually exhibit widely differing electrical properties. Polymers and resins (as presented in section 3.2) are generally non-conductive, while carbon fibres are mostly conductive. The bulk conductivity of the composite then depends on the properties of its constituents, but also on the individual composition of the composite.

Reported measured values of composite conductivities strongly depend on the materials, the composition, the geometries, fibre orientation and ply stacking sequence.

For the same reasons, theoretical analysis and modelling of the electrical properties can be very complex, and various methods exist [109, 110, 111]. There are also many different techniques to measure the electrical properties of composite materials on various length scales and a wide range of frequencies, *e.g.* direct measurement of voltage and current to calculate resistivity [112], electrical impedance spectroscopy [113], dielectric spectroscopy [114] or conductive AFM and scanning microwave impedance microscopy [115].

For this work, the bulk conductivity of the investigated CFRP material was measured for the frequency region of interest using dielectric spectroscopy. A small sample with dimensions of 8 mm × 4 mm × 2 mm was cut from a CFRP plate made of unidirectional Sigrafil CE1250-230-39 carbon/epoxy prepreg laminate with a $[0_{10}]$ stacking sequence. This sequence was chosen to have a specimen with three distinct orientations. Figure 5.1 (a) shows these orientations as A (orientation along the fibres), B (orientation perpendicular to the fibres and perpendicular to the layer orientation) and C (perpendicular to the fibres and oriented along the layers). The measurement setup is the same as is used for the dielectric measurements described in section 3.2.1.

Figure 5.1 (b) shows the measured conductivities for each orientation as functions of frequency.
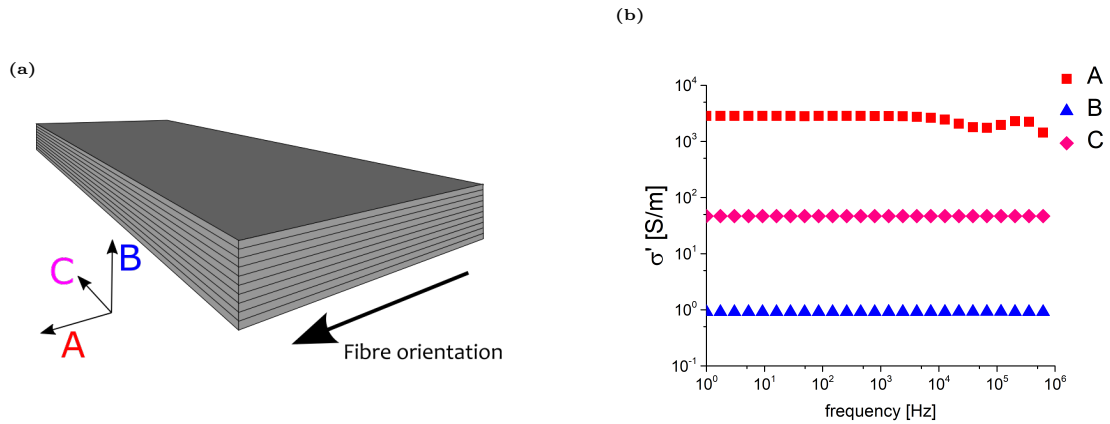

Figure 5.1: (a): Measurement direction for electric conductivity. A: along fibres B: perpendicular to fibres/ perpendicular to layers C: perpendicular to fibres/ along layers. (b): Measured electric conductivities as functions of frequency.

The measured bulk conductivities significantly differ for each orientation, with the highest values measured in the direction of the carbon fibres. The smallest values are measured perpendicular to the layer orientation. This might be a result of resin-rich regions at the interfaces between the layers, where the fibre volume fraction may be below the percolation threshold. Furthermore, the measured conductivities barely vary with frequency in the frequency range up to 1 MHz.

5.2 Preliminary test

The tests with the artificial EME source (see section 2.4.4) indicate that an EME signal will be measured when the relative distance between a charged surface and the EME sensor changes at certain time scales (depending on the measured frequencies). This may occur when the charged surface is excited by an acoustic wave. This also suggests that a similar EME signal can be measured when the EME sensor vibrates with respect to a charged surface, *e.g.* when the EME sensor is also excited by an acoustic wave. These effects might interfere with EME measurements during fracture tests, especially when the EME sensor is directly connected to the fracturing specimen, as is the case for the experiments presented in chapter 3.2. Even when the EME sensor is not directly mounted on the test specimen, the acoustic signal generated by the fracture process can travel to the EME sensor as long as it is connected to the same test fixture. One possible solution is separate mounting of the EME sensor (as was used for the experiments presented in chapter 4).

For the experiments presented in the following sections and in the next chapter, a different approach was chosen. Here, the EME sensors were to follow the movement or deformation of the tested specimen without being in direct contact with them. A mounting system that includes a mechanism to attenuate acoustic waves that are passing through was chosen. A simple way to achieve this is the application of materials that are good acoustic insulators. Polyethylene (PE) foam and polyurethane (PU) foam, both used as packaging materials, were chosen because of their ready availability.
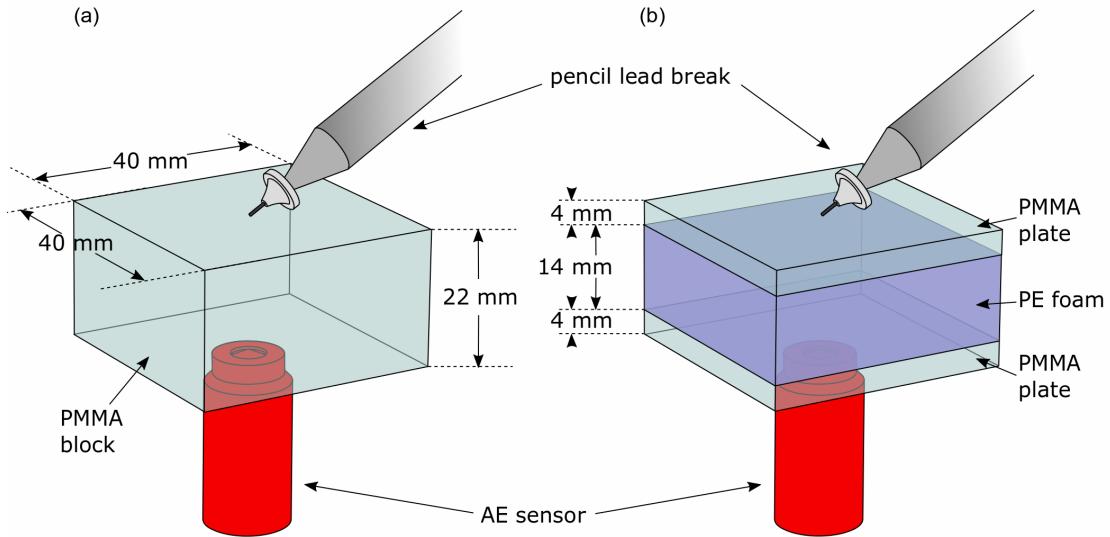

Figure 5.2: Schematic of setup for determining the attenuation of an acoustic signal by a layer of PE foam. (a) Setup without foam layer. (b) Setup with layer of PE foam.

Since no data for ultrasound absorption (for the frequency region of interest) was available for PE and PU foams, a simple test setup was used to examine the attenua-

tion of an acoustic signal along a propagation path through a combination of PMMA (used for most parts of the test fixtures) and a rigid PE foam block. A schematic of the setup is shown in figure 5.2. For a reference measurement, an acoustic signal travelling through a single block of PMMA is recorded. The block has dimensions of 40 mm × 40 mm × 22 mm. The acoustic test signals are generated by pencil lead breaks, a standard AE test source [116], and the signals are recorded by a KRNBB-PC point contact sensor mounted at the opposite side of the block (see figure 5.2 (a)). The block is then replaced by a second block with equal dimensions, consisting of two plates of PMMA with a layer of 14 mm PE foam in between (see figure 5.2 (b)). Again, test signals are generated on one side of the block and measured on the other.

The AE signals were amplified by 40 dB by a 2/4/6 preamplifier without internal bandpass filter. As acquisition parameters a threshold of 65 dB_{AE} and a sampling rate of 10 MS/s proved adequate.

A representative pair of signals is shown in figure 5.3 (a), with the respective frequency spectra shown in figure 5.3 (b). The total energy loss of an AE signal travelling through the foam, compared to the reference signal, is 99.5%. Here, frequencies up to 40 kHz are attenuated by approximately 20 dB, while frequencies above 70 kHz are attenuated by up to 50 dB.

The flexible PU foam was not tested, but a similar or even greater attenuation is expected because of the higher elasticity of the material and a higher content of air-filled cells.
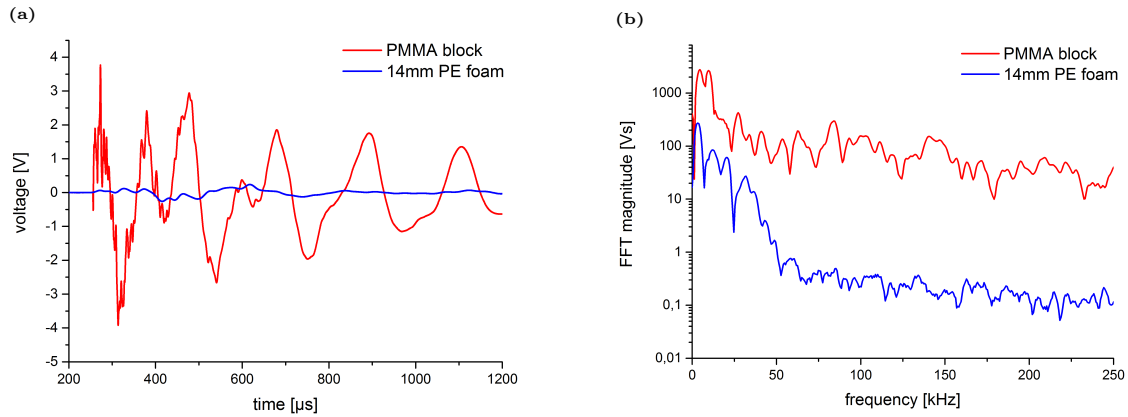

Figure 5.3: (a): Acoustic signals recorded with and without layer of foam. (b): FFT of same signals.

The experiment shows a significant attenuation of acoustic waves travelling along a path containing a few millimetres of solid foam. The EME sensor mounts for the experiments presented in the following sections are designed in a way that every acoustic wave reaching the EME sensor has travelled a distance of at least 10 mm trough solid foam (PE or PU foam) and therefore is greatly attenuated. Thus, influences of EME sensor vibration on the EME signals are considered to be minimal.

5.3 mode I fracture of CFRP

5.3.1 Specimen preparation

All CFRP specimens for the experiments presented in the following chapters were fabricated from unidirectional Sigrafil CE1250-230-39 carbon/epoxy prepreg laminate. Following the manufacturer's recommendations, the curing process consisted of 90 minutes of curing in a heat press with vacuum bagging at a temperature of 130°C and a pressure of 0.7 MPa. Furthermore, all specimens were conditioned and tested at standard climate conditions (23°C ± 2°C, 50% ± 10% relative humidity), in accordance to DIN EN ISO 291 [117].

The specimens for the DCB tests where manufactured based on the recommendations of ASTM D5528 [118] with a $[0_7]_{sym}$ stacking sequence. As non-adhesive insert in the midplane, serving as delamination initiation site, a foil made from ethylene tetrafluoroethylene (ETFE) was used. The dimensions of the specimens are 155 mm × 25 mm × 2.8 mm. The ETFE insert has a length of 60 mm. For the load introduction, two loading blocks made from PMMA are attached to the surface of the specimen with an adhesive. A schematic of a prepared specimen is shown in figure 5.4.
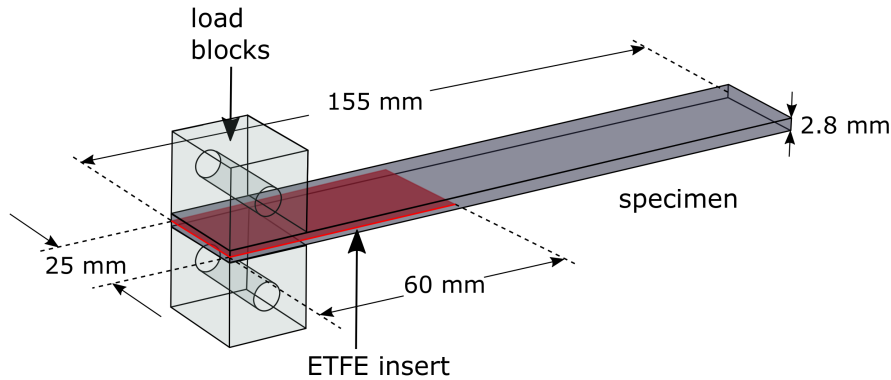
Figure 5.4: Schematic of DCB test specimen with dimensions.

5.3.2 Experimental setup

The test setup for the DCB tests is schematically shown in figure 5.5. Most parts of the test fixture are manufactured from PMMA. The bolts are made from POM, which proved to be free from measurable slip stick friction within the load blocks during the tests. The mechanical load is introduced by a tube of pultruded glass-fibre-reinforced plastic (GFRP). The compliance of the test fixture was determined to be 1.32 μm/N. For the load curves shown in this chapter, this value is taken into account.

The mechanical load is applied displacement-controlled by a universal testing machine (Zwick ZT 5.0) with a cross-head velocity of 2 mm/min. The load is measured

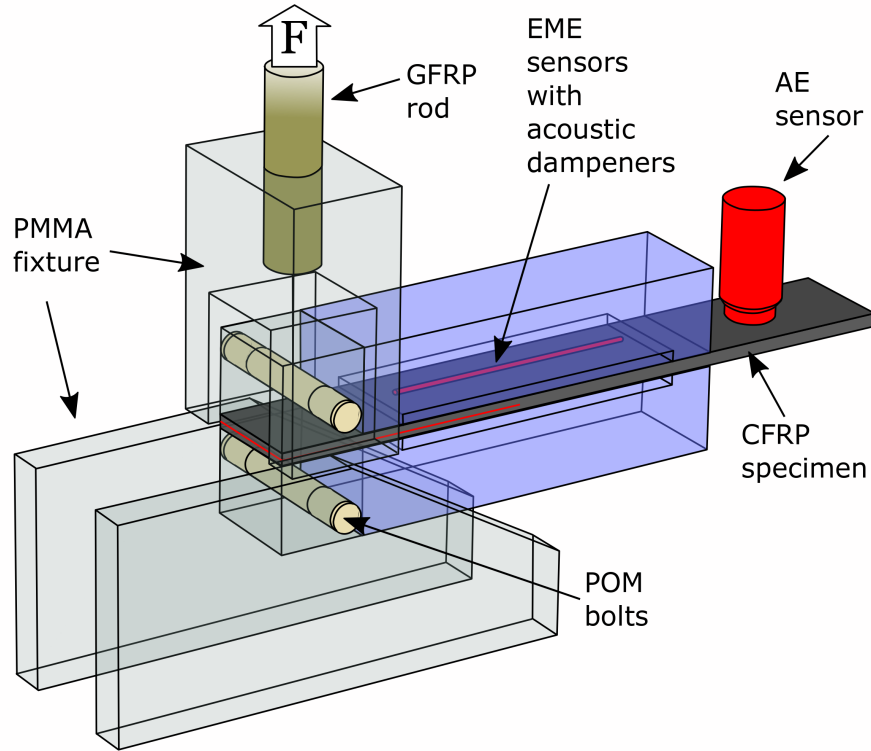with a 5 kN Xforce HP load cell.

Figure 5.5: Schematic of DCB test setup.

The test procedure following ASTM D5528 [118] consists of two steps. The initial loading of the specimen induces delamination starting from the insert. This first, potentially unstable crack is referred to as precrack. When the precrack is induced, the load is reduced to zero. This precrack then serves as natural mode I crack initiation site for the second step, where the specimen is loaded again for stable delamination growth.

The ETFE insert and its interactions with the CFRP layers during loading may generate additional EME signals. Therefore, the insert is manually removed from the specimen after the precrack is induced. The main focus of the presented results is on the EME signals generated during the second loading with no ETFE insert present.

The AE sensor is mounted on top of the specimen at the side opposite to the load introduction (see figure 5.5). To prevent grounding of the conducting CFRP specimen by bringing it into direct contact with the grounded AE sensor casing, a thin layer of PE foil is placed between the sensor and the specimen. This has almost no effect on the sensitivity of the AE measurement, but prevents the EME measurement's sensitivity from being impacted by grounding the specimen.

As acoustic sensor, a KRNBB-PC point contact sensor is used. The acoustic signals are amplified by a 2/4/6 preamplifier without internal bandpass filter and recorded

Table 5.1: Acquisition parameters used for AE and EME signal recording during DCB tests. Different AE settings were used for non-precracked and precracked specimen.

Channel	Threshold [dB$_{AE}$]	Preampl. [dB]	Sample rate [MS/s]	PDT [μs]	HDT [μs]	HLT [μs]
AE (non-precracked)	42	20	10	10	80	300
AE (precracked)	42	40	10	10	80	300
EME	21	62	10	100	1000	1000

by a PCI-2 acquisition card. The acquisition parameters that proved adequate for the acquisition of the AE signals are listed in table 5.1. Different preamplification values were used for the two stages of testing, because the initial, potentially unstable crack starting from the insert may generate stronger AE signals than the stable crack propagation due to a higher energy release.

As EME sensors, two flexible wires are placed above and below the specimen, oriented along the length of the specimen. For the reasons listed in section 5.2, the sensors are not in contact with the specimen, but are fixed to blocks of flexible PU foam. The distance between the EME sensors and the specimen is approximately 1 mm. During the test, the specimen will bend. The flexible sensors and foam blocks are attached in a way that allows the sensors to bend with the specimen, while keeping the specimen-sensor distance almost constant over the course of the experiment. A schematic of this principle is shown in figure 5.6. The lengths of the EME sensors are chosen to cover the whole length of the crack growth.

The EME signals detected by these sensors were amplified in two stages. A first preamplifier is directly connected to the EME sensors, inside the shielding enclosure. For this internal preamplifier, a junction field effect transistor in a common source circuit with a 10 MΩ input resistor was used. The voltage signal then is further amplified by a UBBV-NF35 low frequency amplifier (Aaronia AG). The complete EME acquisition setup including its properties is discussed in detail in section 2.4.2. The EME signals are also recorded by the PCI-2 acquisition card. The EME acquisition parameters are listed in table 5.1.

AE and EME signals are recorded independently, *i.e.* not in a synchronised acquisition mode.
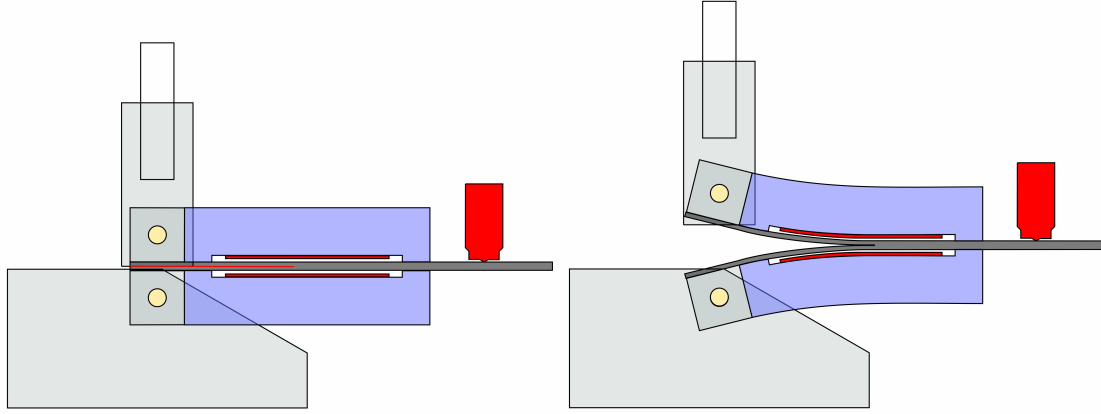
Figure 5.6: Schematic of EME sensor mounting. Flexible EME sensors are mounted to flexible foam, which allows for constant sensor distance during specimen bending.

5.3.3 Results and discussion

Non-precracked specimen

Figure 5.7 shows the load-time curve of an exemplary DCB test of a non-precracked specimen. It also shows the amplitudes of the measured AE and EME signals for this test.
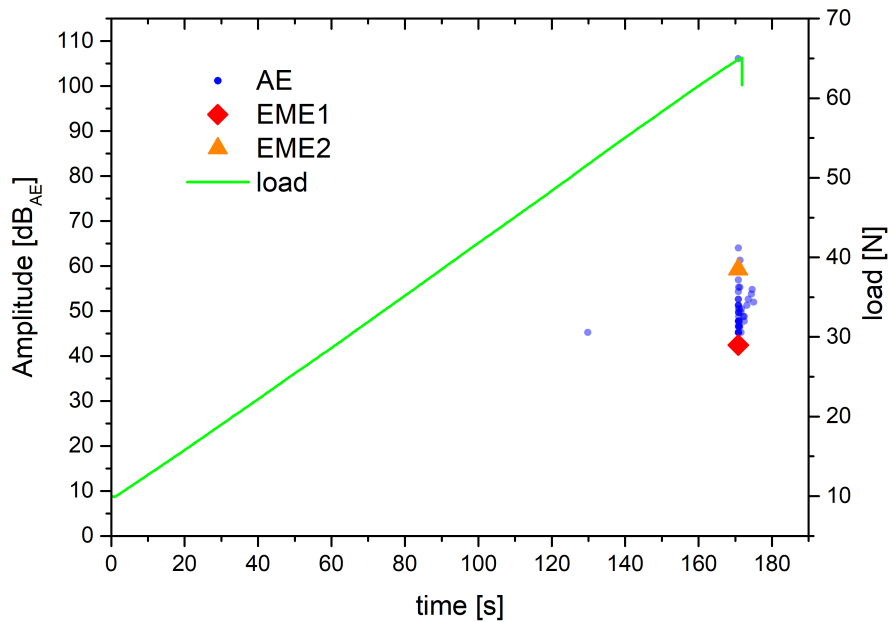

Figure 5.7: Load-time curve and amplitudes of measured signals for the precracking stage of exemplary DCB specimen.

73

Since this stage of the test is only meant to induce the precrack and the test is aborted once the precracking occurs, this precracking event is the only source for signal emission. The crack formation generated a triplet of strong EME and AE signals. A representative triplet of AE and EME signals generated by one of the specimens is shown in figure 5.8. Here and in the following sections, the EME sensor located above the specimen is denoted as EME 1, and its signals are illustrated in red, while the EME sensor located below the specimen is denoted as EME 2, and its signals are illustrated in orange. The precracking event is a macroscopic event, and the emitted signals can be considered as a superposition of multiple signals emitted in close succession.
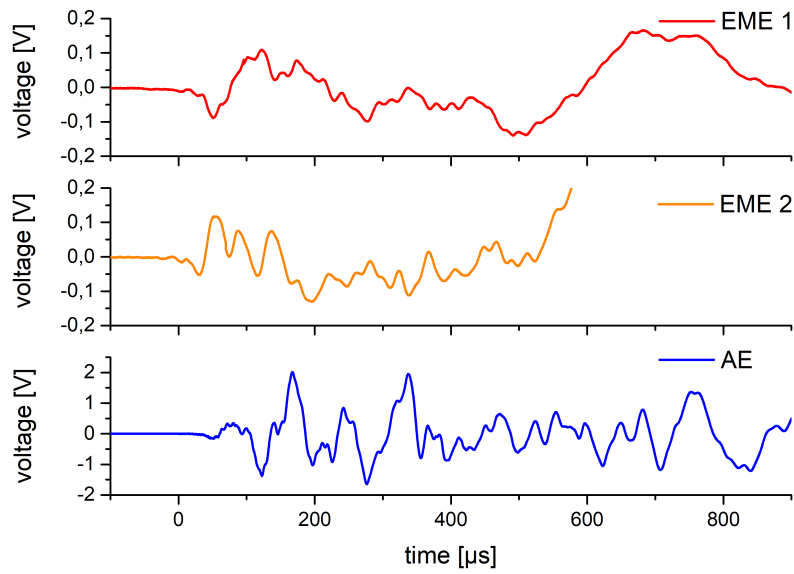
Figure 5.8: Exemplary EME and AE signals generated during the precracking of a BCD specimen.

These signals are not well suited for the purpose of analysing the electromagnetic emission generated by mode I fracture of CFRP. Here, the crack initiation site is a resin-rich zone at the end of the ETFE insert. The fracture therefore, at least for its initial moments, is not a typical mode I fracture between CFRP layers. Furthermore, the insert itself and its interactions with the specimen material during the crack formation certainly contribute to the emitted signals, though it was not tested to what degree. Thus, the signals emitted by the precracking stage are not analysed in detail at this point.

However, it can be noted that strong EME signals were recorded for every specimen in this precracking stage and that the signals considerably differ from the ones measured in the next testing stage. Furthermore, the exemplary EME signals shown in figure 5.8 were measured with the same polarity, which would not be expected when considering a simple surface dipole model for the source. In the following

74

section, a more detailed analysis of the EME signal polarities is conducted for the precracked specimen.

As for all results presented in the previous sections, there is a difference in arrival time between the AE and EME signals that mainly reflects (besides smaller effects due to different signal strengths and threshold values) the time the AE signal needs to travel from the crack to the AE sensor.

Precracked specimen

After the precracking stage, the ETFE insert was manually removed from the specimen to avoid any interference with the EME measurement. Then the specimens were loaded again for the actual DCB test. Figure 5.9 shows the load over time as well as the AE and EME signal amplitudes. Some weaker acoustic signals but no EME signals were recorded before the crack starts to propagate. When the crack finally starts propagating, which can be identified in the figure by the first drop in the load curve, new fracture surfaces are created. This is accompanied by the emission of strong AE and EME signals. As the crack propagates through the specimen, more AE and EME signals are recorded, with increased emission activity during phases of stronger crack propagation.
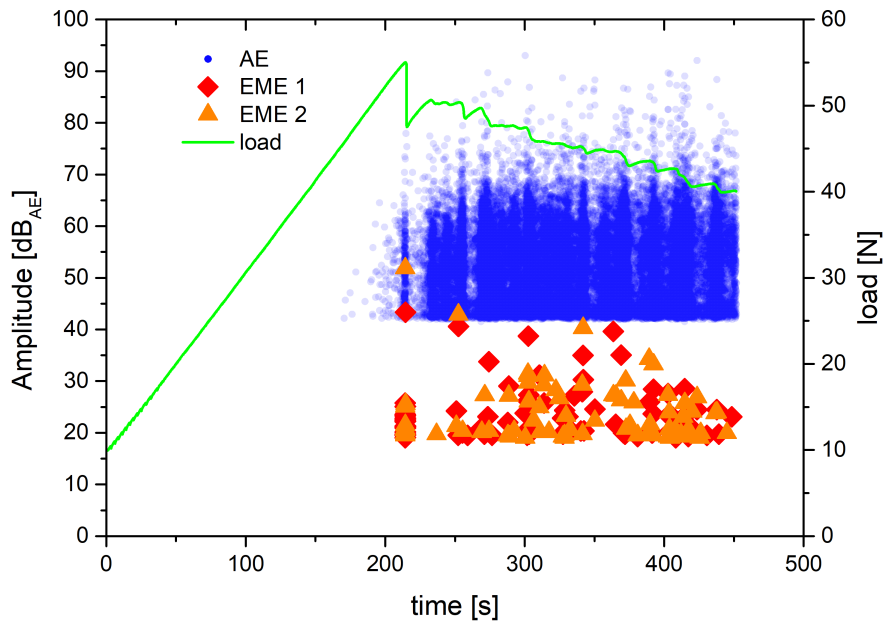

Figure 5.9: Load-time curve and amplitudes of measured signals for exemplary precracked DCB specimen.

For the acoustic emission, the signal amplitudes should correlate with the energy released by the fracture events and therefore, weaker signals are expected for the

later stages of the test. However, the distance between the emission source and the AE sensor decreases as the crack propagates. Therefore, the AE amplitudes appear to increase during the test.

The distance between the EME sensors and the propagating crack should remain constant, since the EME sensors cover the whole region of the specimen where the fracture occurs. The decrease in EME signal amplitudes over the course of the test may therefore directly correlate to the decreasing energies released by the growing fracture.

Figure 5.9 also shows the differences between the amplitudes of the AE and EME signals. This is a direct result of the different sensitivities of the two applied sensor systems. Even with an amplification of 62 dB for the EME channels and an amplification of 40 dB for the AE channel, the amplitudes of the measured EME signals are much smaller.

For a further analysis of the signal amplitudes, the amplitude distributions are plotted. Figure 5.10 (a) shows the number of signals for each amplitude interval. For the analysis, only the last four (of 12) tested specimens were used, because the measurement settings were slightly changed during the tests, but are identical for those four specimens.
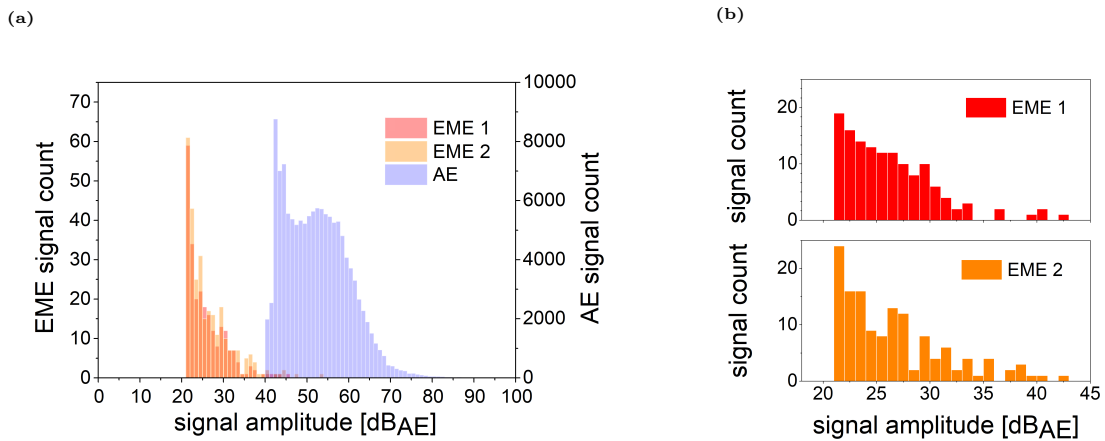

Figure 5.10: (a): Signal count over amplitude for AE and EME signals of four DCB specimens. EME and AE signal amplitudes are plotted with different scaling. (b): Signal count over amplitude only for EME signals measured in pairs.

On the lower end, the amplitude distributions are limited by the threshold values, which are set slightly above the noise floor. Assuming the distributions are similar for AE and EME signals, *i.e.* every AE event is accompanied by an EME event with a correlating signal amplitude, while neglecting effects on the AE signal amplitude distribution caused by a changing source-sensor distance, only the high amplitude slope of the EME distribution was recorded, and most of the EME signals generated alongside weaker AE events were not measured, because their amplitudes were below the threshold level, *i.e.* below the noise floor. A significant increase in signal-to-noise ratio might result in a greater number of EME signals measured. However,

the currently used setup (comprising measurement equipment, shielding and sensor positioning) is already optimised in this regard.

Figure 5.10 (b) shows the number of signals for each amplitude interval only for signals that were recorded in pairs, ignoring emission events where only one signal was recorded on either of the EME channels. For those signals, the amplitude distributions are comparable, with the EME signals recorded with sensor 2 being slightly weaker. Since the EME sensor setup was designed to be as symmetric as possible, the similar distributions indicate a symmetric electromagnetic emission for the mode I fracture, as would be expected for the source model of a surface dipole.

When analysing the EME signals with respect to waveform characteristics two distinctively different EME signal types are found. In the following, they are denoted as EME type I and type II signals. Figure 5.11 (a) shows exemplary EME signals of type I, and figure 5.11 (b) shows exemplary EME signals of type II. For both types, one corresponding AE signal is also plotted.
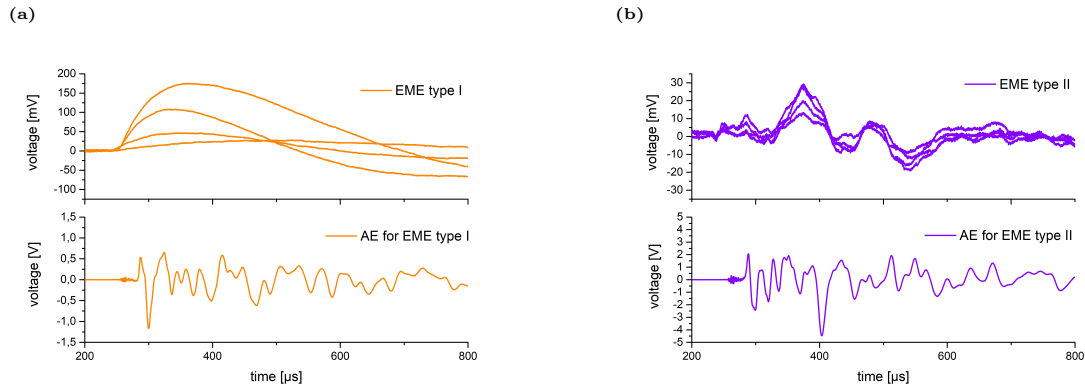

Figure 5.11: Exemplary EME signals for two different types measured during DCB tests. AE signals measured coincidently with each EME signal type are added. (a): type I signals, (b): type II signals.

EME signals of type I can be characterised by an almost smooth waveform that rises to its peak amplitude and then slowly decays. As is discussed in section 3.1.3, the decay characteristic is likely to be a result of the measurement system's 1 kHz high-pass filter. However, rise times and amplitudes significantly vary for the type I signals.

EME signals of type II are more complex and consist of multiple components. The underlying, low frequency oscillation is characteristic and almost identical for all type I signals. Superimposed are oscillations with higher frequencies and noise (since type II signals are generally weaker, the noise seems more pronounced here). The mechanism responsible for the two different EME signal types is unclear. Type II signals are comparable to the EME signals recorded for the polymer mode I fracture tests (presented in section 3.2.4), where for some of the tested polymers, the EME signals also show a characteristic behaviour (see PP and PEEK signals shown in

figure 3.17). Signals comparable to the type I signals were not observed in any of the experiments presented in the previous chapters.

AE signals for this type of experiment could be classified and associated with different failure mechanisms before (*e.g.* in [35]), by using pattern recognition techniques. This was also attempted here with the goal to possibly associate the corresponding EME signals with found certain failure mechanisms. However, an AE sensor with a different sensor characteristic, compared to the ones used in the cited literature, was used here. Different clusters for different failure mechanisms were not found (using various established clustering algorithms). Moreover, for all meaningful clustering results (resulting in two different AE signal clusters), AE signals corresponding to EME signals of type I and type II were always found in the same cluster.
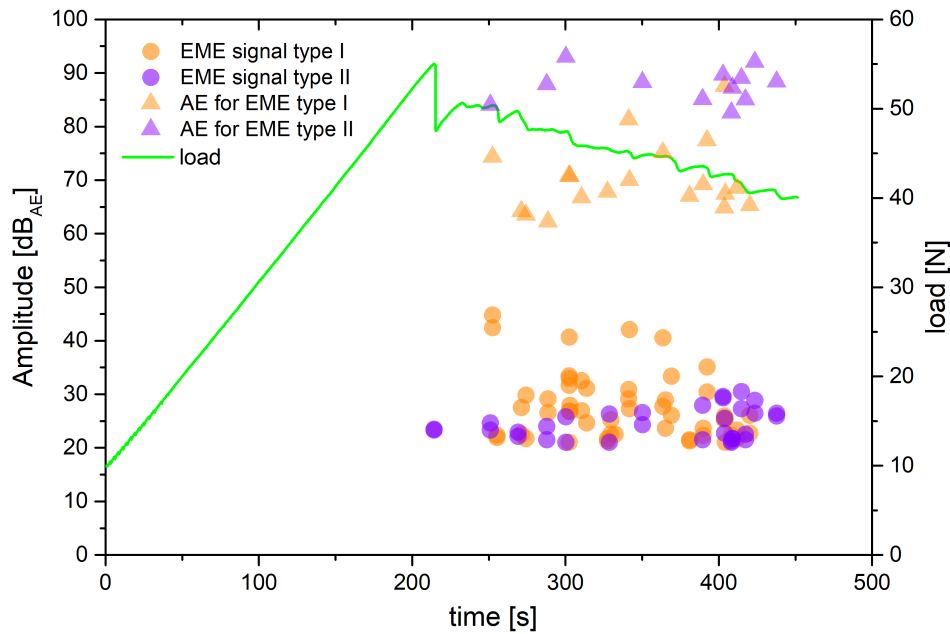

Figure 5.12: Amplitudes of the two EME signal types and coincidently measured AE signals over time for one exemplary DCB test. Load curve included for clarity.

In figure 5.12, the amplitudes of EME type I and type II signals are plotted for one exemplary specimen. The amplitudes of AE signals that were measured coincidently with one of the two EME signal types are also plotted. The load curve is added to identify the stages of the test. EME signals generated by the first initial crack propagation (illustrated by the first significant drop in load) were not included, since they are composed of multiple signals emitted in close succession and could not be assigned to one of the EME signal types.

EME signals of type I have a much greater amplitude at the early stages of crack propagation, while EME signals of type II are weaker but become stronger and more frequent as the crack propagates further. In contrast, AE signals recorded coinci-

dently with EME type II signals have higher amplitudes than the ones measured alongside EME type I signals.

Though the gaps between the measured amplitudes of AE and EME signals are significantly different for the two signal types, they are quite consistent for each individual signal type. Therefore, this gap can be considered as another distinctive feature of the two EME signal types.

The differences between both EME signal types might point to different source mechanisms, which cannot be distinguished by the analysis of the measured AE signals alone.

For all experiments presented in the previous sections, only one EME sensor was used. By using two sensors, one on each side of the propagating crack, the polarities of the electromagnetic emission can be studied. With two sensors and two possible polarities for each sensor, there are four possible combinations for the signal pair polarisations. Figure 5.13 shows one exemplary signal pair (and the corresponding AE signals) for each polarisation combination.
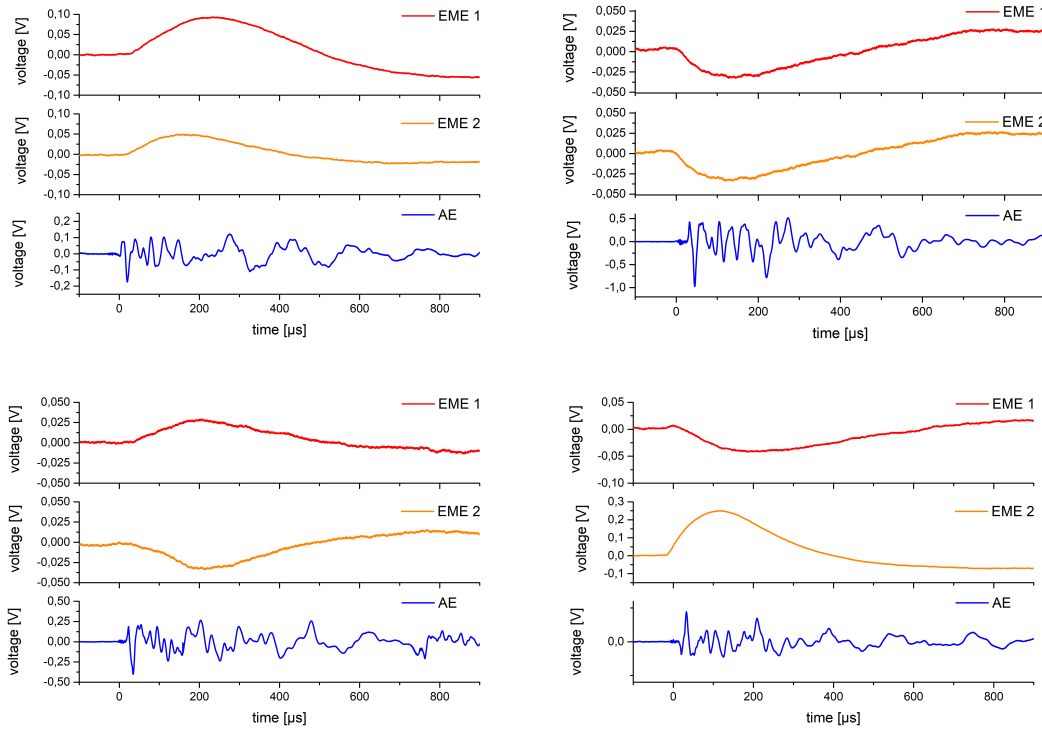

Figure 5.13: Exemplary EME signal pairs for the four different combinations of signal polarisation, coincidently measured AE signals included.

The figure only shows signals of type I, but the following analysis was done with signal pairs of both types. For the same four specimens for which the amplitude analysis was carried out, the polarities of all signal pairs were counted. Table 5.2

shows the percentages each different polarity combination appeared for each specimen.

Table 5.2: Relative frequencies of polarisation combinations of EME signal pairs for four DCB specimens.

EME polarisation	Specimen	09	10	11	12	-	total
		36.3%	42.1%	23.6%	47.4%		39.7%
		48.8%	44.7%	41.2%	34.1%		42.1%
		6.0%	5.3%	17.6%	5.3%		7.1%
		8.9%	7.9%	17.6%	13.2%		11.1%

With the basic source model of a surface dipole in mind, opposite polarities for the two EME sensors were expected for all or at least most of the signal pairs. However, only 18.2% of all analysed signal pairs show this kind of behaviour. For the majority of the signal pairs, the polarities are the same for both channels. For these cases, the likelihood is almost the same that both voltages are either negative or positive. The reasons for this kind of polarity distribution is unclear at this point. Since for all experiments presented in the previous chapters, only one sensor was used, it cannot be determined whether this is a characteristic of the source or whether the conductive specimen material is a relevant factor. A first step could be a repetition of the experiments presented in chapter 3.1 using two EME sensors to compare the above results with the results from a non-conductive material.

5.4 Mode II fracture of CFRP

5.4.1 Specimen preparation

The specimens for the ENF tests where manufactured based on the recommendations of ASTM 7905/D7905-14 [119] with a $[0_8]_{sym}$ stacking sequence. As non-adhesive insert in the midplane, serving as delamination initiation site, a foil made from ETFE was used. The dimensions of the specimens are 188 mm $\times$ 21 mm $\times$ 3.2 mm. The ETFE insert has a length of 45 mm. A schematic of a prepared specimen is shown in figure 5.14.
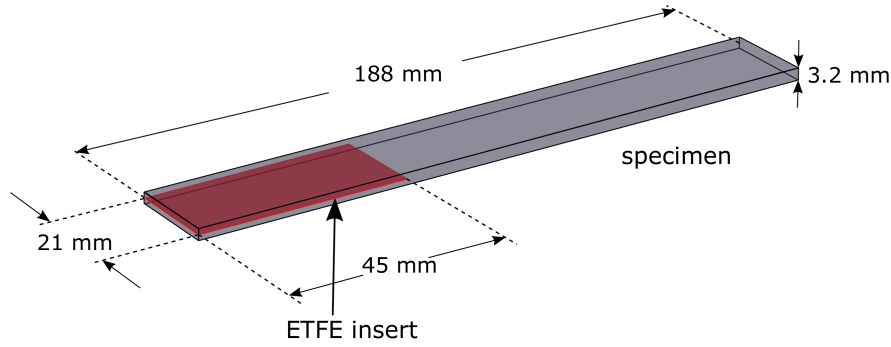

Figure 5.14: Schematic of ENF test specimen with dimensions.

5.4.2 Experimental setup

The test setup for the ENF tests is schematically shown in figure 5.15. Most parts of the test fixture are manufactured from PMMA. Loading and supporting pins are made from polyvinyl chloride (PVC). The mechanical load is introduced by a tube of pultruded glass-fibre-reinforced plastic.

The mechanical load is applied displacement-controlled by a universal testing machine (Zwick ZT 5.0) with a cross-head velocity of 0.5 mm/min. The load is measured with a 5 kN Xforce HP load cell.
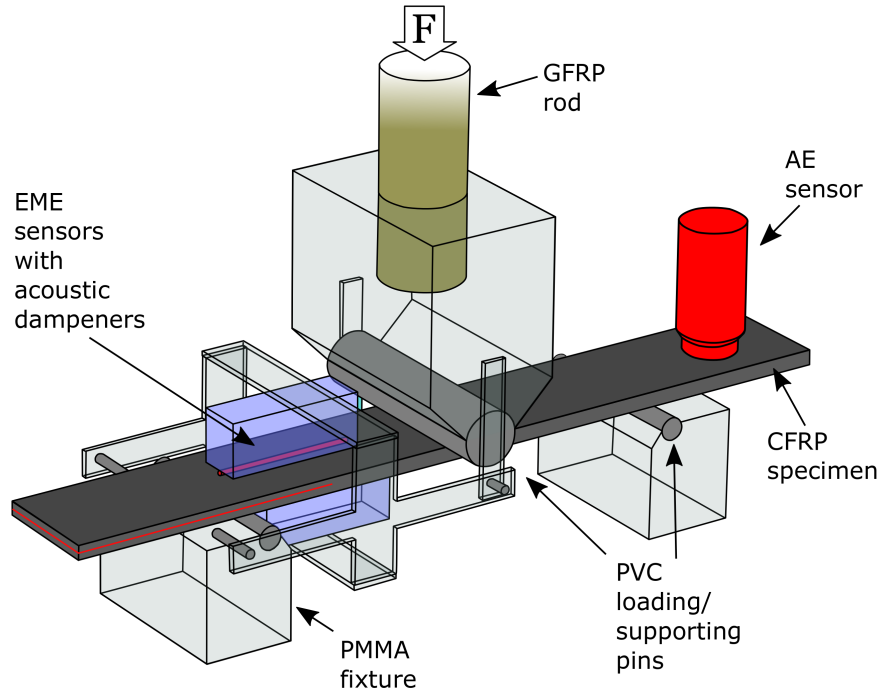
Figure 5.15: Schematic of ENF test setup.

The test procedure following ASTM 7905/D7905-14 [119] consists of two steps. The specimen is positioned on the fixture with a distance of 30 mm between the end of the ETFE insert and the supporting pin. The specimen is loaded to induce delamination starting from the insert. When this first, potentially unstable precrack is induced, the specimen is immediately unloaded. This precrack then serves as natural mode II crack initiation site for the second step. The specimen is then repositioned to a distance of 30 mm between the end of the precrack and the supporting pin. Now, the specimen is loaded again for stable delamination growth.

Similar to the DCB tests, the ETFE insert and its interactions with the CFRP layers during loading may generate additional EME signals. As for the DCB tests, the insert is manually removed from the specimen after the precrack is induced. Here, only results from precracked specimens with their inserts removed are presented in order to exclude possible influences of the inserts on the EME signals.

As acoustic sensor, a KRNBB-PC point contact sensor mounted on top and at the end of the specimen opposite to the crack and the EME sensors (see figure 5.15). The acoustic signals are amplified by a 2/4/6 preamplifier without internal bandpass filter and recorded by a PCI-2 acquisition card. For comparability, acquisition parameters similar to the ones used for the DCB tests are used. The parameters are listed in table 5.3.

As EME sensors, two wires are mounted on a movable mounting fixture, one sensor above and one below the specimen, oriented along the length of the specimen. The mounting fixture is designed to allow the sensors to follow the flexure of the specimen during the test without being in contact with the specimen, while keeping an almost

Table 5.3: Acquisition parameters used for AE and EME signal recording during ENF tests.

Channel	Threshold [dB$_{AE}$]	Preampl. [dB]	Sample rate [MS/s]	PDT [μs]	HDT [μs]	HLT [μs]
AE	40	40	10	10	80	300
EME	21	62	10	100	1000	1000

constant specimen-sensor distance of approximately 1 mm over the course of the experiment. The wires are fixed to blocks of rigid PE foam for acoustic decoupling from the rest of the setup. A schematic of this principle is shown in figure 5.16. The lengths of the EME sensors are chosen to cover the whole length of the crack growth.

For comparability, the EME acquisition setup is the same as the one used for the DCB tests. The EME signals detected by the sensors were amplified in two stages. A first preamplifier is directly connected to the EME sensors, inside the shielding enclosure. For this internal preamplifier a junction field effect transistor in a common source circuit with a 10 MΩ input resistor was used. The voltage signal is then further amplified by a UBBV-NF35 low frequency amplifier. The EME signals are also recorded by the PCI-2 acquisition card. The EME acquisition parameters are listed in table 5.3.

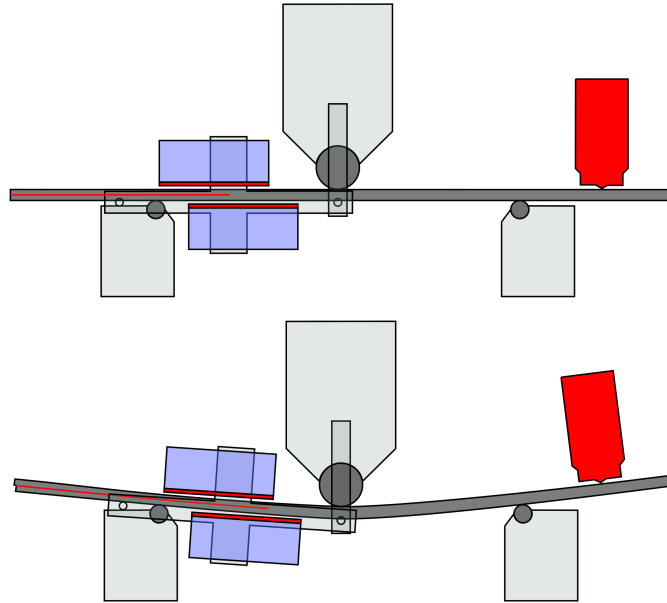AE and EME signals are recorded independently, *i.e.* not in a synchronised acquisition mode.

Figure 5.16: Schematic of movable EME sensor mounting with PE foam blocks.

5.4.3 Results and discussion

Figure 5.17 shows the amplitudes of the AE and EME signals and the load versus time for a representative ENF test on a precracked specimen. During the crack propagation, a large number of AE signals were detected. During the test series, no evaluable EME signals were recorded. For most tests, no EME signals were detected. Occasionally, as in the example shown in figure 5.17, weak EME signals were detected. These signals have very low energies and can hardly be distinguished from the underlying noise. A meaningful evaluation of these few signals is therefore not possible.

In [35], EME signals from an ENF experiment with a comparable setup are presented. However, they were recorded with a smaller sensor-specimen distance, as the EME sensors were mounted directly on the sample surface. For reasons discussed in section 5.2, a non-contact sensor mounting was applied here. Nevertheless, the additional distance of approximately 1 mm between source and sensor might not be enough to explain the differences in measured EME signal strength.
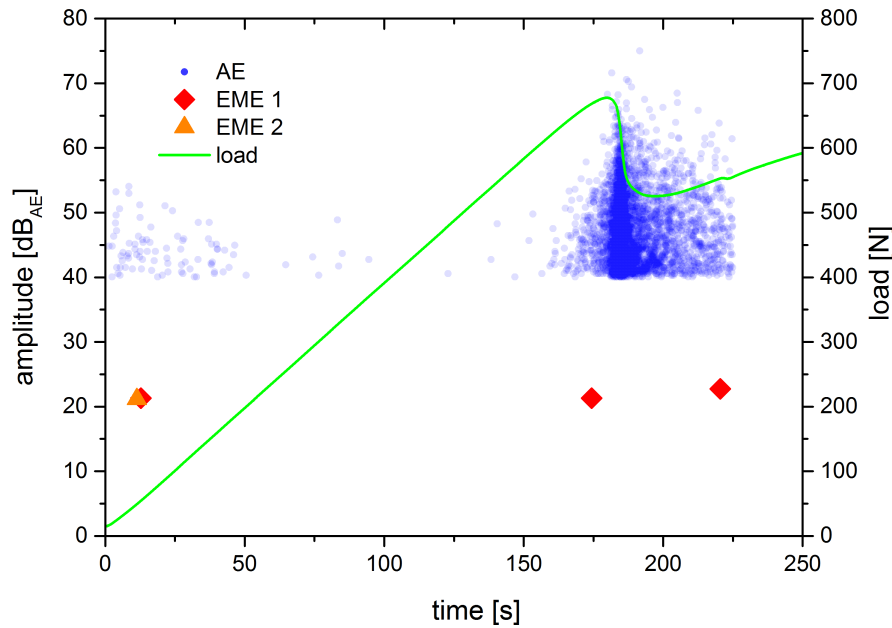

Figure 5.17: Load-time curve and amplitudes of measured signals for exemplary, precracked DCB specimen.

During the precracking stage of the experiments, however, strong EME signals were recorded. These were very strongly saturated. Because of this and the fact that the non-precracked specimen still contained the ETFE foils (whose influence on the EME signal is unclear), these signals are not taken into account here, as in the DCB tests.

Possible reasons for the different EME activities in mode I and mode II failure are discussed in the next section.

5.5 Comparison of results

While during the DCB tests many evaluable EME signals were measured, no evaluable EME signals or no EME signals at all were measured during the ENF tests. This could be due to the different crack modes. In case of mode I failure, the opposite crack surfaces move away from each other and are no longer in direct contact. However, the crack surfaces are still conductively connected via the material. In case of mode II failure, the crack surfaces continue to be in direct contact after the fracture. Possible charge separation could thus be immediately recombined.

Nevertheless, there are other differences between the two tests. Figures 5.18 (a) and (b) show the released mechanical energy-per-time interval (determined by the sampling rate of the load acquisition). The energies were calculated from the load-displacement curves as the difference between the work done by the applied load and the elastic energy remaining in the system.
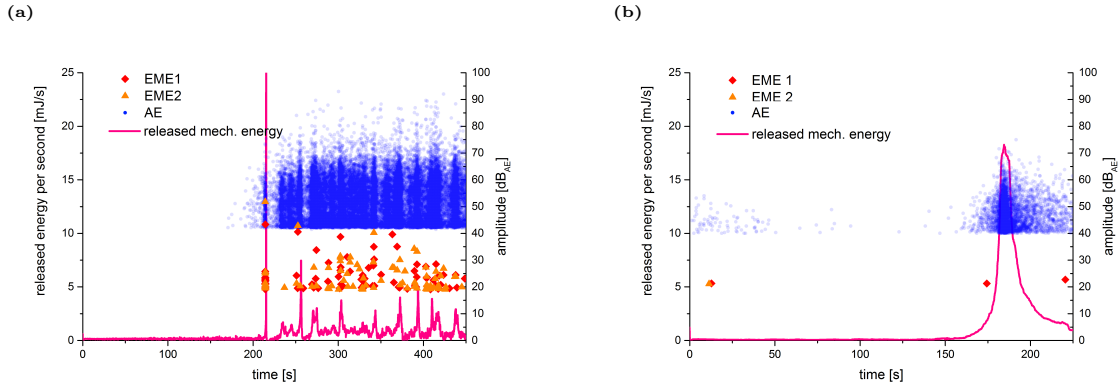

Figure 5.18: Comparison of signal energies and released mechanical energies per time (a): Exemplary DCB test (b): Exemplary ENF test.

The time-dependent energy release rate G, defined as the decrease in total potential energy per increase in fracture surface area, cannot be calculated here, since the time-dependent fracture length was not recorded (mainly because the shielding box did not allow for optical determination of the crack length during the testing). Still, with the assumptions that other mechanisms of energy dissipation can be neglected and assuming a rectangular fracture area, a mean value for G can be approximated with the specimen width and the total crack length measured after the tests. For the DCB tests, a mean value of 252 J/m^2 was calculated, while for the ENF test, a mean value of 460 J/m^2 was calculated. For the mode II fracture, slightly more energy per unit area is necessary for the crack to propagate, but both values still are of the same order of magnitude. However, a fundamental difference between the two

experiments can be observed. While in the DCB tests the energy is released in short bursts (accompanied by AE and EME), energy is released quasi continuously during the ENF tests, accompanied only by AE. In figures 5.18 (a) and (b), the amplitudes of the recorded AE and EME signals are shown. During the DCB tests, AE signals with amplitudes of up to 90 dB were recorded while most EME signals did not surpass 40 dB. Assuming a direct correlation between AE and EME strength and noting that AE signals generated during the ENF tests are almost all below 70 dB, a possible explanation for the lack of EME signals for the ENF tests could be that potentially generated EME signals were too weak to be measured by the applied measurement equipment.

Although efforts were made to conduct the tests for both fracture modes under comparable conditions (same specimen material and preparation, same experimental equipment and comparable experimental setups), the dynamics of the fracture modes differ quite significantly. It is therefore not possible to attribute the differences in EME activity or EME signal strengths to the difference in fracture mode alone.

6 Directional measurements of EME

In this chapter, experiments conducted to measure the directional dependency of the electromagnetic emission generated by the fracture of cross-ply CFRP specimen are presented. Theoretical considerations (section 2.3.2) and results presented in section 3.1.3 suggest a strong directional dependency of the EME signals generated by a fracture process. The spatial field distribution is assumed to be correlated to the orientation of the sources as well as influenced by the properties of the surrounding matter.

To induce EME sources, *i.e.* cracks, resulting from different failure modes and exhibiting a variety of different crack surface orientations, a three-point bending test setup for cross-ply CFRP specimen with varying ply stacking sequences was chosen. Four independent EME sensors are placed around the fracturing region of the specimen to measure the EME signals in different directions.

6.1 Flexure tests of CFRP

6.1.1 Specimen preparation

Like the specimens used for the experiments presented in chapter 5, the specimens used for the three-point flexure tests were fabricated from unidirectional Sigrafil CE1250-230-39 carbon/epoxy prepreg laminate. Following the recommendations of DIN EN ISO 14125 [120], the specimen dimensions are 95 mm × 15 mm × $2.0 - 2.2$ mm. Four different ply stacking sequences were chosen for the layer setups: $[0,90_3]_{sym}$, $[0_2,90_3]_{sym}$, $[0,90_2,0,90]_{sym}$ and $[0_2,90,0,90]_{sym}$. A schematic of a prepared specimen is shown in figure 6.1.
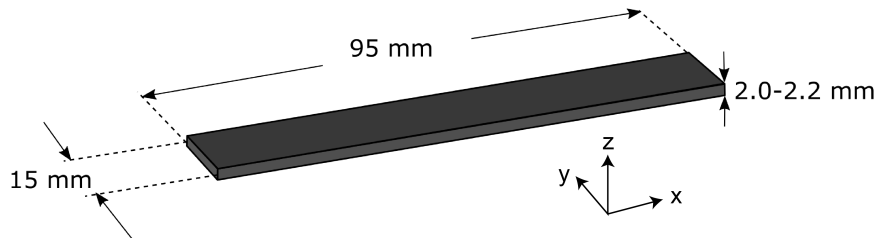

Figure 6.1: Schematic of flexure test specimen with dimensions.

6.1.2 Experimental setup

The three-point flexure test setup was manufactured in accordance with DIN EN ISO 14125 [120]. As for all test setups presented in this text, the test fixture components are manufactured from non-conductive materials, mainly PMMA. Supports and load noses were made from PVC. A tube of pultruded glass-fibre-reinforced plastic is used to introduce the mechanical load. The test setup is schematically shown in figure 6.2.
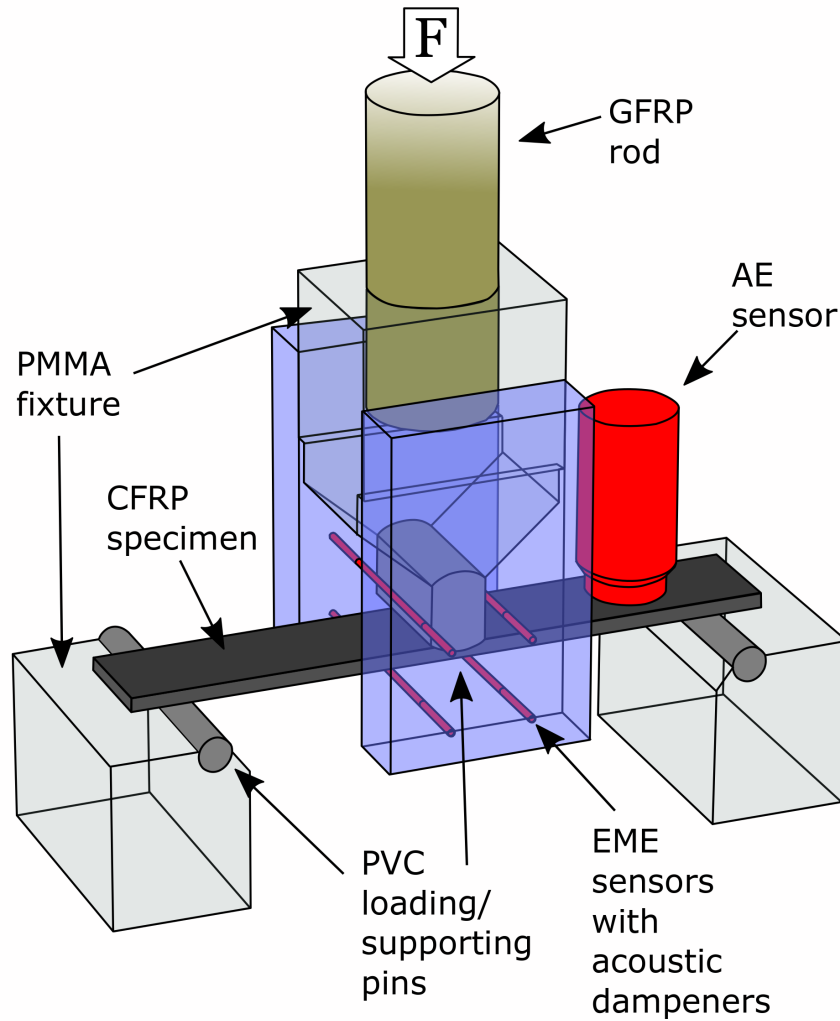

Figure 6.2: Schematic of flexure test setup

Using test fixtures made from plastics naturally increases the compliance of the setups, which can be accounted for in the data reduction. Furthermore, the compliance was measured to be constant within the load range considered in this investigation, and no plastic deformation of the test fixtures was observed.

The mechanical load is applied displacement-controlled by a universal testing ma-

Table 6.1: Acquisition parameters used for AE and EME signal recording during ENF tests. Two different EME setups were used during the tests.

Channel	Threshold [dB$_{AE}$]	Preampl. [dB]	Sample rate [MS/s]	PDT [μs]	HDT [μs]	HLT [μs]
AE	45	40	10	-	-	300
EME	28/25	27/62	10	-	-	300

chine (Zwick ZT 5.0) with a cross-head velocity of 1.2 mm/min. The load is measured with a 5 kN Xforce HP load cell.

The AE sensor, a KRNBB-PC point contact sensor, is mounted on top of the specimen at one side. To prevent grounding of the conducting CFRP specimen by bringing it into direct contact with the grounded AE sensor casing, a thin layer of PE foil is placed between the sensor and the specimen, as described in section 5.3.2. The acoustic signals are amplified by a 2/4/6 preamplifier without internal bandpass filter and recorded by a PCI-2 acquisition card. The acquisition parameters are listed in table 6.1.

As EME sensors, four copper wires are held in position by two blocks of PE foam to minimise EME sensor vibrations caused by acoustic waves travelling through the fixture. Two sensors are positioned above the specimen and two below the specimen. The horizontal and vertical distance between the sensors is 12 mm, which gives a distance from each sensor to the centre of the configuration of 8.5 mm. Figure 6.3 schematically shows the EME sensor configuration.
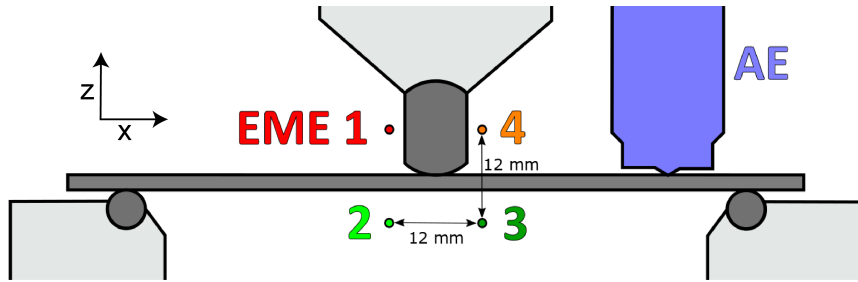

Figure 6.3: Schematic of flexure test setup with EME sensor geometry and positions. Sensors are numbered and displayed in different colours for clear assignment between sensors and signals.

During the experiments, two different EME signal amplification setups were used. For one part of the experiments, the EME signals detected by the sensors were amplified in two stages. A first preamplifier is directly connected to the EME sensors, inside the shielding enclosure. For this internal preamplifier, a junction field effect transistor in a common source circuit with a 10 MΩ input resistor was used. The voltage signal is then further amplified by a UBBV-NF35 low frequency amplifier.

This setup has a total amplification of 62 dB and was used to be able to measure the weaker EME signals generated by the initial failure occurring in the top layer of the specimens. However, the final failure of the specimens was accompanied by much stronger signals. In order to be able to measure these signals, five specimens of each type were tested using only the first amplification stage. This setup has a total amplification of 27 dB.

The EME signals are also recorded by the PCI-2 acquisition card. The EME acquisition parameters are listed in table 6.1.

AE and EME signals are recorded in a synchronised acquisition mode, *i.e.* any signal surpassing the threshold of one of the five channels triggers the acquisition of all channels simultaneously. Thus, a quintuplet of AE and EME signals was recorded for every event, even when the much weaker EME signals did not exceed their threshold value. Furthermore, the AE acquisition also serves as a kind of filter, *i.e.* EME signals detected without corresponding AE signals were considered to not have originated from crack initiation or propagation and were therefore not considered for the analysis.

6.1.3 Results and discussion

All specimens were mechanically loaded until failure occurred. Initial failure occurred in the topmost $0°$ layer under compressive load. Any further damage to the different specimens is governed by the respective ply orientation, the layer thickness and the interaction between compressive and tensile stresses at the top and bottom of the specimens.

Figures 6.4 to 6.7 show exemplary load curves, the amplitudes of the measured AE and EME signals and microscopy images of exemplary, fractured specimens for each of the tested specimen types. For comparability, all four figures show the same axis ranges. The $[0,90_3]_{sym}$ and $[0_2,90_3]_{sym}$ specimens failed in one macroscopic event, while the failure of the $[0_2,90,0,90]_{sym}$ and $[0,90_2,0,90]_{sym}$ specimen occurred in two or more events, each accompanied by strong acoustic and electromagnetic emission. Between these events, weaker emission signals were detected, generated by slow damage accumulation.
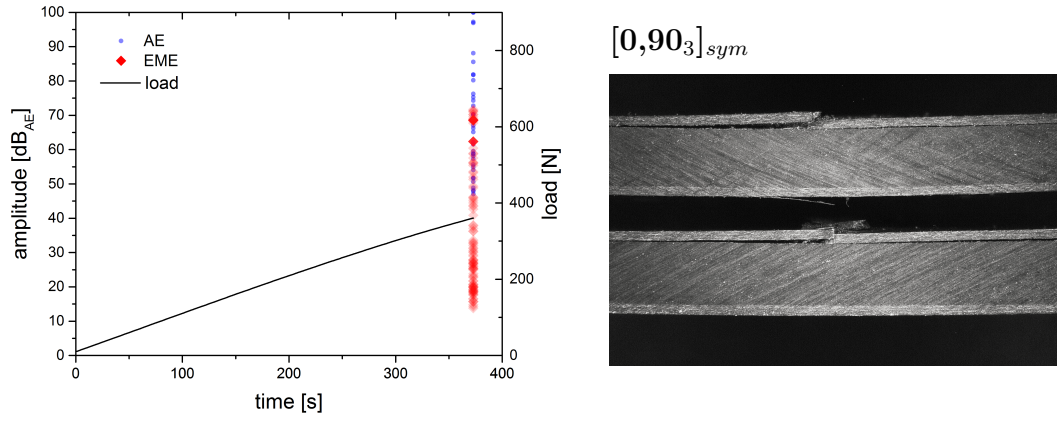
Figure 6.4: Left: Load-time curve and amplitudes of measured signals for exemplary $[0,90_3]_{sym}$ specimen. Right: Microscopy image of two exemplary fractured specimens.
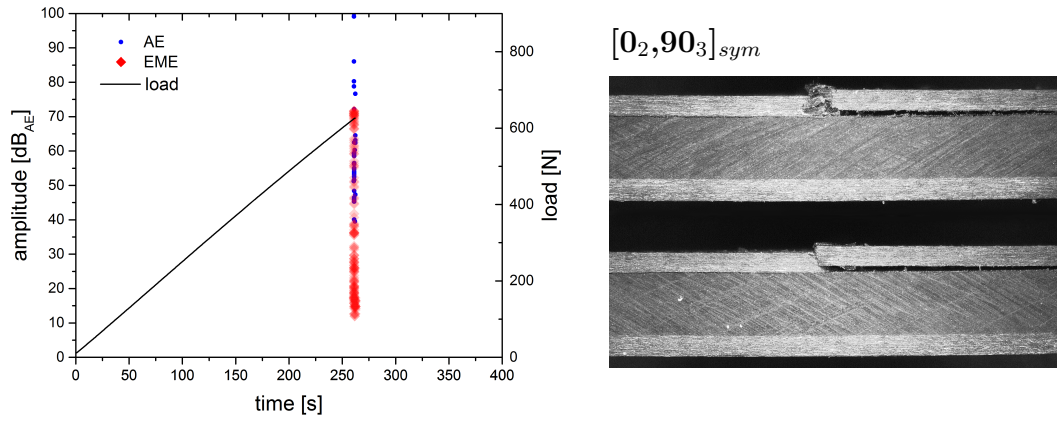

Figure 6.5: Left: Load-time curve and amplitudes of measured signals for exemplary $[0_2,90_3]_{sym}$ specimen. Right: Microscopy image of two exemplary fractured specimens.
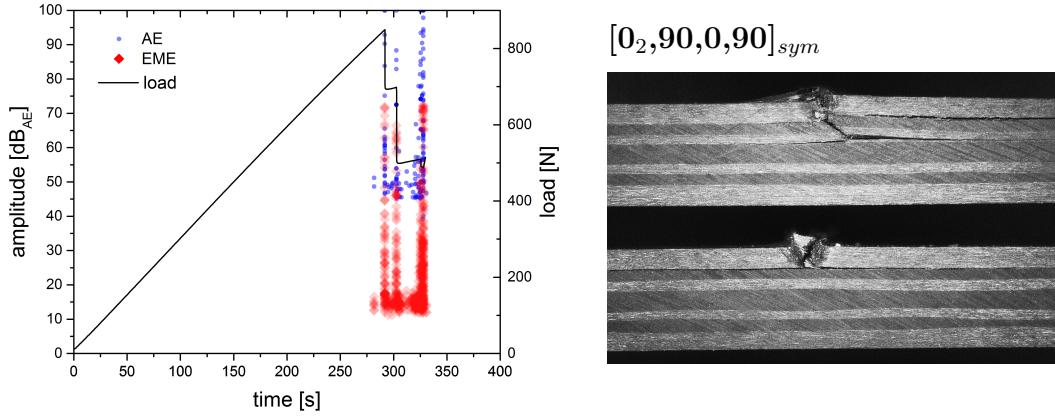
Figure 6.6: Left: Load-time curve and amplitudes of measured signals for exemplary $[0_2,90,0,90]_{sym}$ specimen. Right: Microscopy image of two exemplary fractured specimens.
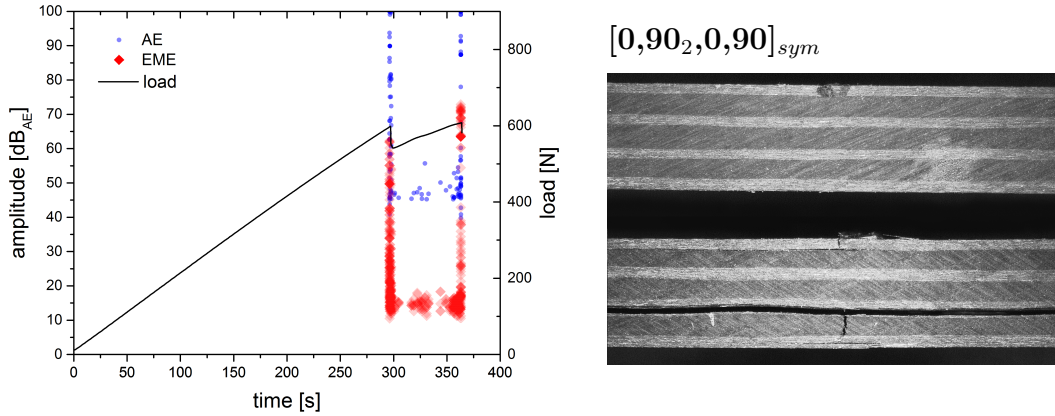

Figure 6.7: Left: Load-time curve and amplitudes of measured signals for exemplary $[0,90_2,0,90]_{sym}$ specimen. Right: Microscopy image of two exemplary fractured specimens.

As is shown in figures 6.4 to 6.7, every major crack event, *i.e.* the final fracture of the specimen or events that cause noticeable load drops, is accompanied by a cascade of AE and EME signals. For most of these events, only the first signal quintuplet can be evaluated, since these signals are not superimposed by other signals. The subsequently recorded signals are mostly reverberations or superpositions of many different signals with no clear beginning or end. Therefore, for every specimen only a few signals will be evaluated and analysed.

Figure 6.8 shows two exemplary signal quintuplets recorded during a flexure test of a specimen with a $[0_2,90_3]_{sym}$ ply stacking sequence. The exemplary EME signals shown in this figure were recorded with the 62 dB preamplification setup. Figure 6.8 (a) shows the signals emitted by a weak emission event that occurred before

the final failure of the specimen. Figure 6.8 (b) shows multiple signals emitted in close succession during the final failure of the specimen. Here, only the first weak signal lies within the measuring range of the 62 dB preamplification setup, while the following EME signals significantly exceed the the limits of the setup. As mentioned in the experimental setup section, to measure these significantly stronger signals generated by macroscopic failure, some specimens were tested with the 27 dB preamplification setup. This also means that for a single specimen, not all of the emitted EME signals can be measured adequately with one of the setups. However, the range in EME signal strength is larger than what could be covered by the two amplification setups, as some signals could barely be distinguished from the noise floor with the sensitive setup, and some signals even exceeded the working range of the less sensitive setup.
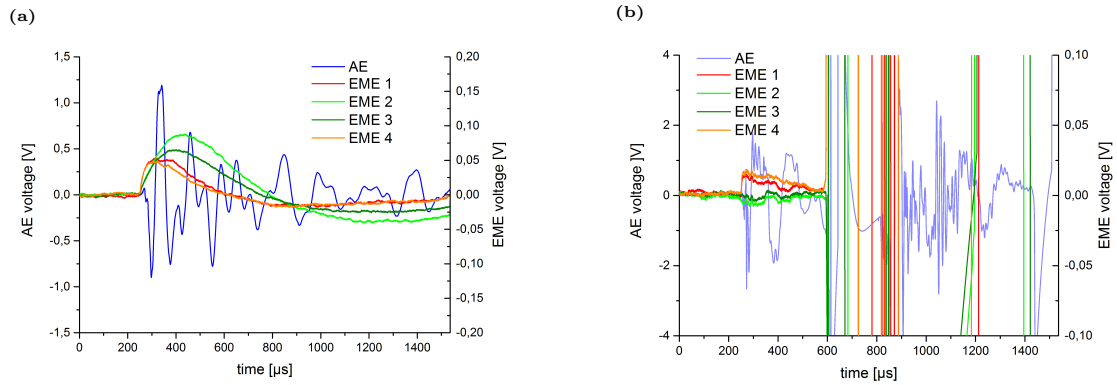

Figure 6.8: Exemplary AE and EME signals recorded during fracture of $[0_2,90_3]_{sym}$ specimen. EME signals are recorded with the 62 dB preamplification setup.

The results presented in chapter 5 suggest, that the polarisation of EME signals measured on opposite sides of an interlaminar fracture in CFRP can be opposite or the same. A similar effect is also illustrated in figures 6.8 (a) and (b) where in one case all EME signals are of the same polarisation, and in one case, the EME signals measured above the specimen (sensors 1 and 4) are of a different polarisation than the ones measured below the specimen (sensors 2 and 3).

During the experiments presented in this chapter, the ply stacking sequences are the only external parameter that was varied. This variation results in fracture behaviour that also significantly varies. Furthermore, even for specimens with the same layer sequence, the fracture characteristics (like orientation, position or volume) may differ greatly. This also results in significantly varying characteristics of the recorded EME signals. For this reason and because of the limited number of evaluable signals, a meaningful statistical analysis is not feasible. Instead, for each type of specimen, exemplary signals are presented and discussed. For the analysis of the internal damage and specifically the determination of the fracture surface orientations, computer tomography scans of the fracture regions of selected specimen

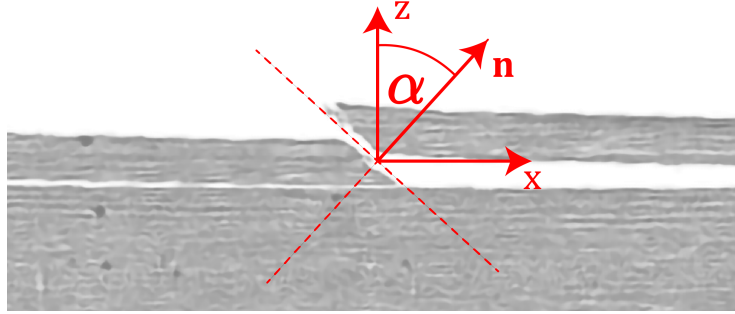(three per ply stacking type) were made.

Figure 6.9: Image detail of a 0° layer fracture. The crack surface angles are measured in the x-z plane as the angle between the crack surface normal and the z axis.

Since the EME measurement setup is a quasi 2D setup, the angles of the crack surfaces are measured in the x-z plane as the angle between the crack surface normal and the z axis, as is shown schematically in figure 6.9.

$[0,90_3]_{sym}$

The specimens with the $[0,90_3]_{sym}$ ply stacking sequence all failed in one major fracture event. The failure was preceded by weak emission signals indicating beginning microscopic failure. In figure 6.10, two EME signal quadruplets are shown. The signals shown in figure 6.10 (a) were recorded with the 62 dB preamplification setup shortly before final failure of one specimen. The signals shown in figure 6.10 (b) were recorded with the 27 dB preamplification setup during final failure of another specimen. For comparability, the differences in amplification are taken into account in the figure axes.
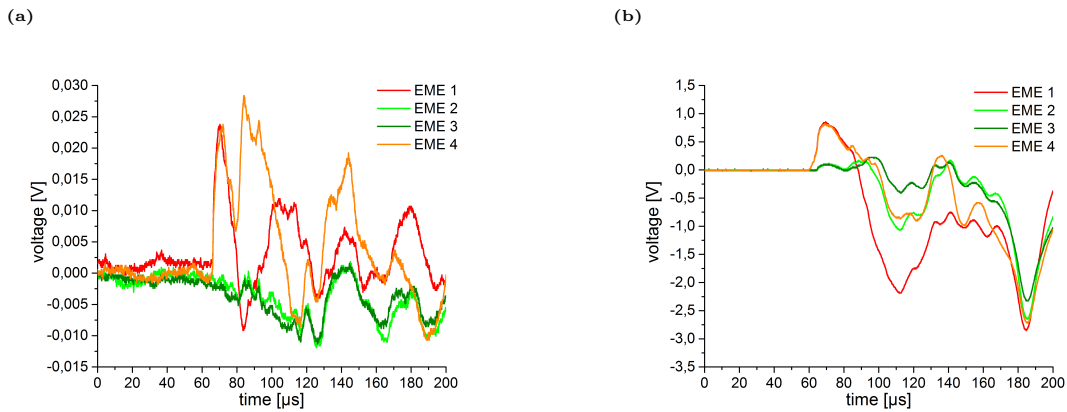

Figure 6.10: Exemplary EME signals recorded during fracture of $[0,90_3]_{sym}$ specimens, (a) recorded with the 62 dB preamplification setup shortly before final failure, and (b) recorded with the 27 dB preamplification setup during final failure. For comparability, differences in amplification are taken into account for the voltage axes.

94

Figure 6.11 shows three tomographic cross-sectional images of the fracture region of a $[0,90_3]_{sym}$ specimen at three different y positions along the width of the specimen. Initial failure occurs in the topmost 0° layer. The orientation of the crack surfaces in this layer greatly varies along the width of the specimen, with angles between 37° and 149°. After the fracture of the topmost 0° layer, large scale delamination between the 0° layer and the adjacent 90° layer occurs with fracture surface angles of ±5°, although the angles were probably slightly larger at the time of fracture due to the bend of the specimen under load.
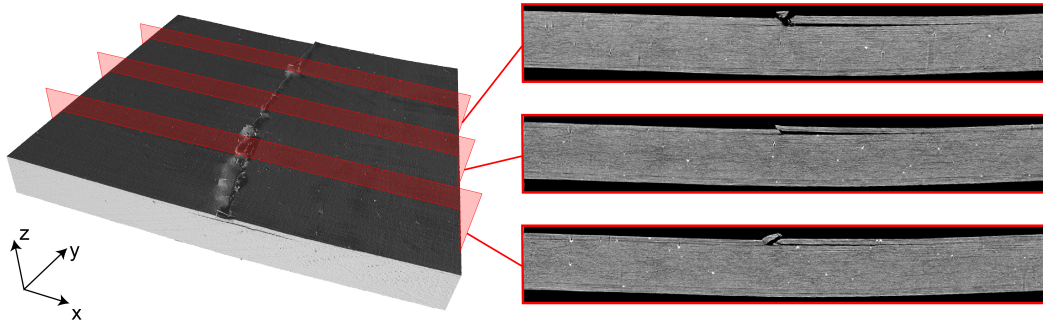

Figure 6.11: CT image of fracture region of a $[0,90_3]_{sym}$ specimen with three cross-sectional images (positions of cross-sectional images are highlighted in the 3D image).

For both of the exemplary EME signal quadruplets, the signals recorded with the two sensors above the specimen (1 and 4) as well as the signals recorded below the specimen (2 and 3) are identical at first, then start to diverge. However, the signals measured above the specimen are of a much higher amplitude. Although the exact location and orientation of the source of the exemplary signals is unknown it is assumed that the first, weaker signals (figure 6.10 (a)) originate in the 0° layer, while the stronger signals are emitted during the delamination. Besides the difference in amplitude, the weaker signals shown on the left contain higher frequencies. On the other hand, the similarities in the distribution of the amplitudes among the sensors could be due to both quadruplets being generated by the same kind of source, but with different amounts of energy.

$[0_2,90_3]_{sym}$

The specimens with the $[0_2,90_3]_{sym}$ ply stacking sequence also failed in one major fracture event. Shortly before final failure, weak EME signals were emitted due to beginning microscopic failure. Figure 6.12 shows two EME signal quadruplets. The signals shown in figure 6.12 (a) were recorded with the 62 dB preamplification setup shortly before final failure of one specimen. The signals shown in figure 6.12 (b) were recorded with the 27 dB preamplification setup during final failure of another specimen.
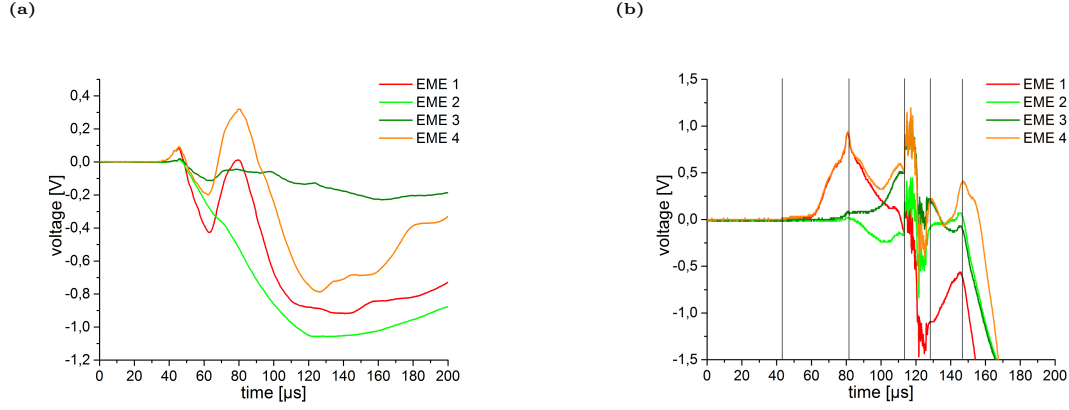
95

Figure 6.12: Exemplary EME signals recorded during fracture of $[0_2,90_3]_{sym}$ specimens, (a) recorded with the 62 dB preamplification setup shortly before final failure, and (b) recorded with the 27 dB preamplification setup during final failure. For comparability, differences in amplification are taken into account for the voltage axes.

Figure 6.13 shows three tomographic cross-sectional images of the fracture region of a $[0_2,90_3]_{sym}$ specimen at three different y positions along the width of the specimen. Initial failure also occurs in the two topmost 0° layers. The angles of the fracture surfaces in these layers, determined from the CT images, vary between 59° and 135°. After the fracture of the two topmost 0° layers, delamination between the 0° layer and the adjacent 90° layer occurs with fracture surface angles of $\pm4°$. In addition, smaller and larger regions of intra-ply fracture in the 0° layers can be observed, with fracture surface angles of $\pm5°$.
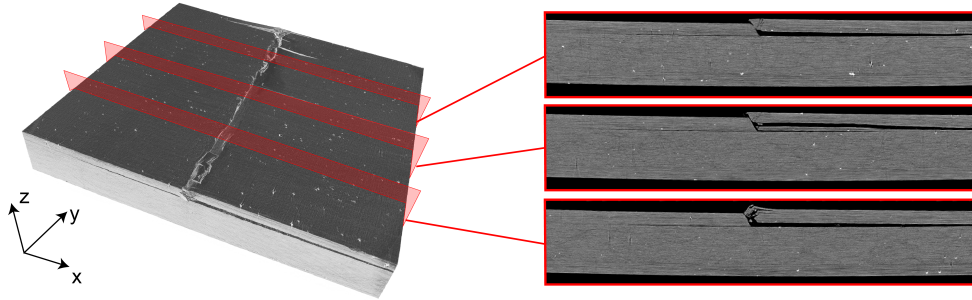

Figure 6.13: CT image of fracture region of a $[0_2,90_3]_{sym}$ specimen with three cross-sectional images (positions of cross-sectional images are highlighted in the 3D image).

The signals recorded shortly before final failure, shown in figure 6.12 (a), start the same way as the ones presented for the $[0,90_3]_{sym}$ specimens. For the first 10 µs the signals of sensors 1 and 4 are identical, as well as the signals of sensors 2 and 3, with the former having much higher amplitudes. Then the signal from the sensor 2 increases in amplitude, while the one from sensor 3 remains weak by comparison. Furthermore, signals 1 and 4 show clear oscillations, while signals 2 and 3 do not. The signals shown in figure 6.12 (b) were recorded during final failure

of the specimen. These signals appear to be superpositions of signals generated by several sources (as is indicated in the figure). However, the beginning of the signals is similar to the other signals presented so far.

$[0_2,90,0,90]_{sym}$

For the specimens with the $[0_2,90,0,90]_{sym}$ ply stacking sequence, multiple larger fracture events occurred before the final failure. For some of these events, each accompanied by a noticeable drop in applied load and strong signal emission, precursor signals could be detected. Figure 6.14 shows two EME signal quadruplets. The signals shown in figure 6.14 (a) were recorded with the 62 dB preamplification setup shortly before a major fracture event. The signals shown in figure 6.14 (b) were recorded with the 27 dB preamplification setup during macroscopic failure.
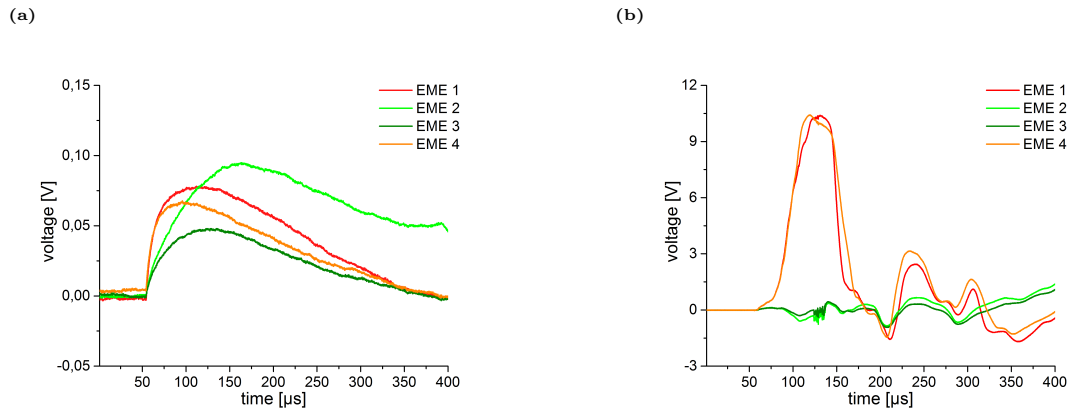
(a)

(b)

Figure 6.14: Exemplary EME signals recorded during fracture of $[0_2,90,0,90]_{sym}$ specimens, (a) recorded with the 62 dB preamplification setup shortly before final failure, and (b) recorded with the 27 dB preamplification setup during final failure. For comparability, differences in amplification are taken into account for the voltage axes.

Figure 6.15 shows three tomographic cross-sectional images of the fracture region of a $[0_2,90,0,90]_{sym}$ specimen at three different y positions along the width of the specimen. Starting at the top of the specimen, damage spreads to the layers beneath, causing different kinds of failure types. In the two topmost 0° layers mostly compressive fibre failure occurs. These macroscopic cracks, with crack surface angles between 51° and 128°, continue through the four top layers, with inter-fibre failure in the 90° layer. Large areas of delamination between the layers and smaller regions of intra-ply fracture in the 0° layers can be observed in the top half of the specimen. The signals recorded shortly before macroscopic failure, shown in figure 6.14 (a), show comparable characteristics. Here, the signal recorded with sensor 2 has the highest amplitude. The difference in rise time between the signals recorded above and below the specimen will be discussed in the next section. The signals shown in figure 6.14 (b) were recorded during macroscopic failure. Very strong and almost identical signals were recorded at the sensors above the specimen with much weaker
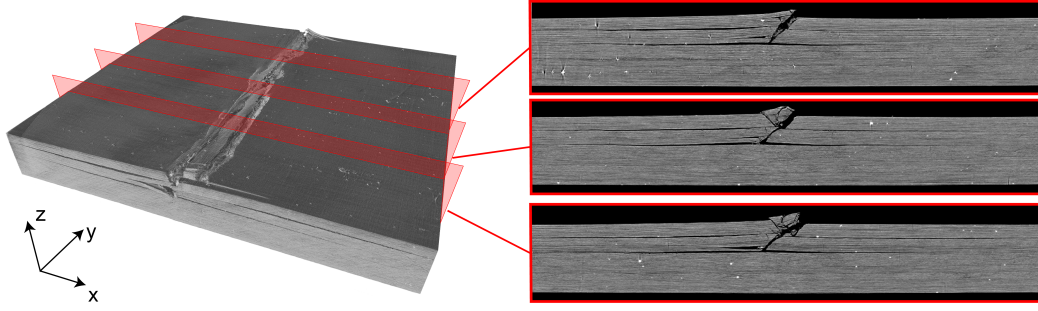
Figure 6.15: CT image of fracture region of a $[0_2,90,0,90]_{sym}$ specimen with three cross-sectional images (positions of cross-sectional images are highlighted in the 3D image).

signals at the other sensors.

Although most of the specimen failed in a manner that is described above, some also show significant damage at the bottom of the specimen. Here, the material failed under tension, with fibre failure, inter-fibre failure, delamination and intra-ply fracture. Figure 6.16 shows three cross-sectional images of the fracture region of such a specimen.
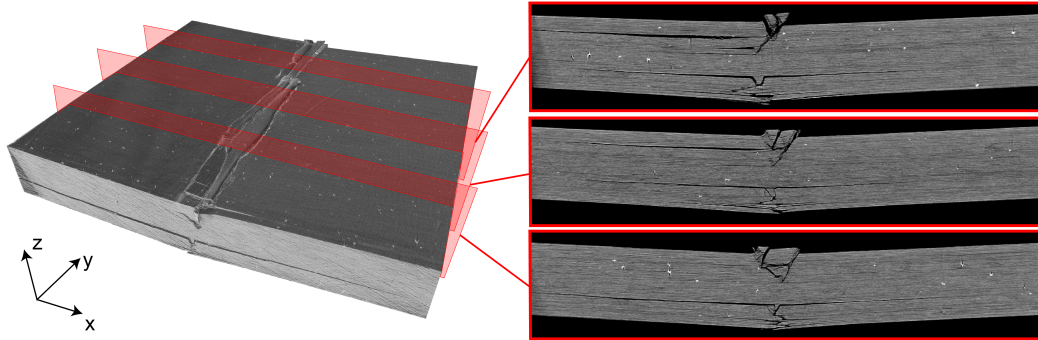

Figure 6.16: CT image of fracture region of a $[0_2,90,0,90]_{sym}$ specimen with three cross-sectional images (positions of cross-sectional images are highlighted in the 3D image). Here, in comparison to figure 6.15, damage also occurred at the bottom of the specimen.

In figure 6.17, three EME signal quadruplets are displayed that were recorded during the failure of this specimen. These signals are quite different from the ones assumed to originate from the top layers of the specimen. Here, the EME signals measured with the sensors below the specimen (2 and 3) are mostly recorded with higher amplitudes, although the difference in amplitude between top and bottom signals is less pronounced. Furthermore, these signals contain components with higher frequencies.
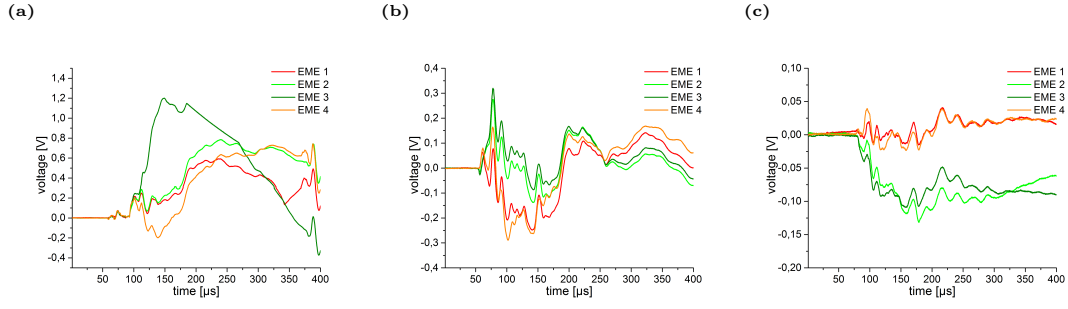
Figure 6.17: EME signals of three fracture events recorded with the 62 dB preamplification setup during failure of a $[0_2,90,0,90]_{sym}$ specimen (CT images of this specimen are shown in fig. 6.16).

$[0,90_2,0,90]_{sym}$

The specimens with the $[0,90_2,0,90]_{sym}$ ply stacking sequence also failed in two or more fracture events. Each of these events is accompanied by strong signal emission, and some were preceded by weak precursor signals. Figure 6.18 shows two EME signal quadruplets. The signals shown in figure 6.18 (a) were recorded with the 62 dB preamplification setup shortly before a major fracture event. The signals shown in figure 6.18 (b) were recorded with the 27 dB preamplification setup during macroscopic failure.
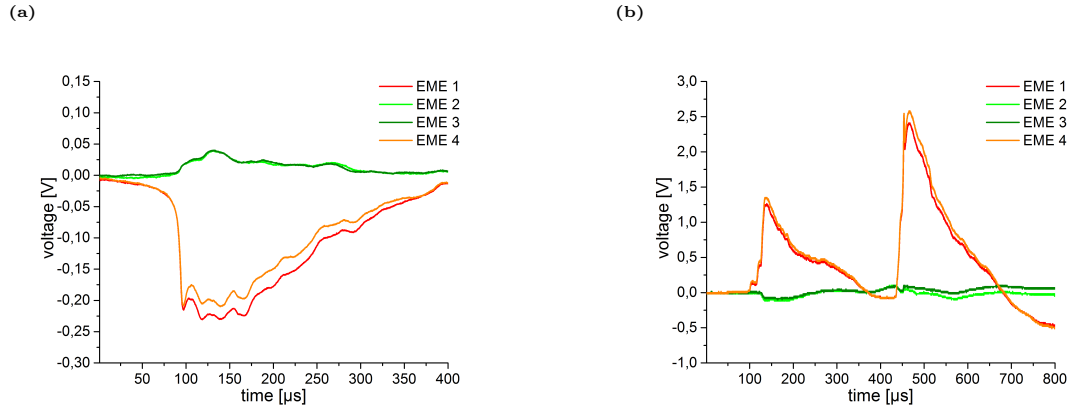

Figure 6.18: Exemplary EME signals recorded during fracture of $[0,90_2,0,90]_{sym}$ specimens, (a) recorded with the 62 dB preamplification setup shortly before final failure, and (b) recorded with the 27 dB preamplification setup during final failure. For comparability, differences in amplification are taken into account for the voltage axes.

Figure 6.19 shows three tomographic cross-sectional images of the fracture region of a $[0,90_2,0,90]_{sym}$ specimen at three different y positions along the width of the specimen. The topmost 0° layer exhibits similar damage in the first layer as all the other types of specimens, *i.e.* fracture with crack surface angles between 61° and 123° as well as delamination between the first two layers. Most of the damage

99

however occurred at the bottom of the specimens, with failure of the last 0° layer and the two 90° layers above and extensive delamination between the two 90° layers and the 0° layer above.
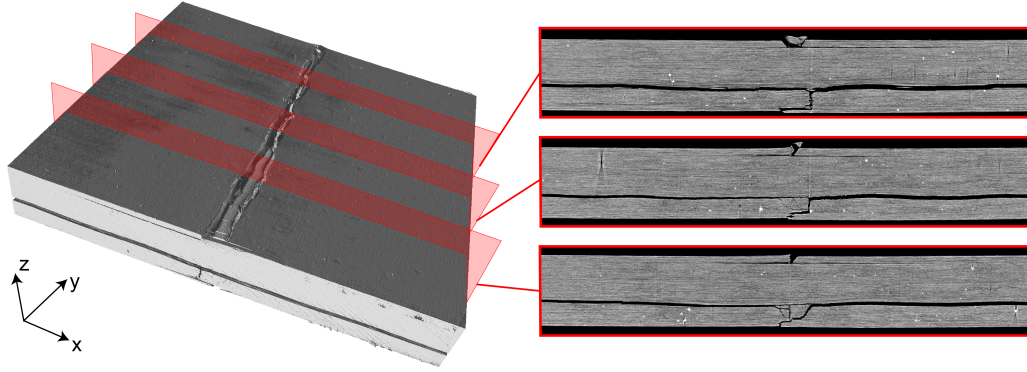

Figure 6.19: CT image of fracture region of a $[0,90_2,0,90]_{sym}$ specimen with three cross-sectional images (positions of cross-sectional images are highlighted in the 3D image).

The signals shown in figure 6.18 (a), precursor signals recorded shortly before the first macroscopic failure of a specimen, exhibit characteristics similar to precursor signals recorded for the other specimen types. The signals measured on each side of the specimen are almost identical, and the ones measured above the specimen have higher amplitudes. Furthermore, the signals measured below the specimen have a longer rise time. Figure 6.18 (b) shows signals measured at the first noticeable load drop. They are similar to the precursor signals, but much stronger. Here, signals of two events in close succession could be measured. These double event signals for the first macroscopic failure could be measured for all five specimens tested with the less sensitive, 27 dB preamplification setup. These were the only signals for any specimen that could be measured with a good repeatability.

Signals generated by the final failure, occurring at the bottom side of the specimen, were very strong and exceeded even the working range of the 27 dB preamplification setup. Therefore, there are no evaluable signals generated by this failure.

For many of the EME signal quadruplets presented above, regardless of the ply stacking sequence of the specimen, the signals at the sensors below the specimen have longer rise times. One effect that can cause such behaviour is low-pass filtering. Most of these signals are assumed to originate at the topmost layers. So a kind of shielding effect caused by the conductive specimen between the signal source and the sensors below might be a reason for this observation. Nevertheless, the signals shown in figure 6.17 are assumed to originate in the bottom layers, and no comparable effect can be observed for the signals at the opposite side of the specimen. Another possible explanation might be differences in the measurement setup at both sides of the specimen. As is shown in figure 6.3, the sensors above the specimen are positioned right next to the load nose made from PVC. Remaining static charges

on the surface of the load nose material or influences by the material itself may influence the signals measured by the sensors in the vicinity.

The orientations of the crack surfaces in the top layers, as determined from the CT scan images, can vary greatly along the specimen width. Therefore, only an approximation or a general orientation can be given. However, based on the results presented here, one cannot conclude a simple correlation between EME signals strengths at each sensor and the approximate crack orientation. For a clear correlation between signal amplitude and detection angle, as was observed for the resin specimens and presented in chapter 3.1.3, a crack orientation of 45° would result in strong signals measured at sensors 2 and 4 and weak signals measured at sensors 1 and 3. This was not observed here. Instead, signals measured at one side of the specimen were mostly identical in amplitude, regardless of crack orientation. The most likely explanation seems to be the anisotropic electric properties of the CFRP specimen. As was presented in chapter 5.1, the specimens are conductive, with conductivities depending on fibre and layer orientation. However, further investigation is needed to test this assumption.

Considering the significant variations in the characteristics in the measured EME signals as a result of different fracture behaviours, crack orientations and crack positions, further tests with fewer varying parameters might be needed to identify certain correlations between fracture properties and EME features.

7 Summary and conclusion

In the context of this work, it was investigated whether and how the measurement of electromagnetic emission during the failure of fibre-reinforced composites can be used to obtain information about the failure process. This was motivated by the fact that certain information can remain hidden from other, established investigation methods, such as acoustic emission analysis, or can only be obtained with considerable analytical effort and a precise knowledge of material properties and structure.

Since the measurement of EME signals during the failure of solids is not an established standard measurement method, and existing publications specifically on EME during the failure of CFRP are very limited, a suitable measurement setup had to be developed first. In the course of the project, this measurement setup was constantly developed and adapted, not least because new insights were gained with each test, and new challenges had to be overcome. The measurement setup used for the final tests on CFRP comprised sensors that were optimised in geometry and position and mounted in a vibration-damped manner, a customised preamplifier chain, an electrically insulated shielding chamber and a mechanical test fixture made of non-conductive material. Furthermore, the simultaneously used AE sensors were attached to the specimens in an electrically insulated manner, all metallic surfaces inside the shielding enclosure were grounded, and all non-conductive surfaces, including the specimens, were treated antistatically before the tests.

Analyses of the electronic measurement setup also show that measurement systems with flat transfer functions are possible. This enables an almost undisturbed information transfer over a wide frequency range and represents one of the great advantages of the method compared to other methods.

Before the actual measurements of the EME during the failure of CFRP, extensive tests were carried out on the individual components of CFRP. The aim of the investigations was on the one hand to examine the properties of the EME as a function of the material properties of the individual components. In addition, with less complex fracture behaviour, the EME characteristics associated with fracture evolution could be better investigated.

The experiments and their results on EME in polymer specimen failure, presented in chapter 3, initially allowed certain assumptions to be made about possible source models. This was particularly necessary as proposed models published in the literature are numerous and sometimes contradictory. Furthermore, the results of the experiments on polymers show that EME in these materials are very short-range and angle-dependent. The latter could be used to determine the orientation of a fracture, a possibility not readily available to other non-destructive testing methods.

It was shown that the rise time of the EME signals most likely correlates directly with the crack dynamics, and a derivation of the crack velocities in the investigated materials based on this assumption produces reasonable results.

Although the EME signals generated by the failure of the different polymer types differ significantly in some characteristics, especially the signal amplitude, no direct correlation between material and signal properties could be found. This is mainly due to the fact that the failure mechanisms of the individual polymer types already differ significantly. For a more precise analysis of the correlation between material properties and EME properties, it would have been more useful to restrict the experiments to one type of polymer and then to vary a specific material parameter. The results of the experiments on single fibres and fibre bundles, presented in chapter 4, show that failure of carbon fibres is also accompanied by clearly measurable EME. However, due to the very short fracture times, the signals could not be recorded unaltered. The measuring system used did not have a high enough sample rate necessary to accurately capture the fast emission processes. Nevertheless, it could be shown that the EME signals of the fibre fractures differ significantly from the EME signals of the polymer tests.

Results of fracture tests on CFRP specimen were presented in chapters 5 and 6. However, the tests presented in chapter 5 caused inter-laminar failure and thus mainly failure of the matrix material. The flexure tests presented in chapter 6 also caused significant failure of the fibres in the material.

DCB and ENF tests were conducted with the aim of investigating the EME dependence on fracture modes. Mode I failure of CFRP was accompanied by significant EME. Two different types of EME signals were observed. A correlation of the different signal types with a certain fracture process could not be found. Furthermore, the polarities of the EME signals recorded on the opposite sides of the fracture were investigated. A clear majority of all recorded signals showed the same polarity on both sensors. For mode II failure of CFRP specimens, no significant EME signals were recorded. A comparison of EME signals between the two fracture modes could therefore not be made. The reason for the lack of EME in the ENF tests may be the different energy release rates of the fracture processes. This means that possible EME signals were too weak to be recorded with the measurement equipment used. Furthermore, it cannot be ruled out that the mode II fracture process itself could also tend to generate weaker EME.

Finally, chapter 6 presents the results of flexure tests on CFRP specimens. Specimens with different ply stacking sequences were loaded under bending load until final, macroscopic failure occurred. Four EME sensors were positioned around the crack area to measure the directionality of the generated EME. During the tests, multiple possible failure modes in CFRP were generated within the differently layered specimens. In addition to matrix cracking and large scale inter- and intralaminar failure, significant fibre failure was generated in the outer layers of the laminates. For many of the occurring crack events, the corresponding EME signals could be recorded on all four sensors. Because of the strong variations in fracture evolution for each type of layer setup, the measured EME signals showed widely different

characteristics. These EME characteristics depend on the source orientation and position, crack energy and fracture type. The anisotropic electric conductivity of the material is assumed to strongly influence the orientation of the emitted electric fields. Because of this material property and because the crack orientation could only be determined within a certain range of variation, no clear angular dependency of the EME signals was found for the CFRP tests.

These last experiments on CFRP generated a great variety of different EME signals. These signals very likely contain valuable information about their source processes. However, specific correlations were not determined here, mainly because of the limited number of tested specimens, the great variety in fracture behaviour and a number of additional influences like the materials conductivity or possibly the still asymmetrical test setup (with respect to the x-y plane).

In summary, it can be noted that the measurement of the electromagnetic signals emitted during the failure of CFRP offers considerable potential for the analysis of fracture processes. Based on the results presented in this text, it can be concluded that the measured signals have properties that are directly related to certain fracture parameters. Furthermore, the measurement is possible with relatively little metrological effort.

However, there are still many possibilities for improvements, further developments and in-depth analyses. For example, the need for shielding when measuring EME signals would be an inconvenience for practical applications, but other methods to eliminate signal noise could be applied. Furthermore, there is a need to refine the theoretical considerations of the underlying physical processes. In particular, the model for the source mechanism requires deeper investigation. The influence of the surrounding matter and its electrical properties should also be investigated in more detail. The theory of signal evolution, *i.e.* the successive influences of source, propagation path, sensor and measuring circuit, should then be developed further.

Bibliography

[1] Gade S.O., Weiss U., Peter M.A. and Sause M.G.R. (2014) Relation of Electromagnetic Emission and Crack Dynamics in Epoxy Resin Materials. *J. Nondestruct. Eval.* **33** 711-723

[2] Gade S.O. and Sause M.G.R (2017) Measurement and Study of Electromagnetic Emission Generated by Tensile Fracture of Polymers and Carbon Fibres. *J. Nondestruct. Eval.* **36** (9) 1-13

[3] Gade S.O., Alaca B.B. and Sause M.G.R (2017) Determination of Crack Surface Orientation in Carbon Fibre Reinforced Polymers by Measuring Electromagnetic Emission. *J. Nondestruct. Eval.* **36** (21) 1-7

[4] Lund J. and Byrne J. (2001) Leonardo Da Vinci's tensile strength tests: Implications for the discovery of engineering mechanics. *Civ. Eng. Environ. Syst.* **00** 1-8

[5] Griffith A.A. (1921) The phenomena of rupture and flow in solids. *Philos. Trans. R. Soc. London Ser. A.* **221** 163-198

[6] Irwin G.R. (1957) Analysis of Stresses and Strains near the End of a Crack Traversing a Plate. *J. Appl. Mech.* **24** 361–364

[7] Anderson T.L. (2005) *Facture Mechanics - Fundamentals and Applications.* Taylor & Francis.

[8] Soboyejo W. (2002) *Mechanical Properties of Engineered Materials.* Marcel Dekker Inc.

[9] Dowling N.E. (2013) *Mechanical Behavior of Materials - Engineering Methods for Deformation, Fracture, and Fatigue.* Pearson.

[10] Schürmann H. (2007) *Konstruieren mit Faser-Kunststoff-Verbunden.* Springer.

[11] Elices M. and Llorca J. (2002) *Fiber Fracture.* Elsevier Science.

[12] Knauss W.G. (1989) Time dependent fracture of polymers. *7th International Conference on Fracture*, Houston.

[13] Williams J.G. (1977) Fracture mechanics of polymers. *Polym. Eng. Sci.* **17** 144-149

[14] Kausch H.H. (2001) Fracture mechanical characterization of semicrystalline thermoplastics. *10th International Conference on Fracture*, Honolulu.

[15] Puck A. and Schürmann H. (1998) Failure analysis of FRP laminates by means of physically based phenomenological models. *Compos. Sci. Technol.* **58** 1045-1067

[16] Puck A. and Schürmann H. (2002) Failure analysis of FRP laminates by means of physically based phenomenological models. *Compos. Sci. Technol.* **62** 1633-1662

[17] Naghipour P., Schneider J., Bartsch M., Hausmann J. and Voggenreiter H. (2009) Fracture simulation of CFRP laminates in mixed mode bending. *Eng. Fract. Mech.* **76** 2821-2833

[18] Jumahat A., Soutis C., Jones F.R. and Hodzic A. (2009) Fracture mechanisms and failure analysis of carbon fibre/toughened epoxy composites subjected to compressive loading. *Compos. Struct.* **92** 295-305

[19] Srinivasaa V., Shivakumara V., Nayakaa V., Jagadeeshaiaiha S., Seethrama M., Shenoya R. and Nafidie A. (2010) Fracture Morphology of Carbon Fiber Reinforced Plastic Composite Laminates. *Mater. Res.* **13** 417-424

[20] Landau L.D. and Lifshitz E.M. (1986) *Course of Theorical Physics: Theory of Elasticity*. Pergamon press.

[21] Auld B.A. (1973) *Acoustic Fields and Waves in Solids*. John Wiley & Sons.

[22] Hellier C.J. (2003) *Handbook of Nondestructive Evaluation*. McGraw-Hill.

[23] Grosse C.U. and Ohtsu M. (2008) *Acoustic Emission Testing*. Springer.

[24] Eitzen D.G. and Wadley H.N.G. (1984) Acoustic Emission: Establishing the Fundamentals. *J. Res. Natl. Bur. Stand. (U.S.)* **89** 75-100

[25] Ono K. and Ohtsu M. (1984) A generalized theory of acoustic emission and Green's functions in a half space. *J. Acoust. Emiss.* **3** 27-40

[26] Ohtsu M. and Ono K. (1986) The generalized theory and source representations of acoustic emission. *J. Acoust. Emiss.* **5** 124-133

[27] Green E.R. (1995) Acoustic emission sources in a cross-ply laminated plate. *Compos. Eng.* **5** 1453-1469

[28] Green E.R. (1998) Acoustic Emission in Composite Laminates. *J Nondestruct Eval.* **17** 117-127

[29] Wilcox P.D., Lee C.K., Scholey J.J., Friswell M.I., Wisnom M.R. and Drinkwater B.W. (2006) Progress Towards a Forward Model of the Complete Acoustic Emission Process. *Adv. Mat. Res.* **13-14** 69-75

[30] McLaskey G.C. and Glaser S.D. (2012) Acoustic Emission Sensor Calibration for Absolute Source Measurements. *J Nondestruct Eval.* **31** 157-168

[31] Hamstad M.A. (2007) Acoustic Emission Signals Generated By Monopole (Pencil-Lead Break) Versus Dipole Sources: Finite Element Modeling And Experiments. *J. Acoust. Emiss.* **25** 92-106

[32] Zelenyak A.M., Hamstad M.A. and Sause M.G.R. (2015) Modeling of Acoustic Emission Signal Propagation in Waveguides. *Sensors.* **15** 11805-11822

[33] Sause M.G.R., Hamstad M.A. and Horn S. (2012) Finite element modeling of conical acoustic emission sensors and corresponding experiments. *Sens. Actuator A Phys.* **184** 64-71

[34] Sause M.G.R. and Richler S. (2015) Finite Element Modelling of Cracks as Acoustic Emission Sources. *J Nondestruct Eval.* **34** 1-13

[35] Sause M.G.R. (2016) *In-situ monitoring of fiber-reinforced composites.* Springer-International.

[36] Prosser W.H. (1996) Advanced AE techniques in composite materials research. *J. Acoust. Emiss.* **14** 1-11

[37] Gorman M.R. (2011) Modal AE analysis of fracture and failure in composite materials, and the quality and life of high pressure composite pressure cylinders. *J. Acoust. Emiss.* **29** 1-28

[38] Sause M.G.R., Gribov A., Unwin A.R. and Horn S. (2012) Pattern recognition approach to identify natural clusters of acoustic emission signals. *Pattern Recogn. Lett.* **33** 17-23

[39] Sause M.G.R. and Horn S.R. (2010) Influence of specimen geometry on acoustic emission signals in fiber reinforced composites: FEM-simulations and experiments. *29th European conference on acoustic emission testing*, Vienna.

[40] Yamada I., Masuda K. and Mizutani H. (1989) Electromagnetic and acoustic emission associated with rock fracture. *Phys. Earth Planet. Int.* **57** 157-168

[41] Frid V., Rabinovitch A. and Bahat D. (2003) Fracture induced electromagnetic radiation. *J. Phys. D: Appl. Phys.* **36** 1620-1628

[42] Misra A., Prasad R.C., Chauhan V.S. and Srilakshmi B. (2007) A theoretical model for the electromagnetic radiation emission during plastic deformation and crack propagation in metallic materials. *Int. J. Fract.* **2** 99-121

[43] Hadjicontis V., Mavromatou C., Antsygina T.N. and Chishko K.A. (2007) Mechanism of electromagnetic emission in plastically deformed ionic crystals. *Phys. Rev. B* **2** 1-14

[44] Rabinovitch A., Shay A., Liraz R., Frid V. and Bahat D (2005) Electromagnetic radiation emitted during friction process. *Int. J. Fract.* **2** 21-27

[45] Tsutsumi A., Shirai N. (2008) Electromagnetic signals associated with stick–slip of quartz-free rocks. *Tectonophysics.* **1-4** 79-84

[46] Dickinson J.T. (1984) Fracto-emission: The role of charge separation. *J. Vac. Sci. Technol. A* **2** 1112-1116

[47] Shiota T. and Yasuda K. (2010) Simultaneous measurement of the emission of photons and charged particles during fracture of brittle materials. *Mater. Sci. Eng.* **1-3** 248-252

[48] Rabinovitch A., Frid V., Bahat D. and Goldbaum J. (2000) Fracture area calculation from electromagnetic radiation and its use in chalk failure analysis. *Int. J. Rock Mech. Min. Sci.* **37** 1149-1154

[49] Koshevaya S., Grimalsky V., Makarets N., Kotsarenko A., Siquieros-Alatorre J., Perez-Enriquez R. and Juarez-Romero D. (2008) Electromagnetic emission from magnetite plate cracking under seismic processes. *Adv. Geosci.* **14** 25-28

[50] Lacidogna G., Carpinteri A., Manuello A., Durin G., Schiavi A., Niccolini G. and Agosto A. (2010) Acoustic and Electromagnetic Emissions as Precursor Phenomena in Failure Processes. *Strain* 144-152

[51] Mori Y., Obata Y. and Sikula J. (2009) Acoutic and electromagnetic emission from crack created in rock samples under deformation. *J. Acoust. Emiss.* **27** 157-166

[52] Rabinovitch A., Frid V., Goldbaum J. and Bahat D. (2003) Polarization-depolarization process in glass during percussion drilling. *Philos. Mag.* **83** 2929-2940

[53] Aman S., Aman A. and Tomas J. (2012) Method of Crack Formation Analysis Based on Mechanoluminecence. *Mater. Sci. Appl.* **10** 739-744

[54] Dickinson J., Jensen L. and Williams W.D. (1985) Fractoemission from lead zirconate-titanate. *J. Am. Ceram. Soc.* **68** 235-240

[55] Langford S.C., Dickinson J. and Jensen L. (1987) Simultaneous measurements of the electron and photon emission accompanying fracture of single-crystal MgO. *J. Appl. Phys.* **62** 1437–1449

[56] Tudik A.A. and Valuev N.P. (1980) Electromagnetic Emission During the Fracture of Metals. *Sov. Tech. Phys. Lett.* **6** 37-38

[57] Singh R., Lal S. and Misra A. (2014) Variation in electromagnetic radiation during plastic deformation under tension and compression of metals. *Appl. Phys. A* **117** 1203-1215

[58] Singh R., Lal S. and Misra A. (2019) Effect of notch-depth ratio on intermittent electromagnetic radiation from Cu-Ni alloy under tension. *Mater. Test.* **61** 885-893

[59] Dickinson J.T., Jensen L.C. and Dion R.P. (1993) Fracto-emission from high density polyethylene: Bond breaking versus tribological stimulation. *J. Appl. Phys.* **73** 3047-3054

[60] Petrenko V.F. (1996) Electromechanical phenomena in ice. *CRREL Special Report.* **96-2** 1-30

[61] Mizuno Y. (2002) Light emission associated with deformation and fracture of ice. *J. Jpn. Soc. Snow* **64** 241–248

[62] Dickinson J.T., Jahan-Latibari A. and Jensen L.C. (1985) Electron emission and acoustic emission from the fracture of graphite/epoxy composites. *Int. Mater. Sci.* **20** 229-236

[63] Astanin V.V., Shchegel G.O., Hufenbach W., Hornig A. and Langkamp A. (2012) Characterising failure in textile-reinforced thermoplastic composites by electromagnetic emission measurements under medium and high velocity impact loading. *Int. J. Impact. Eng.* **49** 22-30

[64] Sedlak P., Enoki M., Ogasawara T. and Sikula J. (2010) Electromagnetic and acoustic emission in PEEK/Carbon nanotube composites. *29th European Conference on Acoustic Emission Testing*, Vienna.

[65] Stoudek R., Trcka T., Matysik M., Vymazal T. and Plskova I. (2016) Acoustic and electromagnetic emission of lightweight concrete with polypropylene fibers. *Mater. Technol.* **50** 547-552

[66] Dickinson J.T., Jensen L.C. and Bhattacharya S.K. (1985) Fractoemission from the failure of metal/epoxy interfaces. *J. Vac. Sci. Technol.* **3** 1398-1402

[67] K'Singam L.A., Dickinson J.T. and Jensen L.C. (2006) Fractoemission from Failure of Metal-GIass Interfaces. *J. Am. Ceram. Soc.* **68** 510-514

[68] Koktavy P. (2009) Experimental study of electromagnetic emission signals generated by crack generation in composite materials. *Meas. Sci. Technol.* **20** 1-8

[69] Sklarczyk C., Winkler S. and Thielicke B. (1996) Die elektrische Emission beim Versagen von Faserverbundwerkstoffen und ihren Komponenten. *Mat.-wiss. u. Werkstofftech.* **27** 559-566

[70] Macku R., Koktavy P., Trcka T. and Sicner J. (2014) Fracture Related Electromagnetic Emission Measurement and Excess Noise Analysis of Reinforced Composites. *Proc. Mater. Sci.* **3** 116-121

[71] Koktavy P., Pavelka J. and Sikula J. (2004) Characterization of acoustic and electromagnetic emission sources. *Meas. Sci. Technol.* **15** 973-977

[72] Ivanov V.V., Egorov P.V., Kolpakova L.A. and Pimonov A.G. (1988) Crack dynamics and electromagnetic emission by loaded rock masses: Translated from Fiziko-Tekhnicheskie Problemy Razrabotki Poleznykh Iskopaemykh. *Sov. Min. Sci.* **24** 20-27

[73] Sedlak P., Sikula J., Lokajicek T. and Mori Y. (2008) Acoustic and electromagnetic emission as a tool for crack localization. *Meas. Sci. Technol.* **19** 1-7

[74] Takeuchi A. and Nagahama H. (2006) Electric dipoles perpendicular to a stick-slip plane. *Phys. Earth Planet In.* **3-4** 208-218

[75] Petraki E., Nikolopoulos D., Nomicos C.D., Stonham J., Cantzos D., Yannakopoulos P. and Kottou S. (2015) Electromagnetic pre-earthquake precursors: Mechanisms data and models-A Review. *J. earth sci. clim. chang.* **6** 2-11

[76] Carpinteri A. and Borla O. (2017) Fracto-emissions as seismic precursors. *Eng. Fract. Mech.* **177** 239-250

[77] Berri B.L. and Gribov V.A. (1982) Radio irradiation of glaciers and snow avalanches. *Materiali Glatsiologicheskih Issledovanii* **44** 150-156

[78] Li X., Wang E., Li Z., Liu Z., Song D. and Qiu L. (2016) Rock Burst Monitoring by Integrated Microseismic and Electromagnetic Radiation Methods. *Rock Mech. Rock Eng.* **49** 4393-4406

[79] Ogawa T., Oike K. and Miura T. (1985) Electromagnetic radiations from rocks. *J. Geophys. Res.* **90** 6245-6249

[80] O'Keefe S.G. and Thiel D.V. (1995) A Mechanism for the production of Electromagnetic Radiation during the fracture of Brittle Materials. *Phys. Earth and Planet. Inter.* **89** 127-135

[81] Rabinovitch A., Frid V. and Bahat D (2007) Surface oscillations — A possible source of fracture induced electromagnetic radiation. *Tectonophysics* **431** 15-21

[82] Laptukhov A.I. (1995) Generation of an electromagnetic field during rupture of a dielectric. *Russian Phys. J.* **38** 15-19

[83] Allison F.E. (1965) Shock-Induced Polarization in Plastics. I. Theory. *J. Appl. Phys.* **7** 2111-2113

[84] Mastrogiannis D., Antsygina T.N., Chishko K.A., Mavromatou C. and Hadjicontis V. (2015) Relationship between electromagnetic and acoustic emissions in deformed piezoelectric media: Microcracking signals. *Int. J. Solids Struct.* **56-57** 118–125

[85] Chen Z. and Huang K. (2010) A numerical analytic method for electromagnetic radiation accompanying with fracture of rocks. *Chinese Phys. B* **19** 1-6

[86] Dirks H.K. (1996) Quasi-stationary fields for microelectronic applications. *Electr. Eng.* **2** 145-155

[87] Larsson J. (2007) Electromagnetics from a quasistatic perspective. *Am. J. Phys.* **3** 230-239

[88] Haus H.A. and Melcher J.R. (1989) *Electromagnetic fields and energy.* Prentice Hall.

[89] Partridge R.E. (1965) Capacitive probe E-field sensors. *Sensor and simulation notes.* **11** 1-17

[90] IEEE Std 291-1991 (2010) *IEEE Standard Methods for Measuring Electromagnetic Field Strength of Sinusoidal Continuous Waves, 30 Hz to 30 GHz.*

[91] Ramo S. (1939) Currents Induced by Electron Motion. *Proc. IRE* **27** 584-585

[92] Shockley W. (1938) Currents to Conductors Induced by a Moving Point Charge. *J. Appl. Phys.* **9** 635-636

[93] Winkler S. (1993) *Tear detector for mechanical loading test sample - uses capacitive sensor coupled via impedance converter to electronic evaluation circuit.* Patent DE 4004171 C2.

[94] Shiwa M., Inaba S., Carpenter S.H. and Kishi T. (1992) Development of high-sensitivity and low-noise integrated acoustic emission sensor. *Mater. Eval.* **51** 868-874

[95] Klinkenbusch L. (2005) On the Shielding Effectiveness of Enclosures. *IEEE Trans. Electromagn. Compat.* **3** 589-601

[96] Robinson M.P., Benson T.M., Christopoulos C., Dawson J.F., Ganley M.D., Marvin A.C., Porter S.J. and Thomas D.W.P. (1998) Analytical formulation for the shielding effectiveness of enclosures with apertures. *IEEE Trans. Electromagn. Compat.* **3** 240-248

[97] Cooley W. (1968) Low-Frequency Shielding Effectiveness of Nonuniform Enclosures. *IEEE Trans. Electromagn. Compat.* **1** 34-43

[98] Marcuvvitz N. (1986) *Waveguide Handbook.* Institution of Engineering and Technology.

[99] Gooding D.M. and Kaufman G.K. (2014) Tribocharging and the Triboelectric Series. In: Scott R.A. *Encyclopedia of Inorganic and Bioinorganic Chemistry.* John Wiley & Sons.

[100] McCarty L. and Whitesides G. (2008) Electrostatic Charging Due to Separation of Ions at Interfaces: Contact Electrification of Ionic Electrets. *Angew. Chem.* **47** 2188-2207

[101] ASTM E976-10 (2010) *Standard Guide for Determining the Reproducibility of Acoustic Emission Sensor Response. ASTM International.*

[102] Miroshnichencko M. and Kuksenko V. (1980) Study of electromagnetic pulses in initiation of cracks in solid dielectrics. *Sov. Phys. Solid State* **22** 1531–1533

[103] Moosburger-Will J., Greisel M, Sause M.G.R., Horny R. and Horn S (2013) Influence of partial cross-linking degree on basic physical properties of RTM6 epoxy resin. *J.Appl. Polym. Sci.* **130** 4338-4346

[104] DIN EN ISO 527-1 (2012) *Determination of tensile properties of plastics - part 1: General principles*

[105] DIN EN ISO 527-2 (2012) *Determination of tensile properties of plastics - part 2: Test conditions for moulding and extrusion plastics.*

[106] Koizumi N., Yano S. and Tsuji F. (1968) Dielectric Properties of Polytetrafluoroethylene and Tetrafluoroethylene-Hexafluoropropylene Copolymer. *J. Polym. Sci. C* **23** 499-508

[107] Bergman R.H. and Shahbender R.A. (1958) Effect of Statically Applied Stresses on the Velocity of Propagation of Ultrasonic Waves. *J. Appl. Phys.* **29** 1736-1738

[108] Winkler S.R. (2005) Field Emissions Caused by Fracture and Yielding. *Int. J. Fract.* **136** 221-235

[109] Holloway C.L., Sarto M.S. and Johansson M. (2005) Analyzing Carbon-Fiber Composite Materials With Equivalent-Layer Models. *IEEE Trans. Electromagn. Compat.* **47** 833-844

[110] Chippendale R.D. and Golosnoy I.O. (2011) Percolation effects in electrical conductivity of carbon fibre composites. *IET Conference Publications.* **2011** 1-2

[111] Fouladgar J., Wasselynck G. and Trichet D. (2013) Shielding and Reflecting Effectiveness of Carbon Fiber Reinforced Polymer (CFRP) Composites. *2013 International Symposium on Electromagnetic Theory*, Hiroshima.

[112] Wang S. and Chung D.D.L. (2000) Electrical behaviour of carbon fiber polymer-matrix composites in the through thickness direction. *J. Mater. Sci.* **35** 91-100

[113] Almuhammadi K., Bera T.K. and Lubineau G. (2017) Electrical impedance spectroscopy for measuring the impedance response of carbon-fiber-reinforced polymer composite laminates. *Compos. Struct.* **168** 510-521

[114] Bellucci S., Bistarelli S. and Cataldo A. (2015) Broadband Dielectric Spectroscopy of Composites Filled With Various Carbon Materials. *IEEE Trans. Microw. Theory Tech.* **63** 2024-2031

[115] McKenzie A.B. (2015) Characterization of electrical conductivity of carbon fiber/epoxy composites with conductive AFM and scanning microwave impedance microscopy. Thesis. University of Illinois. Urbana, Illinois.

[116] Sause M.G.R. (2011) Investigation of pencil lead breaks as acoustic emission sources. *J. Acoust. Emiss.* **29** 184-196

[117] DIN EN ISO 291 (2008) *Plastics - Standard atmospheres for conditioning and testing.*

[118] ASTM D5528-01 (2001) *Standard Test Method for Mode I Interlaminar Fracture Toughness of Unidirectional Fiber-Reinforced Polymer Matrix Composites. ASTM International.*

[119] ASTM 7905/D7905M-14 (2014) *Standard Test Method for Determination of the Mode II Interlaminar Fracture Toughness of Unidirectional Fiber-Reinforced Polymer Matrix Composites.*

[120] DIN EN ISO 14125 (1998) *Fibre-reinforced plastic composites - Determination of flexural properties.*

Acknowledgements